1976

Directional growth of pearlite in iron-carbon eutectoid alloys

David Dwight Pearson
Iowa State University

INFORMATION TO USERS

This material was produced from a microfilm copy of the original document. While the most advanced technological means to photograph and reproduce this document have been used, the quality is heavily dependent upon the quality of the original submitted.

The following explanation of techniques is provided to help you understand markings or patterns which may appear on this reproduction.

1. The sign or "target" for pages apparently lacking from the document photographed is "Missing Page(s)". If it was possible to obtain the missing page(s) or section, they are spliced into the film along with adjacent pages. This may have necessitated cutting thru an image and duplicating adjacent pages to insure you complete continuity.

2. When an image on the film is obliterated with a large round black mark, it is an indication that the photographer suspected that the copy may have moved during exposure and thus cause a blurred image. You will find a good image of the page in the adjacent frame.

3. When a map, drawing or chart, etc., was part of the material being photographed the photographer followed a definite method in "sectioning" the material. It is customary to begin photoing at the upper left hand corner of a large sheet and to continue photoing from left to right in equal sections with a small overlap. If necessary, sectioning is continued again – beginning below the first row and continuing on until complete.

4. The majority of users indicate that the textual content is of greatest value, however, a somewhat higher quality reproduction could be made from "photographs" if essential to the understanding of the dissertation. Silver prints of "photographs" may be ordered at additional charge by writing the Order Department, giving the catalog number, title, author and specific pages you wish reproduced.

5. PLEASE NOTE: Some pages may have indistinct print. Filmed as received.

University Microfilms International
300 North Zeeb Road
Ann Arbor, Michigan 48106 USA
St. John's Road, Tyler's Green
High Wycombe, Bucks, England HP10 8HR

Directional growth of pearlite in iron-carbon eutectoid alloys

by

David Dwight Pearson

A Dissertation Submitted to the
Graduate Faculty in Partial Fulfillment of
The Requirements for the Degree of
DOCTOR OF PHILOSOPHY

Department: Materials Science and Engineering
Major: Metallurgy

Approved:

Signature was redacted for privacy.
In Charge of Major Work

Signature was redacted for privacy.
For the Major Department

Signature was redacted for privacy.
For the Graduate College

Iowa State University
Ames, Iowa

1976

TABLE OF CONTENTS

INTRODUCTION

Pearlite is a lamellar structure consisting of alternating plates of ferrite (B.C.C. iron) and cementite (an orthorhombic carbide with stoichiometry Fe_3C). It is one of many products which form from the high temperature F.C.C. solid solution, austenite, when cooled below the eutectoid temperature. The structure was first identified by Sorby (1) who referred to it as the "pearly compound" because of the mother-of-pearl appearance given by the diffraction of light from exposed parallel lamellae of a polished and etched specimen. Pearlite was one of the first structures recognized as being important in strengthening steels. Embury and Fisher (2) have shown that drawn pearlite wires can achieve tensile strengths as high as 4,800 MPa, one of the strongest engineering materials available. As a result, the structure and kinetics of growth have been extensively studied with excellent reviews available (3,4,5,6,7). Experimental evidence overwhelmingly indicates that growth is controlled by diffusion. However, the exact nature of the manner in which carbon partitions at the growth interface is still unclear.

There are presently two accepted models for the growth of pearlite. One treats carbon as transporting solely by volume diffusion in the parent austenite, the other treats the diffusion as occurring in the boundary between the two phases. The last model is particularly attractive since it can account for

high growth rates by treating the boundary as a separate phase with high diffusivity. Either model can be characterized by three fundamental variables: (1) the velocity of growth, (2) the temperature of formation, and (3) the interlamellar spacing.

This study is concerned with the accurate determination of the three kinetic variables by the directional transformation of pearlite at constant rate in a steep temperature gradient. This technique has many advantages over the isothermal method of studying pearlite growth. Chief among these is that it fixes the most difficult to determine variable, the velocity. The technique was first employed by Bolling and Richman (8) to get quantitative results of spacing as a function of imposed velocity. Their results were inconclusive; a clear distinction between the two growth modes could not be made but it did appear that boundary diffusion was becoming important at high growth velocities. However, this range of high velocities indicating boundary diffusion was greater than the maximum velocity observed in isothermal work. Carpay (9) has questioned whether pearlite is transforming under truly steady-state conditions at these high pulling rates. One of the goals of this investigation was to determine the maximum velocity at which pearlite can transform continuously.

However, the major goal of this investigation is concerned with the determination of the pearlite interface temperature in the gradient during transformation. In isothermal

experiments, the temperature is fixed and velocities are determined by measuring the extent of reaction as a function of time. On the other hand, the velocity is fixed in the isovelocity experiments and the temperature of the pearlite interface adjusts to an optimum isotherm in the temperature gradient. In previous isovelocity experiments, the interface temperature was unknown and comparison to isothermal work could only be made by assuming the two growth modes were identical. The interface temperature determinations of this study were designed in order to confirm this assumption. Also, with all three kinetic parameters determined, velocity, interlamellar spacing, and interface temperature, a self-consistent set of data is generated which enables a selection of the proper kinetic model or models to be made.

THEORY

Kinetic models for pearlite growth began almost immediately after the structure was identified and knowledge that it was produced by the decomposition of austenite. Early attempts to characterize the growth were based on volume diffusion of carbon in the parent austenite. These were criticized because they appeared to depend on higher diffusivities than could be reasonably extrapolated to lower temperatures. As a result, models based on grain boundary diffusion were developed because of the fast diffusion associated with the disordered structure of high angle boundaries. The following sections contain short reviews of the two kinetic models.

Volume Diffusion

Although several models had been made earlier describing carbon diffusion in austenite as rate controlling (3), credit is generally given to Zener (10) for the first complete model. He correctly noted the importance of the free energy associated with the interfaces between the respective phases and the variation of local phase equilibria with curvature. Zener developed a model based largely on dimensional arguments, which, at least qualitatively, explained the growth kinetics of pearlite. His model predicted a range of pearlite growth velocities at a given temperature and suggested that conditions would adjust so that growth proceeded at maximum velocity. A short derivation is germane to this study, and the one

to be given here is based on Zener's original work and a review by Hillert (11).

The essential features for edgewise growth of pearlite can be envisioned by referring to Figures 1 and 2. All carbon transport is in the austenite with the new phases, ferrite and cementite, forming with equilibrium concentrations, C^{α} and C^{C_m}. A carbon boundary layer is built up in front of the ferrite platelet and a depleted boundary layer forms in front of the cementite platelet. Carbon diffusion occurs due to the concentration gradients existing in the adjacent austenite. The rate at which carbon must be removed from in front of a ferrite platelet moving with velocity V, width S^{α}, and unit depth d is

$$VS^{\alpha}d(C^{E}-C^{\alpha}). \tag{1}$$

This amount of carbon must be carried away by diffusion given by

$$-D_c^{\gamma} \frac{\partial C^{\gamma}}{\partial x} S^{\alpha}d. \tag{2}$$

The concentration gradient can be estimated by

$$\frac{-\partial C^{\gamma}}{\partial x} \approx \frac{(C^{\gamma/\alpha}-C^{E})}{\delta_{\alpha}}, \tag{3}$$

with $C^{\gamma/\alpha}$ and δ_{α} defined in Fig. 1. Zener assumed δ_{α} to be nearly equal to $S_{\alpha}/2$ thus Equations 1 and 3 become

$$VS^{\alpha}d(C^{E}-C^{\alpha}) = D_c^{\gamma}\frac{(C^{\gamma/\alpha}-C^{E})}{S^{\alpha}} \frac{S^{\alpha}}{2} d. \tag{4}$$

A similar expression can be derived for the cementite platelet,

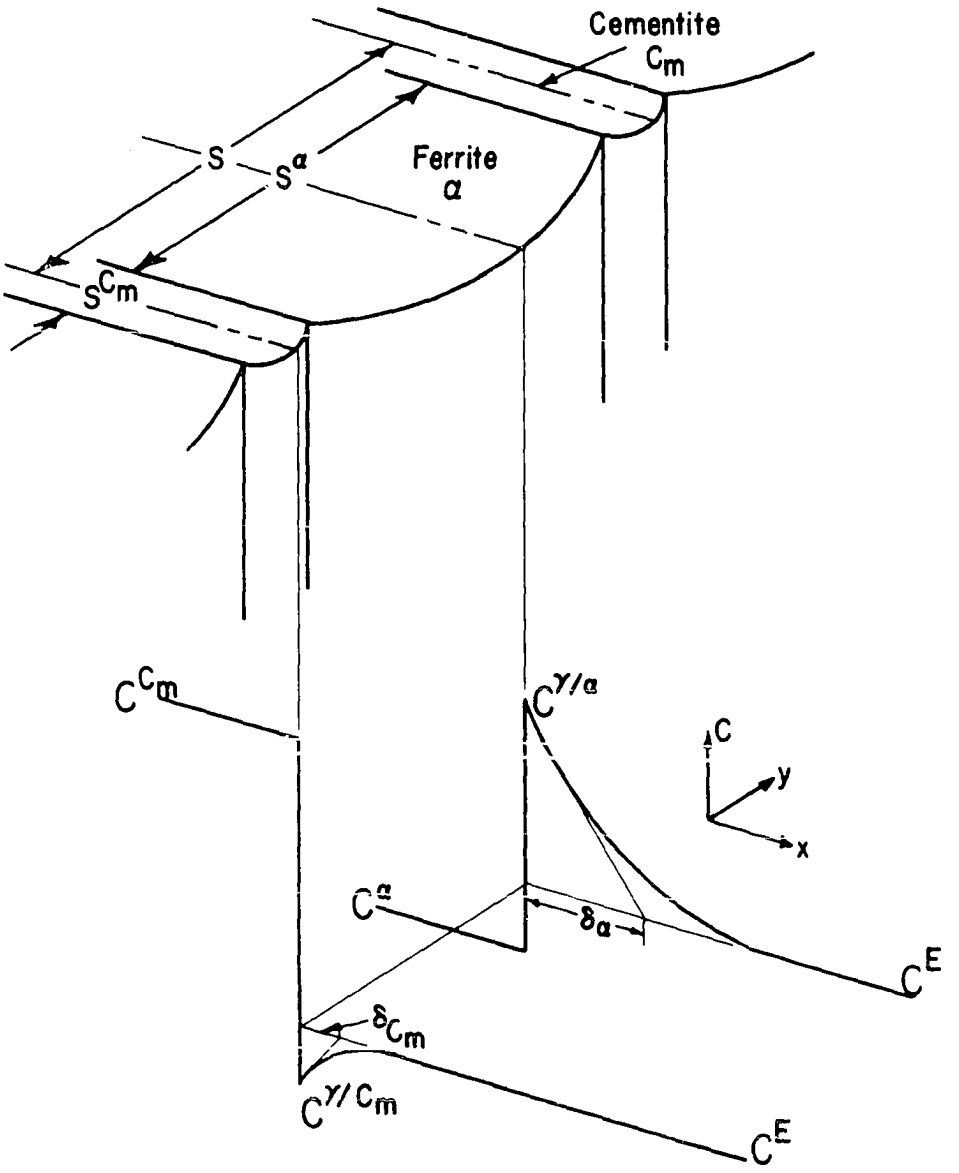

Fig. 1. Schematic illustration of pearlite growth front defining characteristic dimensions and carbon concentrations

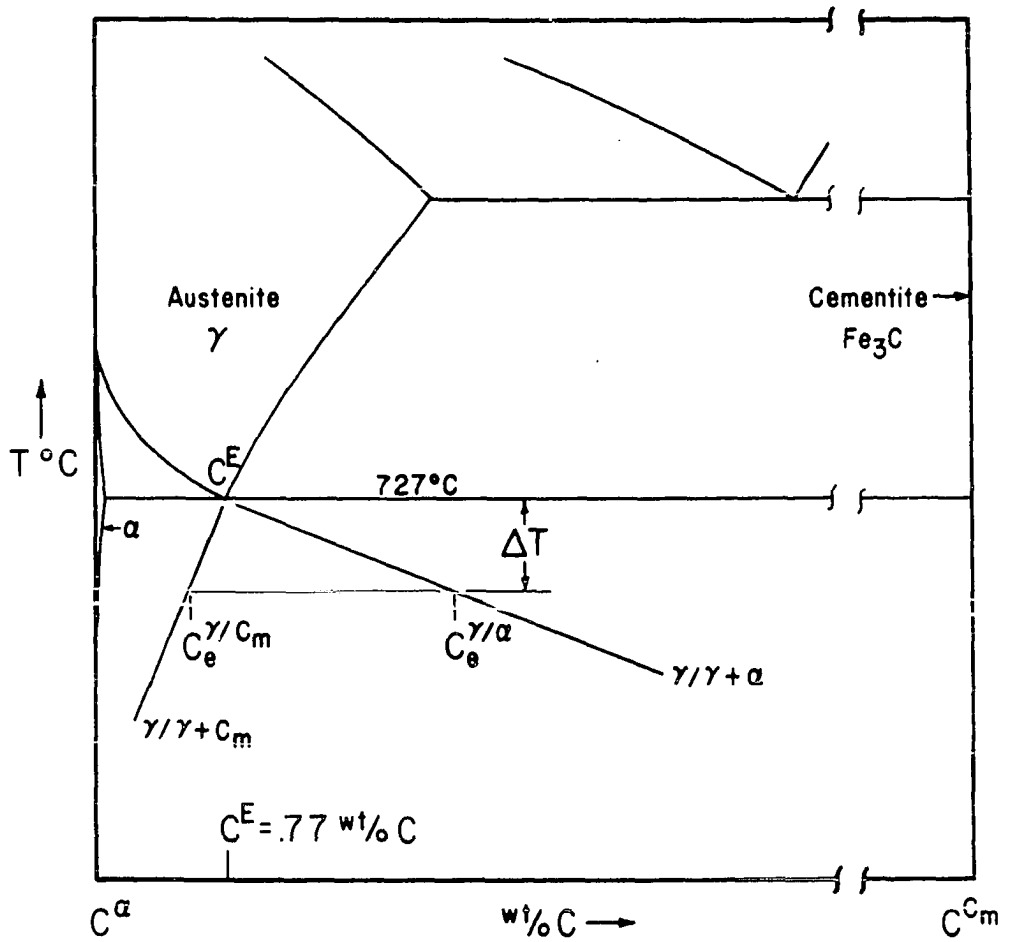

Fig. 2. Hultgren extrapolation of $\gamma/\gamma+\alpha$ and $\gamma/\gamma+C_m$ phase boundaries in the Fe-C system

$$VS^{C_m} d(C^{C_m} - C^E) = D_c^{\gamma} \frac{(C^E - C^{\gamma/C_m})}{S^{C_m}} \frac{S^{C_m}}{2} . \quad (5)$$

If the specific volume between the three phases is equal, then the lever rule can be applied yielding the following relations between spacing and concentration,

$$\frac{S^{\alpha}}{S} = f^{\alpha} = \frac{(C^{C_m} - C^E)}{(C^{C_m} - C^{\alpha})} ,$$

and

$$\frac{S^{C_m}}{S} = f^{C_m} = \frac{(C^E - C^{\alpha})}{(C^{C_m} - C^{\alpha})} . \quad (6)$$

Combining Equations 6 with Equations 4 and 5, the following equation for velocity results,

$$V = \frac{2}{f^{\alpha} f^{C_m}} \frac{(C^{\gamma/\alpha} - C^{\gamma/C_m})}{(C^{C_m} - C^{\alpha})} D_c^{\gamma} \cdot \frac{1}{S} . \quad (7)$$

Zener's main contribution was in the realization that the concentration difference $(C^{\gamma/\alpha} - C^{\gamma/C_m})$ would not be the equilibrium concentration difference suggested by the Hultgren (12) extrapolation of the phase diagram (Figure 2). Instead, the local equilibrium between austenite and the two product phases would be modified due to local curvature of the platelet tips. Zener suggested the concentrations $C^{\gamma/\alpha}$ and C^{γ/C_m} would be related to the equilibrium concentrations $C_e^{\gamma/\alpha}$ and C_e^{γ/C_m} through the Gibbs-Thompson equation given here for the ferrite platelet,

$$\Delta G = \frac{2\sigma^{\gamma\alpha} V_m}{r^{\alpha}} = RT \ln \frac{\gamma_{\alpha} C^{\gamma/\alpha}}{\gamma_e C_e^{\gamma/\alpha}} , \quad (8)$$

where $\sigma^{\gamma\alpha}$ is the interfacial energy, V_m is the molar volume, r^α is the radius of curvature of the interface, and γ_α and γ_e are activity coefficients. For small changes in concentration, $\gamma_\alpha = \gamma_e$ and the R.H.S. of Equation 8 can be approximated by

$$RT\frac{(C_e^{\gamma/\alpha} - C^{\gamma/\alpha})}{C_e^{\gamma/\alpha}} . \tag{9}$$

Therefore the deviation of the composition of the interface would be proportional to the curvature. Zener defined a critical radius of curvature, r_c^α, to be such that the interface concentration $C^{\gamma/\alpha}$ would be reduced to the bulk concentration C^E so that no diffusion could occur. Therefore, two equations for concentration as a function of curvature can be obtained,

$$\frac{2\sigma V_m}{RTr_c^\alpha} = \frac{C_e^{\gamma/\alpha} - C^E}{C_e^{\gamma/\alpha}} \tag{10}$$

and

$$\frac{2\sigma V_m}{RTr^\alpha} = \frac{C_e^{\gamma/\alpha} - C^{\gamma/\alpha}}{C_e^{\gamma/\alpha}} . \tag{11}$$

These two equations can be combined to give

$$(C^{\gamma/\alpha} - C^E) = [1 - \frac{r_c^\alpha}{r^\alpha}](C_e^{\gamma/\alpha} - C^E) . \tag{12}$$

A similar equation can be derived for curvature involving the cementite platelet

$$(C^E - C^{\gamma/C_m}) = [1 - \frac{r_c^{C_m}}{r^{C_m}}](C^E - C_e^{\gamma/C_m}) \tag{13}$$

Zener assumed that the ratios r_c^{α}/r^{α} and $r_c^{C_m}/r^{C_m}$ would be equal to a critical spacing ratio, S_c/S, and combined Equations 12 and 13 to form the equation,

$$(C^{\gamma/\alpha}-C^{\gamma/C_m}) = [1-\frac{S_c}{S}](C_e^{\gamma/\alpha}-C_e^{\gamma/C_m}). \qquad (14)$$

Substituting Equation 7 into Equation 14 yields the velocity equation in final form,

$$V = \frac{2}{f^{\alpha}f^{C_m}} \frac{(C_e^{\gamma/\alpha}-C_e^{\gamma/C_m})}{(C^{C_m}-C^{\alpha})} D_c^{\gamma}\cdot\frac{1}{S}\cdot[1-\frac{S_c}{S}]. \qquad (15)$$

Equation 15 is interesting in that it predicts a range of spacings and velocities for a given undercooling defined by $(C_e^{\gamma/\alpha} - C_e^{\gamma/C_m})$. This would be in contradiction to the uniform spacing and growth rate generally observed. Zener suggested the growth conditions would adjust to maximize the growth rate. Equation 15 predicts a maximum velocity when the spacing is twice the critical spacing, i.e. $S_{opt}=2S_c$. The dependence of spacing on temperature can be obtained by considering the partitioning of the free energy available for transformation between the formation of new interfacial area and losses due to diffusion. As can be seen in Figure 3, when the pearlite interface advances a distance δ, it generates surface area $2\delta d$ per unit volume δdS. The energy per molar volume is then

$$\Delta G_{surf} = \frac{2\sigma^{\alpha C_m} V_m}{S} \qquad (16)$$

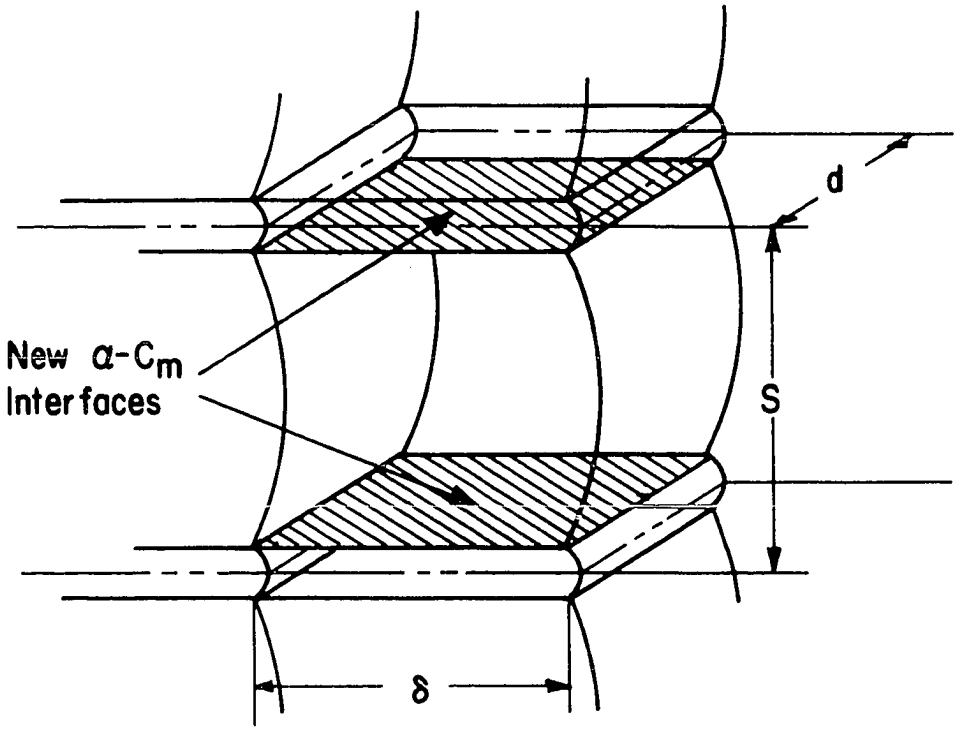

Fig. 3. The generation of α-C_m interfacial area during growth

It can readily be seen that this energy is maximum when S is at the minimum spacing, S_c. The overall free energy available for transformation can be obtained from the enthalpy of transformation per unit volume ΔH_v^T. Assuming ΔH_v^T is independent of temperature, the total free energy available for transformation is

$$\Delta G_{total} = \frac{\Delta H_v^T \Delta T}{T_E} , \qquad (17)$$

where ΔT is the undercooling below the eutectoid temperature, T_E. S_c and S are obtained by equating Equations 16 and 17.

$$S_{opt} = 2S_c = \frac{4\sigma^{\alpha C_m} T_E}{\Delta H_V^T \Delta T} = \frac{K_T}{\Delta T} . \qquad (18)$$

Finally, $(C_e^{\gamma/\alpha} - C_e^{\gamma/C_m})$ is defined by straight line extrapolations of the austenite phase equilibria, Figure 2;

$$(C_e^{\gamma/\alpha} - C_e^{\gamma/C_m}) = K_e \Delta T, \qquad (19)$$

and when Equations 18 and 19 are combined with Equation 15 the two kinetic equations are yielded

$$V = \frac{1}{f^{\alpha} f^{C_m}} \frac{D_c^{\gamma}}{C^{C_m} - C^{\alpha}} \frac{K_e}{K_T} \Delta T^2 = K_{\Delta T} D_c^{\gamma} \Delta T^2$$

and (20)

$$V = \frac{1}{f^{\alpha} f^{C_m}} \frac{D_c^{\gamma}}{(C^{C_m} - C^{\alpha})} \frac{K_e K_T}{S^2_{opt}} = \frac{K_s D_c^{\gamma}}{S^2_{opt}}$$

The two kinetic equations given above define qualitatively the kinetics of pearlite growth if rate is controlled by volume diffusion. The constants $K_{\Delta T}$ and K_s can be easily calculated and predict growth rates much smaller than generally observed (13,14). Improvement in the model can be made by refining the approximations made in developing Equations 20. First, the diffusion is not one dimensional as Equation 2 suggests and $C^{\gamma/\alpha}$ and C^{γ/C_m} vary along the edges of the ferrite and cementite platelets. Brandt (15) and Schiel (16) solved a two dimensional diffusion equation with arbitrary periodic boundary conditions for $C^{\gamma/\alpha}$ and C^{γ/C_m} at the interface plane. Hillert (17) solved similar diffusion equations

as Brandt and Schiel but improved the solutions by allowing the local curvature to specify the concentration at the boundary. However, these solutions depended on assuming D_C^{γ} constant with carbon concentration. Therefore, these solutions are in error since D_C^{γ} is known to vary widely with carbon concentration (18). Nevertheless, Hillert was able to make detailed calculations of interface shape and also to predict the average carbon concentration in the interface as a function of rate. The carbon concentration calculations are particularly useful since the functional form of D_C^{γ} in Equations 20 can be determined. Hillert realized his calculations may be in error due to his inability to treat D_C^{γ} analytically but assumed the error would be small. Hillert (17,19) was also able to treat Equation 18 in a more quantitative manner with more precise use of free energy functions and interfacial energies. Hillert's results do not alter the dependence of spacing on the inverse of the undercooling. The refinements of Hillert's work, unfortunately, could not account for the high pearlite growth rates observed.

Several modifications of Hillert's work have been made. Bolze et al. (20) accounted for the possibility of the new phases being slightly supersaturated so that observed spacings would be wider than those predicted by theory. However, no satisfactory treatment has been made concerning either the variation of carbon diffusivity with carbon content or the interface strain due to the volume change occurring upon

transformation. This last effect is particularly important since Sulonen (21) has shown that tensile strain increases the rate of discontinuous precipitation in Cu-Cd and the strain in austenite caused by the formation of pearlite may have appreciable effects on the growth rate.

Interface Diffusion

The model for interface diffusion assumes that the boundary between pearlite and austenite can be treated as a separate phase with thickness b and diffusivity, D_B. Turnbull (22) first applied the model to discontinuous precipitation in Pb-Sn but it is easily adaptable to the eutectoid reaction. The concentration, C_b, in the boundary is related to the concentration in the parent phase through a distribution coefficient, K. Thus, the concentration difference in the boundary between tips of a ferrite and cementite platelet would be

$$K(C^{\gamma/\alpha}-C^{\gamma/C_m}), \tag{21}$$

with the total mass flow in the boundary given by

$$\frac{D_B\ b\ K}{S/2}\ (C^{\gamma/\alpha}-C^{\gamma/C_m}). \tag{22}$$

Equation (22) can be combined with the mass flow equations

$$\tfrac{1}{2}VdS^{\alpha}(C^{E}-C^{\alpha}) = \tfrac{1}{2}VdS^{C_m}(C^{C_m}-C^{E}), \tag{23}$$

to give

$$V = \frac{4}{f^{\alpha}f^{C_m}}\ D_B\ b\ K\ \frac{(C^{\gamma/\alpha}-C^{\gamma/C_m})}{(C^{C_m}-C^{\alpha})}\cdot\frac{1}{S^2}\ . \tag{24}$$

Finally, applying Equation 14 the velocity as a function of spacing and the extrapolated phase equilibrium concentrations is given by

$$V = \frac{4}{f^{\alpha} f^{C_m}} D_B \; b \; K \; \frac{(C_e^{\gamma/\alpha} - C_e^{\gamma/C_m})}{(C^{C_m} - C^{\alpha})} \cdot \frac{1}{S^2} \left[1 - \frac{S_c}{S}\right] \qquad (25)$$

and with reasoning similar to that which lead to Equations 20 the following kinetic expressions are obtained:

$$V = K_{\Delta T}^{B} \; D_B \; \Delta T^3$$

and (26)

$$V = K_S^B \; \frac{D_B}{S^3} \; .$$

Therefore, the chief difference between the kinetic equations for volume diffusion and boundary diffusion is the exponent of ΔT and S, being 2 for volume diffusion and 3 for boundary diffusion.

Carpay (23) and Carpay and Van den Boomgaard (24) have studied eutectoid reactions in non-ferrous systems. They have observed that the spacing as a function of velocity appears to follow a $V = KS^{-4}$ relation. To account for this, they have developed a model similar to the one given above. Equation 25 can be written

$$V \propto \frac{D_B \Delta T}{S^2} \qquad (27)$$

with $(C_e^{\gamma/\alpha} - C_e^{\gamma/C_m}) \propto \Delta T$. They combine this equation with the experimentally determined relationship,

$$V \propto \Delta T^2 \qquad (28)$$

observed in eutectics and pearlitic transformations (10,13,14) to obtain the result:

$$V \propto D_B S^{-4}. \tag{29}$$

Unfortunately, this analysis results in the following relation for spacing as a function of undercooling:

$$S \propto \Delta T^{1/2}, \tag{30}$$

a result which is not supported by experimental observation (14,25).

As stated previously, the boundary diffusion model is attractive for explaining high growth rates through high grain boundary diffusivities. Puls and Kirkaldy (6) give arguments for grain boundary controlled growth in pearlite at high growth rates and large undercoolings. The growth kinetics of pearlite are described as changing from volume diffusion at high temperatures where carbon diffusivity in austenite is large and growth rates slow to boundary diffusion at faster rates and larger undercoolings where volume diffusivity decreases due to decreasing temperature. The boundary diffusion model has attracted many theoretical endeavors. Particularly interesting contributions have been made by Cahn (26), Hillert (19), Shapiro and Kirkaldy (27), and Sundquist (28,29). The chief disadvantage of the models has been the lack of systems where grain boundary diffusivities are known and the inability to treat the thermodynamics of a boundary in a satisfactory manner.

Optimum Growth

In order that the kinetic Equations 20 and 26 represent unique solutions, it was necessary to introduce some optimal growth principle. The one chosen was based on Zener's suggestion that the spacing would adjust in order to maximize the velocity if the undercooling is fixed. This is equivalent to minimizing the undercooling of the transformation interface in a temperature gradient when the velocity is fixed. However, the system may just as well adjust to optimize some other quantity. Cahn (26) has developed a model based on maximization of the rate of free energy release. On the other hand, Kirkaldy (30,31) has presented arguments in favor of maximum entropy production. The principle of maximum entropy production can be applied to the volume diffusion model in the following way. The net free energy can be obtained from Equations 16 and 17.

$$\Delta G = \Delta G_{total} - \Delta G_{surf} = \frac{2\sigma^{\alpha} C_m V_m}{S_c} \left[1 - \frac{S_c}{S}\right] \tag{31}$$

The rate of entropy production is then given by

$$\frac{dS}{dt} = -V \frac{\Delta G}{T} \propto \frac{1}{S}\left[1 - \frac{S_c}{S}\right]^2. \tag{32}$$

The entropy production rate is a maximum when $S = 3S_c$. This indicates that the stable growth condition is characterized by larger spacings at a somewhat reduced velocity than predicted by the maximum velocity principle.

Chalmers and Jackson in (32) have analyzed lamellar faults in eutectic growth and have proposed that stability of the growth front is governed by fault terminations in a lamellar structure. However, this does not account for the regular spacing observed in some fault free systems or how the system approaches the steady-state configuration. Perturbation analysis provides a method of testing a particular configuration for stability but again does not yield information as to how the steady-state configuration is achieved. Puls and Kirkaldy (6) have reviewed current theory and have concluded that there is no single optimum configuration but rather a spectrum of states grouped around some optimum growth mode. The optimum is never reached because the driving force to alter the interface configuration becomes less as it approaches the "ideal" state. Nevertheless, it is possible to talk about the average behavior of the system when it is constrained in some manner such as isothermal or isovelocity growth.

There have been attempts (33,34) to determine the optimization constant in the equation

$$S = KS_c. \tag{33}$$

However, the critical spacing, given by Equation 18, depends on thermodynamic data which are not precisely known. Thus, the calculated values of S_c have a range equal to the theoretically predicted values of K and as such, a definite selection of the correct optimization principle cannot be made.

PREVIOUS EXPERIMENTAL WORK

The growth of pearlite is of particular commercial interest because it is linked directly to the hardenability of quenched and tempered steels. As a result, there have been extensive studies of pearlite growth in alloy steels but few studies, by comparison, of high purity binary eutectoid steels. In addition, the studies of pearlite growth kinetics have often omitted an important parameter; e.g. growth rates are measured as a function of temperature but spacing data are not reported. Because of the evolution of pearlite theory, many reviews (3,4,6) of experimental work have been published and no attempt will be made to duplicate them. Instead a discussion of the two approaches to kinetic data, i.e. isothermal and isovelocity, will be given with references to the most appropriate experimental findings.

Isothermal Growth

The general experimental technique for isothermal investigations is to austenitize specimens and transfer them to constant temperature lead baths. The specimens are small so that they equilibrate rapidly and are allowed to transform for various times with growth arrested by quenching in water. The specimens are prepared metallographically and determinations of spacing and velocity as a function of temperature are made. The growth rate can be obtained by two methods. First, specimens reacted for increasing periods of time at temperature

can be examined to determine the largest pearlite nodule at each time increment. A plot of size versus time will yield the velocity. The second technique employs statistical analysis of the size distribution of nodules as a function of time (14,35). Spacing determinations are not nearly as tedious, but care must be taken since individual lamellae may not be perpendicular to the plane of polish of the specimen. Spacing measurements are generally reported as the minimum observed spacing with the justification given that these represent the spacings from colonies with lamellae perpendicular to the surface; all other colonies not so aligned would indicate larger spacings. However, Pellisier et al. (25) have given evidence that the mean spacing is not the minimum observed spacing because of the statistical variation of the lamellae. They determined the mean spacing to be 1.65 times the smallest observed spacing. However, their results depend on graphical techniques involving measured areas as well as spacings which are subject to cumulative error.

Frye, Stansbury, and McElroy (13) determined growth rates by the maximum nodule technique but did not include spacing measurements. They observed the growth rate to increase with increasing undercooling with a maximum growth rate at 600°C. Further undercooling resulted in a decrease in the growth rate. Applying absolute rate theory (36) they found good agreement with the equation

$$V = K\Delta T^2 e^{-Q/RT}, \tag{34}$$

with Q = 24.2 kcal/mole. This is the same form as the volume diffusion model (Equation 20) when the diffusivity is treated by a simple Arrhenius relation,

$$D_C = D_o e^{-Q/RT} \tag{35}$$

Since the activation energy for carbon diffusion in austenite is greater than 24 kcal for carbon contents near the eutectoid composition, they conclude that carbon diffusion in austenite is not rate controlling. Brown and Ridley (14) measured growth rates by both the maximum nodule technique and the statistical analysis of nodule size distribution. The two techniques yielded velocities similar to those reported by Frye et al. However, the statistical analysis of the nodule size distribution indicated the velocity from nodule to nodule was not constant but instead nodules nucleating first grew faster than those nucleating later. They attributed this to orientation effects, but did not include experimental verification. Their spacing data as a function of temperature compared favorably with Equation 18 thus supporting Zener's thermodynamic arguments. Brown and Ridley analyzed their growth velocity data in a similar fashion as Frye et al. and determined the activation energy Q to be 24.6 kcal/mole. They also calculated the apparent diffusivity and compared this with extrapolated diffusivities of carbon in austenite determined by Wells et al. (18). They conclude that carbon dif-

fusivity alone could not be rate controlling. However, they did not account for variation of carbon content in the austenite adjacent to the pearlite interface as a function of rate; a result predicted by Hillert's (17) analysis. As a result, their interpretation of Q which is a strong function of carbon concentration is perhaps misleading. A review by Puls and Kirkaldy (6) of both sets of data indicates that the data supports volume diffusion when account is taken of the dependence of D_C^{γ} on carbon concentration.

Isovelocity Growth

Intending to remove the ambiguities of velocity determination by isothermal techniques, Bolling and Richman (8) extended the early research of Bramfitt and Marder (37) on isovelocity growth of pearlite. By pulling a specimen through a steep temperature gradient, the pearlite forms along an isothermal front in an analogous fashion to directional solidified eutectics (38). However, because large undercoolings are associated with eutectoid growth, large gradients are required to suppress nucleation ahead of the advancing growth front. The required gradient in the austenite, G_γ, will depend on the interface temperature, T_i, the eutectoid temperature, T_E, the incubation period, τ, when nodular pearlite first forms and the velocity V. G_γ is defined by the relation

$$G_\gamma = \frac{(T_E - T_i)}{\tau V} \tag{36}$$

The product τV decreases with increasing velocity, therefore the severest gradient requirement will occur at maximum velocity. The continuous cooling experiments of Marder and Bramfitt (34) indicate for V = 100 μm/sec; T_i = 580°C and τ = 10 sec. Therefore, the critical gradient for no nucleation is ~1500°C/cm. Bolling and Richman maintained a gradient of 2500°C/cm in their experiments and were able to directionally transform pearlite from .01 to 2100 μm/sec. The results of spacing measurements over this velocity range indicated an exponential dependence on S (Equation 20 and 28) equal to 2.47 $\pm$ .12. However, if their data is examined between the ranges of 1 to 100 μm/sec, the exponent is 2 and increases to 3 for rates greater than 100 μm/sec. They conclude that volume diffusion may explain the slow growth data with interface diffusion becoming important for faster rates. Chadwick and Edmonds (39) reported n equal to 2.7 $\pm$ .11 for a limited number of velocities between 0.1 and 100 μm/sec, while Cheetham and Ridley (40) indicate n = 2 for 9 velocity determinations between 3 and 13.2 μm/sec. Carpay (9) has questioned whether the pearlite can be forced to grow under steady-state conditions at high growth rates. If pearlite forms via the same mechanism in isothermal growth as in isovelocity growth, then pearlite should not be able to be forced to grow at rates faster than those observed isothermally.

Two of the goals of this study were to determine the temperature of the growth interface in a temperature gradient at

fixed velocity and to determine the maximum velocity that pearlite can be forced to grow. If the same velocity, temperature, and spacing data are obtained as in isothermal growth, then it is likely that pearlite forms via the same mechanism in both instances.

EXPERIMENTAL PROCEDURE

The systematic study of the pearlite reaction by directionally decomposing austenite in a steep temperature gradient requires certain stringent conditions. First, iron-carbon alloys of desired composition must be prepared with sufficient purity and compositional accuracy so that derived results may be compared with confidence to theory and the results of other investigators. Second, equipment must be obtained which will produce gradients with sufficient stability and magnitude so that the pearlite reaction occurs under truly steady-state conditions. And finally, an experimental methodology is required which will efficiently produce the desired data with the greatest amount of precision. The following sections contain descriptions of how these requirements were achieved.

Alloy Preparation

Two sources of high purity iron were used in the production of Fe-C eutectoid composition (.77 wt % C) alloys for this study. The majority of alloys were prepared from iron supplied by Materials Research Corporation. The MRC iron was analyzed and a list of significant impurities is contained in Table 1. A second series of alloys was prepared from iron of substantially higher purity donated by the AISI Product Properties Subcommittee. This iron was produced at Battelle Memorial Laboratories by zone refining in various purifying atmospheres (41) and contained not more than 25 ppm impurities.

Table 1. Analysis of impurity content of MRC iron

Element	Ames[a]	Ames[b]	Element	Ames[a]	Ames[b]
Al	5	--	N	11	
C	20		Nb	5	--
Ca	14	--	Ni	10	ft
Co	160	vw	O	380	
Cr	10	t	P	15	--
Cu	12	t	S	60	--
Ge	4	--	Si	2	--
Mn	2	--			

[a]Impurity content is in ppm by weight. O and N were determined by vacuum fusion techniques at the Ames Lab. C was determined by neutron activation by MRC. All other determinations were by mass spectrographic techniques at the Ames Lab.

[b]Qualitative analysis by DC spectrographic techniques determined at the Ames Lab. ft = faint trace, t = trace, vw = very weak, -- = tested for but not found.

The decision to use alloys of two different purities was based solely on economics. The Battelle iron had a market value of nearly thirty times that of the MRC iron and was limited in quantity. Thus the MRC alloys were used for development of the experimental techniques and the interface temperature measurements. The Battelle alloys were reserved for the investigations of lamellar spacing and maximum velocity of pearlite where direct observation of microstructural defects were indicative of the pearlite reaction and not due to impurities. The difference in impurity content will undoubtedly have a small effect on the austenite to pearlite interface temperature but to a much smaller degree than the experimental error of measurements. On the other hand, the microstructural

observations made on the Battelle alloys are strictly resolved from any impurity interpretation.

All alloys were prepared by arc-melting iron with carbon in the form of spectrographic rod. Small pre-weighed 200 gm charges were placed in an arc-melting chamber together with a separate zirconium button. The chamber was evacuated and back filled with argon. Oxygen was gettered from the system by arc-melting the zirconium button. The alloy charge was arc-melted repeatedly with the alloyed button inverted after each melting operation to insure homogeneity. The final melting operation was in a cylindrical mold cavity which yielded an elongated finger that facilitated further forming operations. The finished finger was removed from the chamber and reweighed. A small but significant weight loss was observed in the MRC alloys. This was attributed to either small beads of iron spalling off during alloying or the reaction of carbon with the dissolved oxygen in the iron. For eutectoid composition alloys, the 380 ppm oxygen content of the MRC iron is sufficient to reduce the carbon content by .008 to .015 wt % C depending on the formation of CO or CO_2 during alloying. To insure against carbon loss, all MRC alloys were weighed slightly in excess of the eutectoid composition.

Each arc-melted finger was sealed in an evacuated quartz tube and homogenized at 1000°C for 72 hours. The finger was hot swaged to 7.62 mm diameter, cut into 10 cm lengths, and centerless ground to 6.35 mm diameter. The samples were then

resealed and again austenitized at 1000°C for 24 hours and cooled to room temperature. Carbon determinations made on nine samples randomly selected at this stage yielded an average carbon content of .77 wt % C with a standard deviation of .015 wt %. Samples were finished machined or further heat treated as described in the following sections.

Equipment

Suitable equipment for very rapid heat transfer is necessary for maintaining the high thermal gradients required for steady-state pearlite transformation at a planar interface. After considerable trial and error, the system consisting of two cooling fixtures and induction coil diagramed in Figure 4 proved to be the most efficient and reliable design. The four turn work coil was made from 4.8 mm soft copper tubing covered with irradiated PVC shrink tubing insulation. Power to the coil was provided by a Westinghouse 25 kW Dual Frequency Radiofrequency Generator equipped with a saturable core reactor. The saturable core reactor effectively smoothed the power output to the generator so that a very stable heating was achieved. However, there was no way to inhibit line voltage fluctuations which were the limiting factor in absolute stability. Nevertheless, embedded thermocouples in the samples showed the maximum temperature to be stable within $\pm$ 3°C over a period of a half hour. The work coil was wound around a mandrel with the same o.d. as the Pyrex tube used to separate

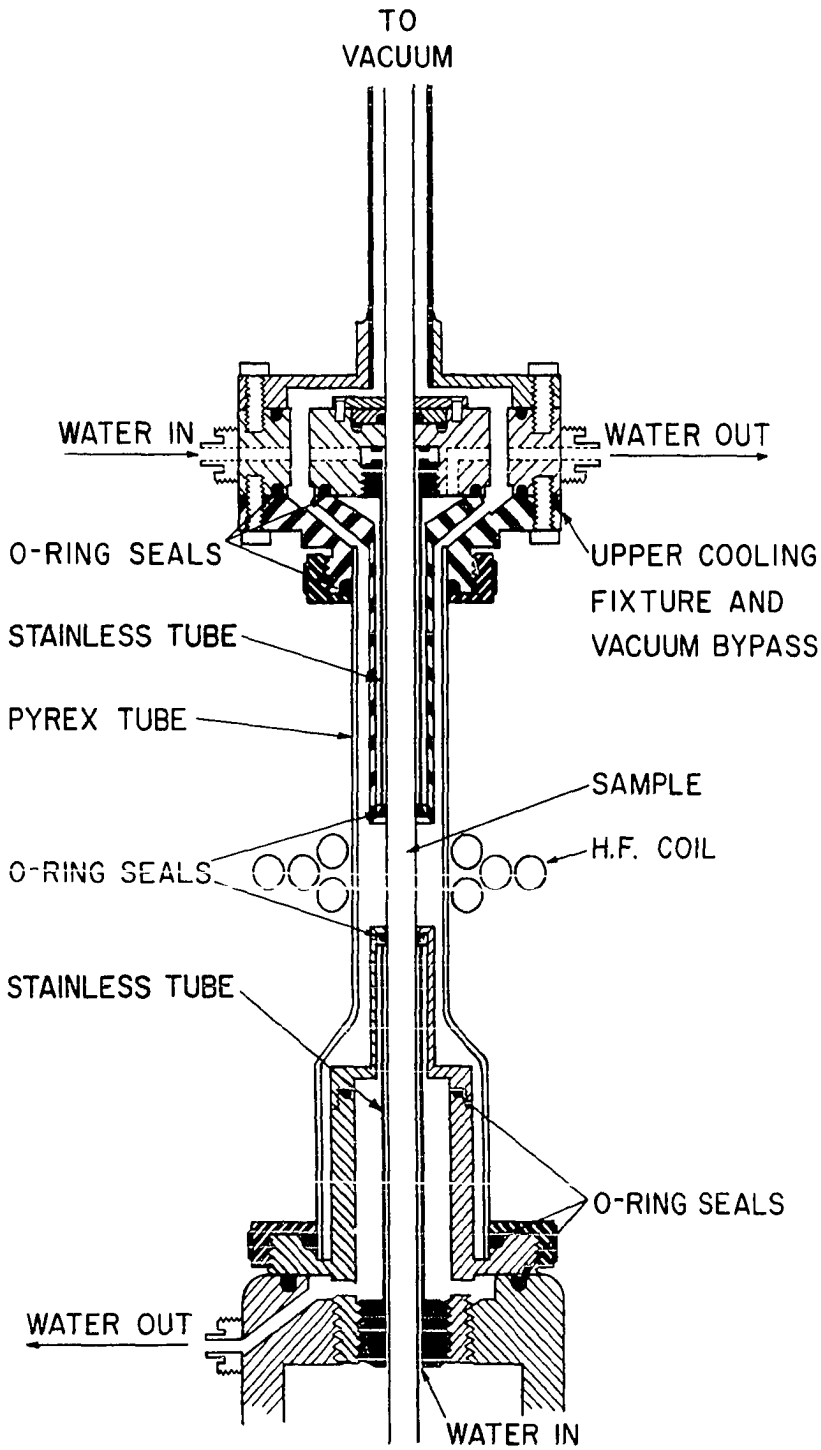

Fig. 4. Sectional view of the cooling fixtures and induction coil used to obtain high thermal gradients

the two cooling fixtures and thus was brought as close as possible to the sample to achieve good coupling. In addition to fixing the distance between the two cooling fixtures, the Pyrex tube could be evacuated and back filled with argon so that the sample could be protected against decarburization during heating.

The two cooling fixtures were constructed so that the sample and o-rings directly adjacent to the heated zone could be cooled efficiently and thus provide the required gradients without o-ring failure. The parts of the cooling fixtures nearest the heated zone as well as the o-ring seats were machined from OFHC copper. This insured that these areas were not heated inductively and that the o-rings were cooled as much as possible by conduction. The o-ring seats were silver soldered to stainless steel tubes with a series of small holes drilled just behind the seats. The tubes could be adjusted so that the samples could slide freely through the o-rings and still maintain a good seal. In addition, the stainless tubes served to channel incoming cooling water along the sample and through the holes near the o-ring seats so that these areas were cooled very effectively. The upper fixture was also designed so that a vacuum could be pulled through it and thus evacuate the Pyrex tube.

The two cooling fixtures and the work coil were mounted on an aluminum carriage shown in the photograph in Figure 5.

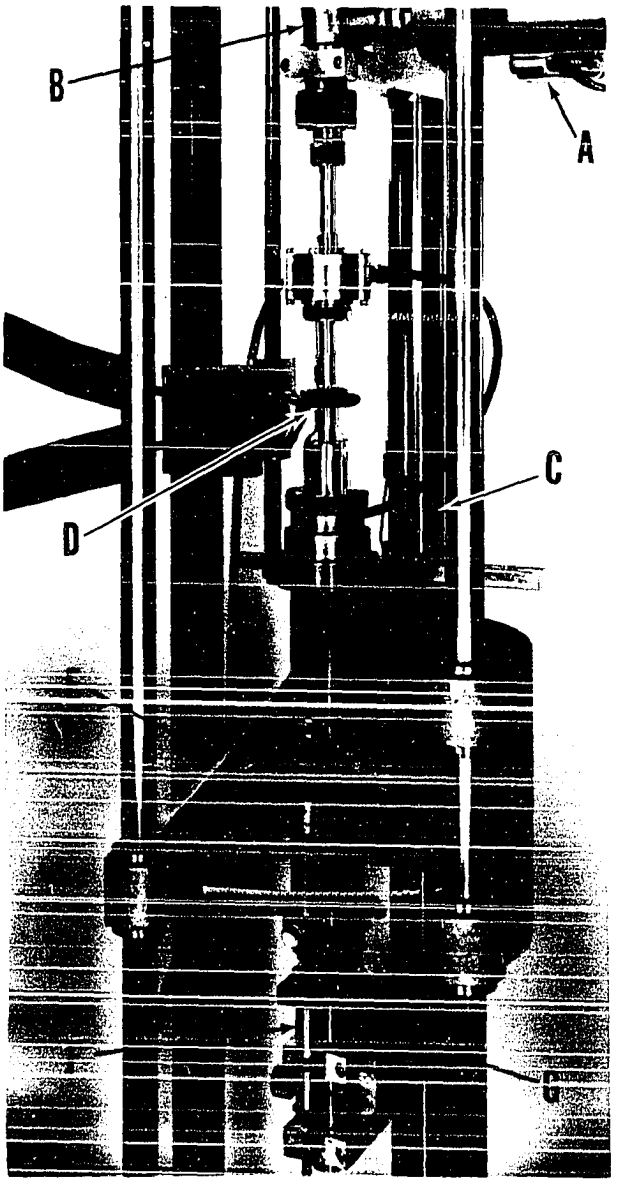

Fig. 5. Transformation apparatus. A) Drive motor (transmission not shown), B) Vacuum header, C) Drive screw, D) Induction coil and cooling fixtures, E) Carriage, F) Differential transformer, G) Sample support rod

The carriage was guided by three hardened steel rods and could be translated at various rates by a screw driven by synchronous motor and transmission. The sample was fixed to a stainless steel post extending into the lower cooling fixture. The carriage and the two cooling fixtures together with the work coil moved vertically along the length of the sample. A Daytronic DS200 differential transformer was mounted on the stainless steel post and was used to measure the relative motion of the carriage. By recording the output of the transducer on a chart recorder, an accurate determination of carriage velocity could be made. In addition, any stallings or erratic movements of the carriage which lead to interruptions or bands in the microstructure of the transformed pearlite would be recorded. This was particularly useful when gradients were measured with a thermocouple. Using a two pen chart recorder, with the transducer output on one channel and the thermocouple output on the other, any change in slope of the recorder gradient would signal a phase change and would not be due to erratic carriage motion if the transducer indicated smooth translation.

Interface Temperature

The temperature of the interface between austenite transforming to pearlite in a temperature gradient can be determined by taking advantage of the difference in thermal conductivity between the two phases. A simple heat flux balance

normal to the interface plane yields the equation

$$k_\gamma G_\gamma + V\Delta H_V^T = k_p G_p \qquad (37)$$

where k_γ and k_p are the thermal conductivities of austenite and pearlite, G_γ and G_p are the respective thermal gradients, ΔH_V^T is the enthalpy of transformation per unit volume, and V is the imposed velocity. For the velocities and gradients used in this study, the $V\Delta H_V^T$ term is approximately two orders of magnitude smaller than the conduction terms. Therefore, the ratio of the gradients in the two phases will be given by the relation

$$\frac{G_\gamma}{G_p} = \frac{k_p}{k_\gamma} \; . \qquad (38)$$

Powell and Hickman (42) have determined the ratio k_p/k_γ to be 1.25 indicating a 25% change in gradient at the interface which is large enough to be easily detected. A marked change in gradient as determined from a calibrated thermocouple moving with the sample would yield the temperature of the pearlite interface.

The sample and thermocouple configuration are schematically diagramed in Figure 6. The sample was tapped on one end with a 1.6 mm hole drilled to a depth of 5 cm from the other end. In addition, the hole end was threaded and an o-ring seat was machined to form a seal with a 6.35 mm diameter stainless steel tube. The tube was necessary to support the thermocouple and provide a vacuum or inert atmosphere

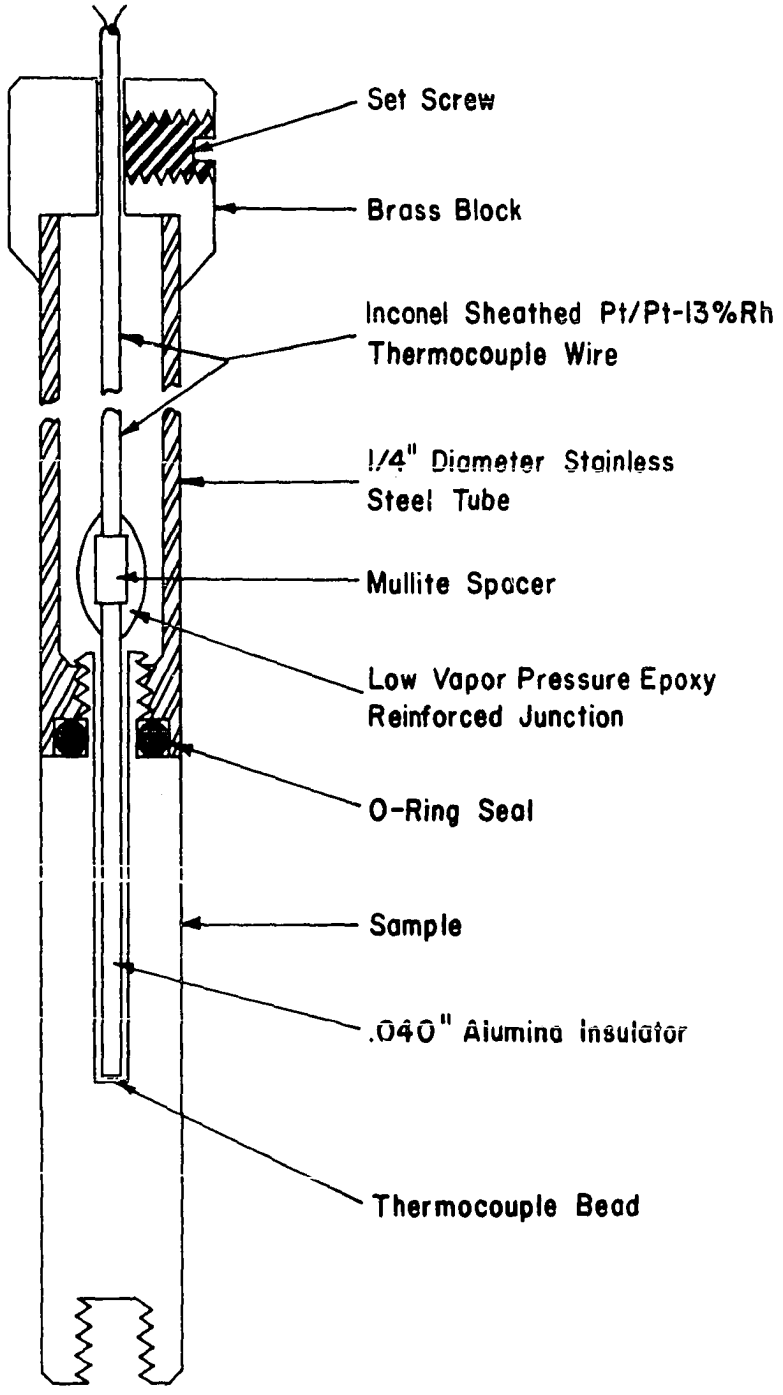

Fig. 6. Schematic diagram of thermocouple and sample assembly

around the thermocouple. The main body of the thermocouple was an approximately 60 cm length of 0.81 mm o.d. Inconel sheathed Pt vs. Pt-13% Rh thermocouple wire. This was threaded through a vacuum o-ring seal and the stainless tube. One end was permanently fixed to a standard thermocouple connector. To the free end were welded two lengths of .13 mm Pt and Pt-13% Rh wire using an oxy-hydrogen microtorch. A 13 mm length of 3 mm o.d. mullite insulation was slipped over the welded areas followed by a 6.4 cm length of 1 mm o.d. alumina insulation. The two insulators were drawn tight against the Inconel sheath and the junction was reinforced with low vapor pressure epoxy resin. The two free ends of .13 mm Pt and Pt-13% Rh wires were welded to make a small bead at the end of the alumina insulator. To insure maximum sensitivity to changes in temperature, the bead was filed to .08 mm thickness using 600 grit sandpaper.

The thermocouple was inserted in the sample and the stainless steel tube was screwed in place. It was important that the alumina insulation be able to slide freely in the sample because of the difference in thermal expansion between the two materials. If the alumina fit in the hole too tightly, it would bind causing the bead to move relative to the sample during heating which produced erratic output. To insure good thermal contact between the sample and the bead, pressure was applied to the thermocouple tip. The sheath emerging from the brass block shown at the top of Figure 6 was gripped in a vice

and forced into the tube thus springing the thermocouple tip against the bottom of the hole. The set screw was tightened keeping pressure on the thermocouple. The thermocouple bead would eventually diffusion bond with the sample after some period of use as can be seen in Figure 7. This indicates that ideal thermal contact occurred between the sample and the bead.

The completed thermocouple assembly was placed in the transformation apparatus with the output connected to an ice junction and chart recorder. The chamber was evacuated to 10^{-3} torr and the cooling water was turned on. High frequency power was slowly applied by increasing the impressed voltage over the work coil via the saturable core reactor control until the sample reached 1000°C. This vaporized any silicon o-ring lubricant on the sample surface. Power was reduced and turned off and argon was admitted to the system to a positive pressure of 6.9 kPA. Power was then reapplied with the power control fully advanced with a maximum temperature of 1250-1300°C achieved.[1] The drive mechanism was turned on and the temperature was recorded as a function of position. At the end of each traverse, the power was turned off and the carriage returned to the starting position. Each sample was transformed for as many times as possible. After each transformation, the sample surface became more irregular due to volume changes occurring during transformation. In addition, the sample surface was

---

[1]A detailed description of how proper load matching was achieved is given in Appendix A.

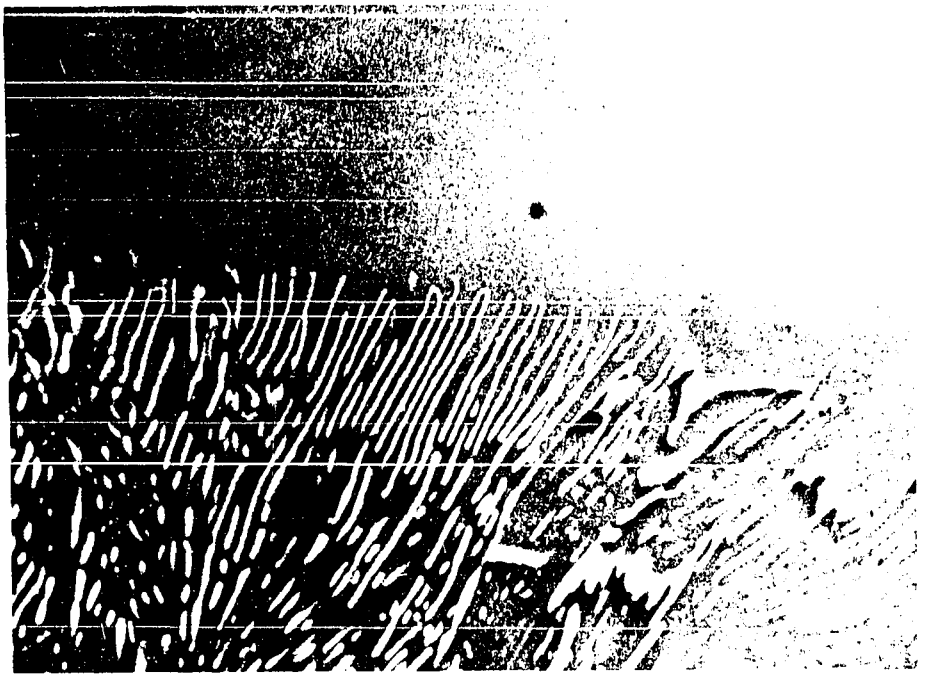

Fig. 7. SEM micrograph of bond between Pt vs. Pt 13% Rh thermocouple bead and Fe-C eutectoid sample. 8000X

Fig. 8. Photograph of austenite zone quenched in place after directionally transforming to pearlite. a) Directionally transformed pearlite, b) Quenched austenite zone (black band is surface nucleated pearlite on small austenite grains), c) Untransformed portion of sample. Arrows indicate austenite to pearlite and austenitizing interfaces

cleaned periodically because of surface contamination and roughness caused by rusting of the sample by the cooling water. The useful life of a sample was dictated by surface irregularities which became severe enough to prevent the o-rings from sealing properly. It should be noted however, that these irregularities were small compared to the bulk of the sample and had no observable effect on the gradient determinations. With each new sample, a rate previously recorded was repeated to insure continuity in data taken from one sample to the next.

Pearlite structures occur in isothermally transformed samples over a temperature range of 500 to 727°C. This temperature range corresponds to an output of 4.4 to 7.0 mV from a Pt vs Pt 13% Rh thermocouple. To properly locate a sharp change in thermal gradient required 2 to 3 mV of information on either side of the break. This could easily be obtained from a chart record with 5 mV span. Suppression required to center the break was applied by a Leeds-Northrup K-3 potentiometer which was also used to calibrate the chart recorder. Once calibration of the chart recorder was completed, the potentiometer and the recorder were not turned off until all the data had been taken. Calibration was checked periodically but further adjustments were not necessary. This proved to be the most precise method of getting good reproducibility from one sample to the next. Examples of a typical change in gradient can be seen in Figures 9 and 10. To determine the interface temperature, a line was drawn through the thermocouple

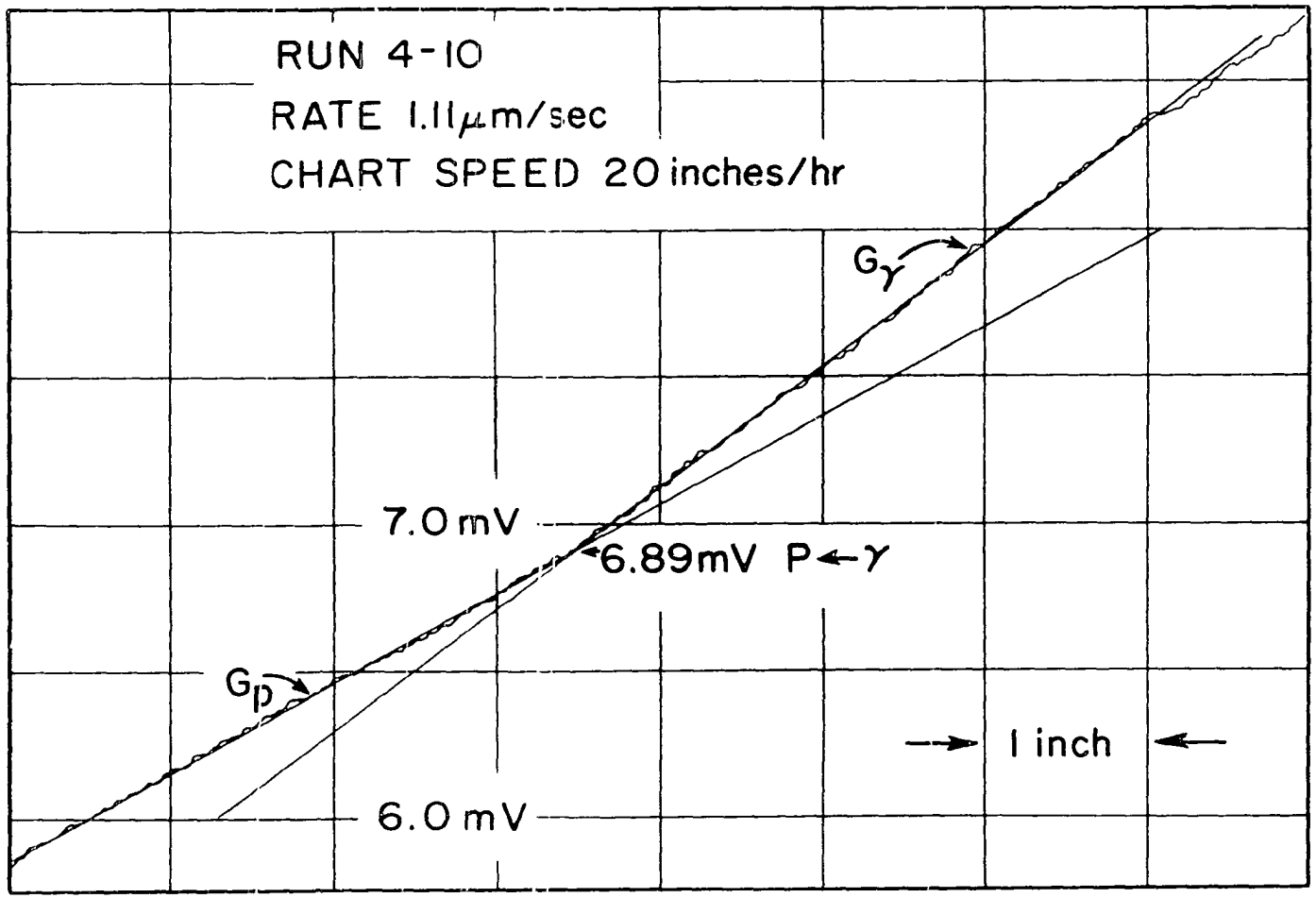

Fig. 9. Chart record of thermocouple output of sample transformed at 1.11 μm/sec

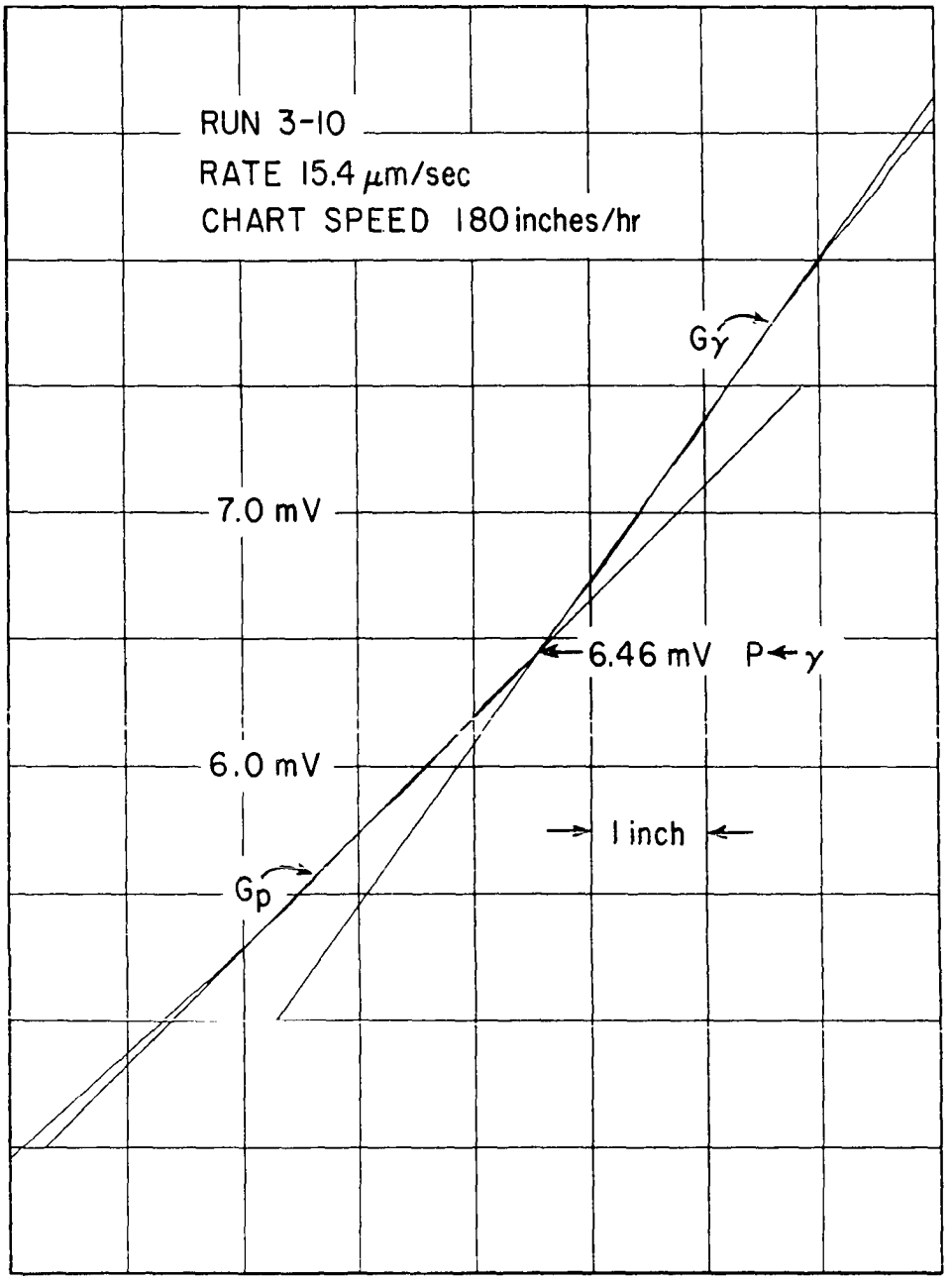

Fig. 10. Chart record of thermocouple output of sample transformed at 15.4 μm/sec

traces on each side of the apparent break. The intersection of the two lines was taken as the interface temperature.

All thermocouples were prepared from the same starting materials. Calibration of the thermocouples was determined by two methods. First, after the useful life of two of the sample assemblies was completed, the entire assembly was calibrated against the melting point of aluminum. Each of the assemblies was placed in a thin graphite tube which was inserted in a block of pure aluminum. The aluminum was melted under argon in an inductively heated graphite crucible. The output of the thermocouple was connected to the same equipment used to record the thermal gradients. The aluminum was allowed to solidify with the recorded freezing plateau used for calibration. The second technique took advantage of the austenitizing interface which occurs when the prior eutectoid structure is pulled through the heated zone. An identical change in gradient occurs as discussed for the austenite to pearlite transformation.[1] Breaks were observed for rates from 1.11 to 106 μm/sec with no apparent superheating. The average of all the breaks was calibrated against the eutectoid temperature of Fe-C.

---

[1]A description of the microstructure observed at the austenitizing interface and a discussion of certain subtleties of using a thermocouple of finite size to record a sudden change in slope of a thermal gradient is given in Appendix B.

The difference between the two calibration techniques was 4.5°C but preference was given to the calibration using the Fe-C eutectoid temperature. This preference was chosen since the calibration was made in the identical manner in which the austenite to pearlite determinations were made. In this way, a self consistent calibration of the interface temperatures was obtained.

Interlamellar Spacing

Samples prepared from the Battelle iron were simply drilled and tapped on one end and placed in the transformation apparatus. For rates from 25 to 106 μm/sec, the period of time that the sample was in the austentizing zone decreased from 7 to 2 minutes. Samples designated for these rates were given an additional quench and temper heat treatment to produce a fine carbide distribution which would readily homogenize during the correspondingly shorter heating times. Each sample was transformed for a distance of 3.8 cm except for the slow rates of 1.11 and 2.2 μm/sec which were transformed only 1.9 cm. At the end of each traverse, power to both the work coil and the drive mechanism was switched off instantly. This effectively quenched the austenitic zone and preserved the steady-state growth interfaces. The samples were polished and etched in Nital to reveal the quench interfaces. A photograph of a characteristic sample in this condition is shown in Figure 8. It is evident that both the austenitic and pearlitic

growth interfaces are macroscopically flat.

A metallographic longitudinal sample was prepared from each quench zone for microstructural investigation of the steady-state growth interfaces. In addition, five transverse sections from the transformed portion were prepared for spacing determinations. The five transverse sections were mounted in electrically conductive copper filled diallyl phthallate thermal setting plastic. The samples were mechanically polished and etched with Picral. All spacing measurements were made with the aid of a Stereoscan S-4 scanning electron microscope (SEM). The magnification of the SEM was calibrated using carbon replicas of standard ruled gratings. The replicas were fixed to the plane of polish of the samples using silver conductive paint. The mounted specimens were placed in the SEM so that the plane of polish was normal to the electron beam. This insured that the spacing measurements were not altered by perspective and that all observations were made parallel to the growth direction. The carbon replica was first brought into focus and a photograph taken to calibrate the magnification. Except for fine focusing, the lens settings were not altered so that the calibration remained unchanged. Focusing of each specimen in the mount was achieved by moving the stage vertically to bring the plane of polish into the original plane of the replica.

Prior observations on longitudinal sections indicated that individual pearlite colonies did not necessarily align

perfectly with the pulling direction. Instead, colonies were observed to grow within 30° of the growth axis. To insure that spacing measurements were made only on those colonies ideally aligned, several precautions were taken. First, in any field of view containing several individual colonies, only those exhibiting the smallest average spacing were included in the count. The others were assumed to be growing at an angle to the surface thus indicating slightly larger spacing. In some cases, it was possible to take advantage of the ability of the SEM to produce a three dimensional image to ascertain if the individual carbide lamellae, which were etched in relief, were normal to the surface. Finally, only those colonies having regular spacings extending over ten or more lamellae were included in the count. Twenty measurements were made on each of the five sections for a total of 100 measurements for each rate.

Maximum Rate of Growth

Samples used for these experiments were identical to those prepared for the spacing determinations. The samples were placed in the transformation apparatus with the austenitized zone held for two hours. The zone length was approximately 10 mm and contained very large grains of austenite, on the order of 2-3 mm. Traverse was started at a low rate between 5 and 10 μm/sec to develop a steady-state growth front of pearlite. At the end of 2.5 mm of transformation, the rate

was increased to greater than 100 μm/sec. At this point, the pearlite growth front was in the area of greatest austenite grain size. This was particularly important, for if pearlite were not able to grow at the high velocities then the growth front would gradually drop lower in the temperature gradient until the M_s temperature was reached and martensite formed. The necessity of large austenite grain size was to prevent any prior austenite grain boundary from interfering with the pearlite growth front. The high pulling rate was continued until all of the original austenitized zone was consumed. A longitudinal section of the sample was prepared by standard metallographic techniques. The start and rate change interfaces could be easily identified as can be seen in Figure 18. Special attention was placed on observing martensite which would indicate that pearlite was not transforming at steady-state at these velocities. The distance between the rate change interface and any interfaces between the fast growth pearlite and martensite was recorded.

RESULTS AND DISCUSSION

The results of the pearlite interface temperature determinations and the interlamellar spacing measurements as a function of transformation rate are summarized in Table 2. The temperature data in this table were derived from 60 recorded gradients obtained from samples fabricated from the same alloy. The Pt vs. Pt 13% Rh thermocouple used to record the gradients was calibrated using the austenitizing interface temperature. The precision and error associated with this technique are discussed in Appendix B. The original uncorrected thermocouple readings of both interfaces are contained in Appendix C.

The Dependence of the Pearlite Interface Temperature on Rate

The undercooling of the pearlite transformation interface as a function of imposed velocity was fit to the power curve $V = a(T_E-T_i)^n$ by least squares analysis. The resulting equation was

$$V = 8.17(10^{-3})\Delta T^{1.99}\ \mu m/sec \qquad (39)$$

where $\Delta T = T_E-T_i$. The quality of the fit of the data to this equation is illustrated in the plot of log V vs. logΔT in Figure 11 and in the statistical correlation coefficient, r, which was .997. A 95% confidence interval for both the preexponential term and the exponent is listed in Table 5. However good this fit may be, it is worth noting that a problem associated with the least squares analysis which resulted in

Table 2. Summary of interface temperature and interlammelar spacing data

Transformation rate μm/sec	Interface temperature $\gamma \rightarrow P$ °C	Undercooling $T_E - T_i$ °C	Average spacing S_{avg} μm	Minimum spacing S_{min} μm
1.11	715±3	12±3	.58 ±.070	.48 ±.020
2.20			.38 ±.032	.33 ±.018
4.43	705±3	22±3	.31 ±.036	.26 ±.010
7.70			.22 ±.025	.19 ±.0086
10.8	687±5	40±5	.20 ±.030	.17 ±.0077
15.4	682±3	45±3	.16 ±.016	.14 ±.0077
24.7	669±3	58±3	.15 ±.025	.12 ±.0074
34.4	655±3	72±3	.11 ±.016	.095±.0047
48.7	651±3	76±3	.10 ±.016	.078±.0070
56.4	646±5	81±5	.095±.015	.075±.0057
67.4	641±4	86±4	.083±.012	.068±.0036
83.6	623±6	104±6	.065±.0086	.054±.0038
106.0	606±6	121±6	.067±.0094	.055±.0016

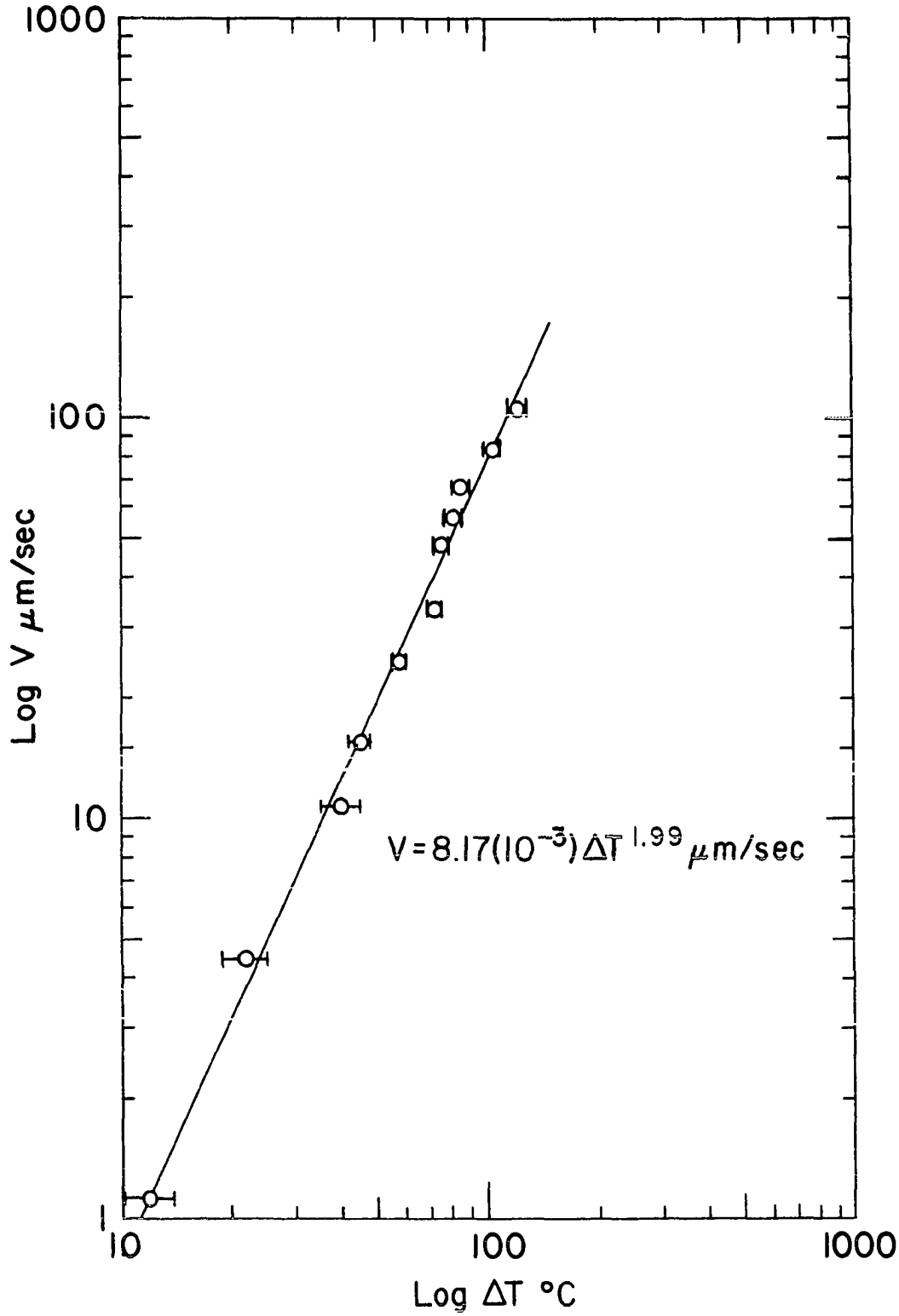

Fig. 11. Logarithmic velocity vs. interface undercooling

Equation 39 is that the proportional error in each ΔT is assumed equal and the statistical weighting of each term is the same. Actually, the proportional error in ΔT increases as the undercooling decreases if the random error in T_i remains constant. Thus, for the slowest rate of transformation, 1.11 μm/sec, for which the average undercooling is 12°C, the random error of $\pm$ 3°C in T_i results in a proportional error in ΔT of 25%. For larger undercoolings, the proportional error in ΔT for the same random error of $\pm$ 3°C is correspondingly smaller.

A further problem of interface temperature measurements made at slow transformation rates is that the random error in T_i may be larger than for faster rates. The increase in error is associated with the correspondingly longer time periods in which the gradient is being recorded. If the power to the sample changes appreciably during this period, the resulting changes in the temperature gradient would cause shifts in the temperature being recorded as the thermocouple passes through the transformation interface. The resulting shifts in the recorded temperature gradient may lead to larger random error in the interface temperature, obtained by extrapolation of the austenite and pearlite temperature gradients, than what would occur for faster translation rates.

A second and more serious source of gradient or temperature fluctuations results from the translation apparatus

itself. A problem associated with the o-rings used to seal the cooling water from the heated zone of the sample is that there was a tendency for the o-rings to stick to the sample at slow transformation rates. This caused the carriage to move in a step-wise motion that could easily be detected using the differential transformer mounted on the carriage. The effect of the hesitant motion of the carriage was detected by the thermocouple as can be seen in the chart recording in Figure 9. The range in temperature oscillations is 2-5°C and the period of the oscillations is 8-16 sec. The rate of change of temperature of any point in the gradient ranges from 0.1 to 0.6 °C/sec which when divided by the gradient (G_γ in this example is 1760°C/cm) gives a variation of the velocity of the isotherms in the sample of ~0.6 to 3 μm/sec. The time average of the velocity of the isotherms is the translation rate of the sample. The low end of the range corresponds to the carriage being stalled by the o-rings sticking to the sample and the high range to the point where the carriage pulls free. The net effect is that the sample is not transforming under ideal steady-state conditions. The interface temperatures for 1.11 μm/sec were reproducible so the effect of the oscillating motion was probably small; however, for slower rates, the oscillations would be larger and it would be difficult to transform the specimen at steady state. For this reason, 1.11 μm/sec was the lowest transformation rate used in this study.

The effect of a $\pm$ 5°C systematic error in the average undercoolings on the least squares analysis used to obtain Equation 39 is shown for various ranges of velocity in Table 3. It is interesting to note that the exponent remains nearly equal to 2, especially in the velocity range of 34.4 to 106 μm/sec. The most likely source of systematic error is in the calibration of the thermocouple. If calibration of the thermocouple were based on the melting point of pure aluminum (Appendix B), the interface temperature would be reduced by 4.5°C. This would nearly correspond to the -5°C error listed in Table 3. There is significance only when ΔT is small. For the velocity range of 10.8 to 106 μm/sec, the resulting equation is virtually identical to Equation 39. Therefore, the interpretation of the interface temperature data and its comparison to theory and previous experimental work, is not seriously jeopardized by the method of calibration of the thermocouple.

Table 3. Effect of a $\pm$ 5°C systematic error in ΔT on the least squares fit to the power function $V = a\Delta T^n$

$\Delta T = \Delta T_{obs} \pm 5°C$	Range of velocities fitted μm/sec	Fitted equation μm/sec	Correlation coefficient r
+5°C	1.11 - 106	$2.03(10^{-3})\Delta T^{2.27}$	.996
+5°C	10.8 - 106	$2.14(10^{-3})\Delta T^{2.26}$	.990
+5°C	34.4 - 106	$6.48(10^{-3})\Delta T^{2.02}$	.995
-5°C	1.11 - 106	$38.9(10^{-3})\Delta T^{1.66}$	.994
-5°C	10.8 - 106	$11.4(10^{-3})\Delta T^{1.94}$	.992
-5°C	34.4 - 106	$20.1(10^{-3})\Delta T^{1.82}$	.957

The Dependence of the Interlamellar Spacing on Rate

Two characteristic spacings were obtained for each rate. The first was simply an average of the 100 spacing measurements. This is presented in Table 2 as S_{avg} together with the standard deviation. The second treatment was an attempt to get the true minimum spacing characteristic of a given rate of transformation. The smallest 20 spacings of each data set were averaged and reported in Table 2 as S_{min}. The reason for averaging the smallest 20 spacings was that the distribution of the data set was skewed towards the larger spacings. The distribution should be normal if the lamellae of each colony are perpendicular to the surface. If, on the other hand, the lamellae intersect the surface other than at right angles, the effect would be to bias the distribution towards larger spacings. The apparent number of larger spacings increases because of the overlap of the smaller spacings being observed at an angle making them appear larger. The effect is shown qualitatively in Figure 12. It would be possible to calculate the exact shape of the skewed distribution if the distribution of plane normals at the lamellae of the pearlite colonies about the growth direction were known. However, this would involve an excessive amount of statistical analysis which would probably not yield a characteristic spacing which would be in serious difference to the two used in this study.

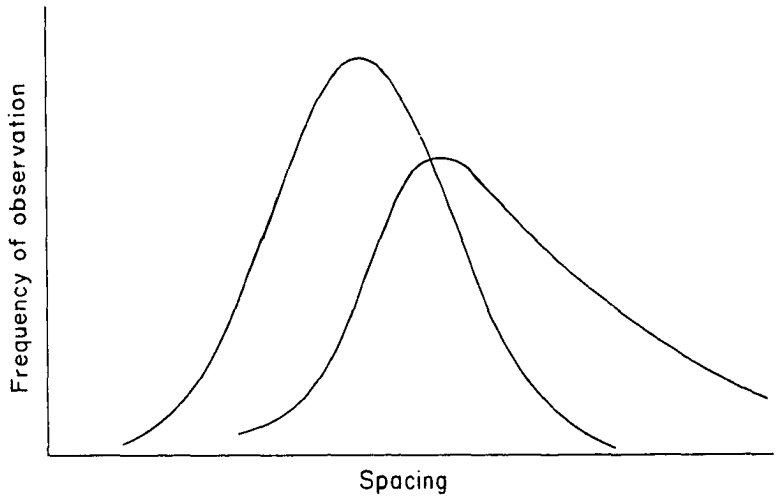

Figure 12. Relationship between a normal distribution and a skewed distribution

Figures 13 and 14 contain representative micrographs of some of the characteristic pearlite structures observed in cross section. The micrographs show that the area fraction of regular lamellar pearlite decreases as the transformation rate increases. The lamellar structure begins to degrade to a rod morphology for velocities in the range of 10 to 20 μm/sec. The coexistence of lamellar and rod forms within a single colony as seen in Figure 13c is typical of this velocity range. At higher velocities, the rod and degenerate structures begin to dominate with lamellar structures accounting for only 10-15% of the area fraction from 80-100 μm/sec. Also, portions of the fine lamellar structure characteristic of the high rates appear to coarsen during cooling in the gradient after forming as evidenced by Figures 14a and 14b. Nevertheless, the large regular

Fig. 13. Micrographs of typical pearlitic structure observed transverse to growth direction. a) Ferrite tracing prior austenite grain boundary. Rate: 2.20 μm/sec; light micrograph; 500X. b) Regular pearlitic structure characteristic of low velocities. Rate: 2.20 μm/sec; SEM micrograph; 1,100X. c) Rod and lamellar pearlite within single colony. Rate: 15.4 μm/sec; SEM micrograph; 6,100X. d) Regular pearlitic structure surrounded by degenerate carbides. Rate: 10.8 μm/sec; SEM micrograph; 2500X. All samples etched with Picral

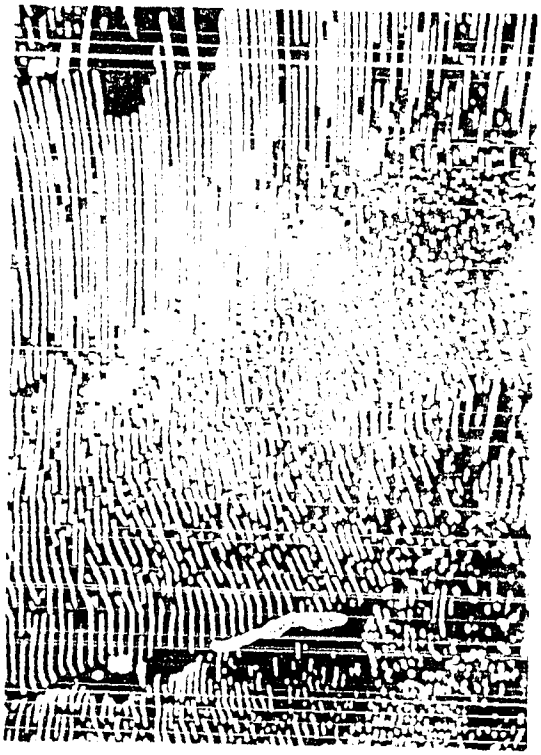

Fig. 14. Micrographs of typical pearlitic structure observed transverse to growth direction. a) Coarsening of lamellar carbides during cooling in gradient. Arrows indicate genesis of globular carbides. Rate: 83.6 μm/sec; SEM micrograph; 20250X. b) Similar coarsening as in (a); Rate: 83.6 μm/sec; SEM micrograph; 20250X. c) Typical isolated colony of regular pearlite surrounded by fine carbide dispersion. Rate: 83.6 μm/sec; SEM micrograph; 5060X. d) Typical pearlite colony representing approximately 10% of the microstructure at 105 μm/sec; SEM micrograph; 11,800X. All samples etched with Picral

1

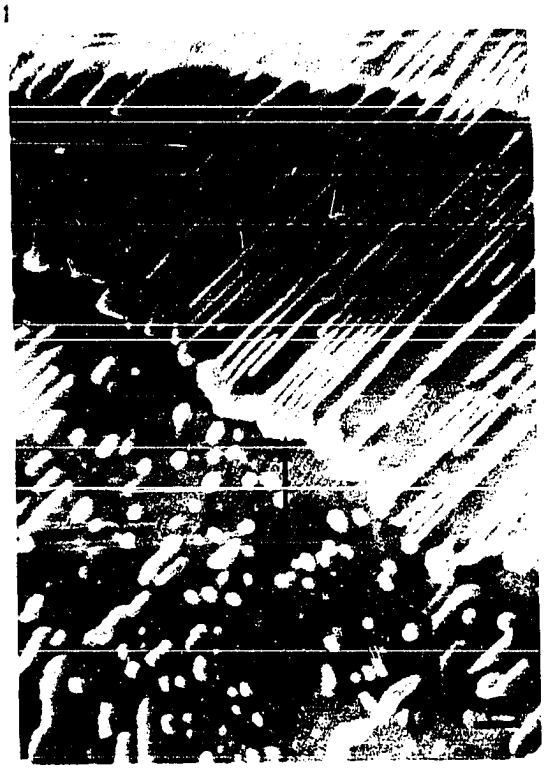

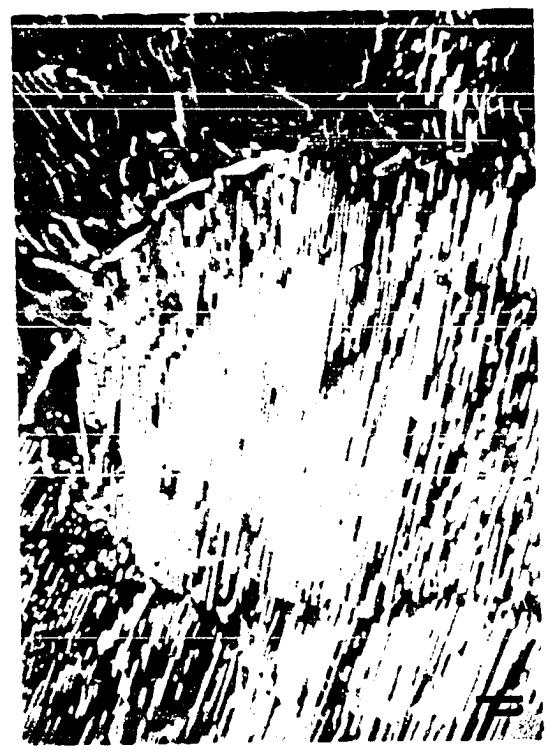

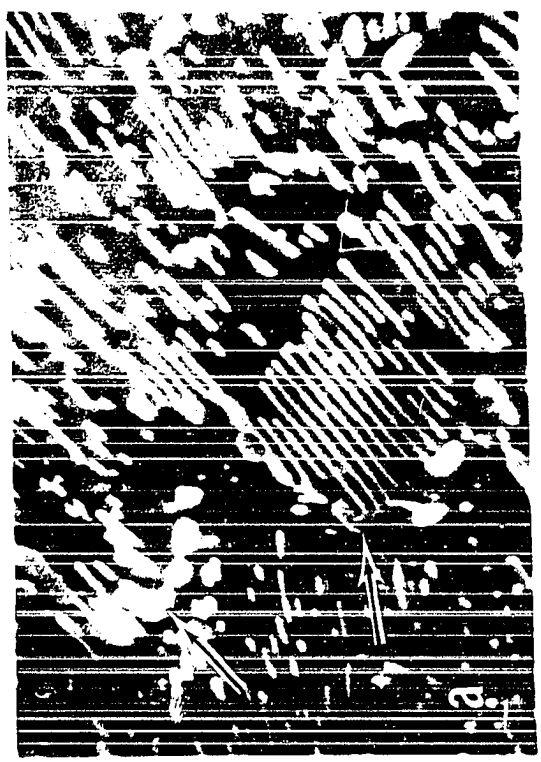

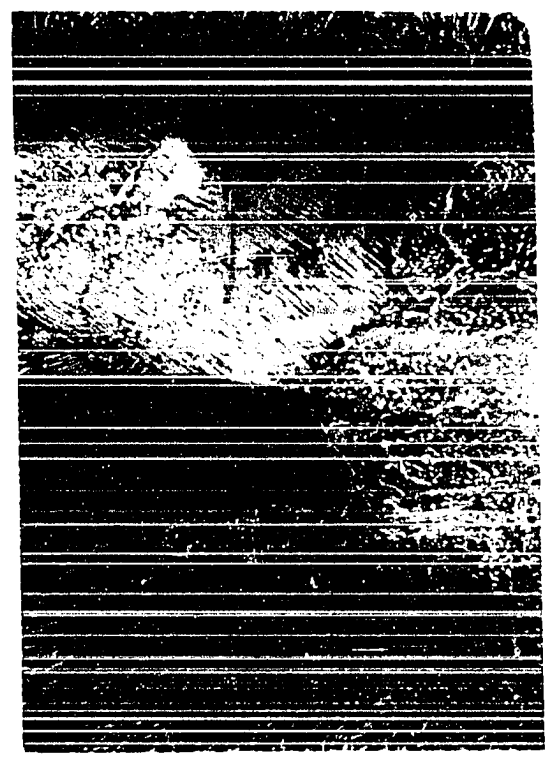

pearlite colonies shown in Figures 14c and 14d for the rates of 83.6 and 106 μm/sec respectively, were not atypical of these rates.

Both sets of spacing data as a function of translation rate were fit to the power curve $V = aS^n$ by the same least squares analysis used to obtain Equation 39. The resulting equations were

$$V = .346\ S_{avg}^{-2.11}\ \mu m/sec, \tag{40}$$

and

$$V = .256\ S_{min}^{-2.07}\ \mu m/sec. \tag{41}$$

The two sets of data are plotted together with the fitted equations in Figure 15. The two equations fit the data well as is evidenced by the correlation coefficient, r , which was .99 for the average spacing data and was .997 for the minimum spacing data. A 95% confidence interval for each of the pre-exponential terms and exponents in Equations 40 and 41 is listed in Table 5. A possible bias in the spacing data which would influence Equations 40 and 41 results from the disparity in area fraction of regular pearlite from the slow to fast rates. At the slow velocities, the observer has many regular colonies from which to select the smallest regularly appearing spacing. As the rate increases, the resulting loss in area fraction of pearlite decreases the range of selection. The net effect might be to skew the spacings at the slow velocities to smaller values thus increasing the absolute value of the ex-

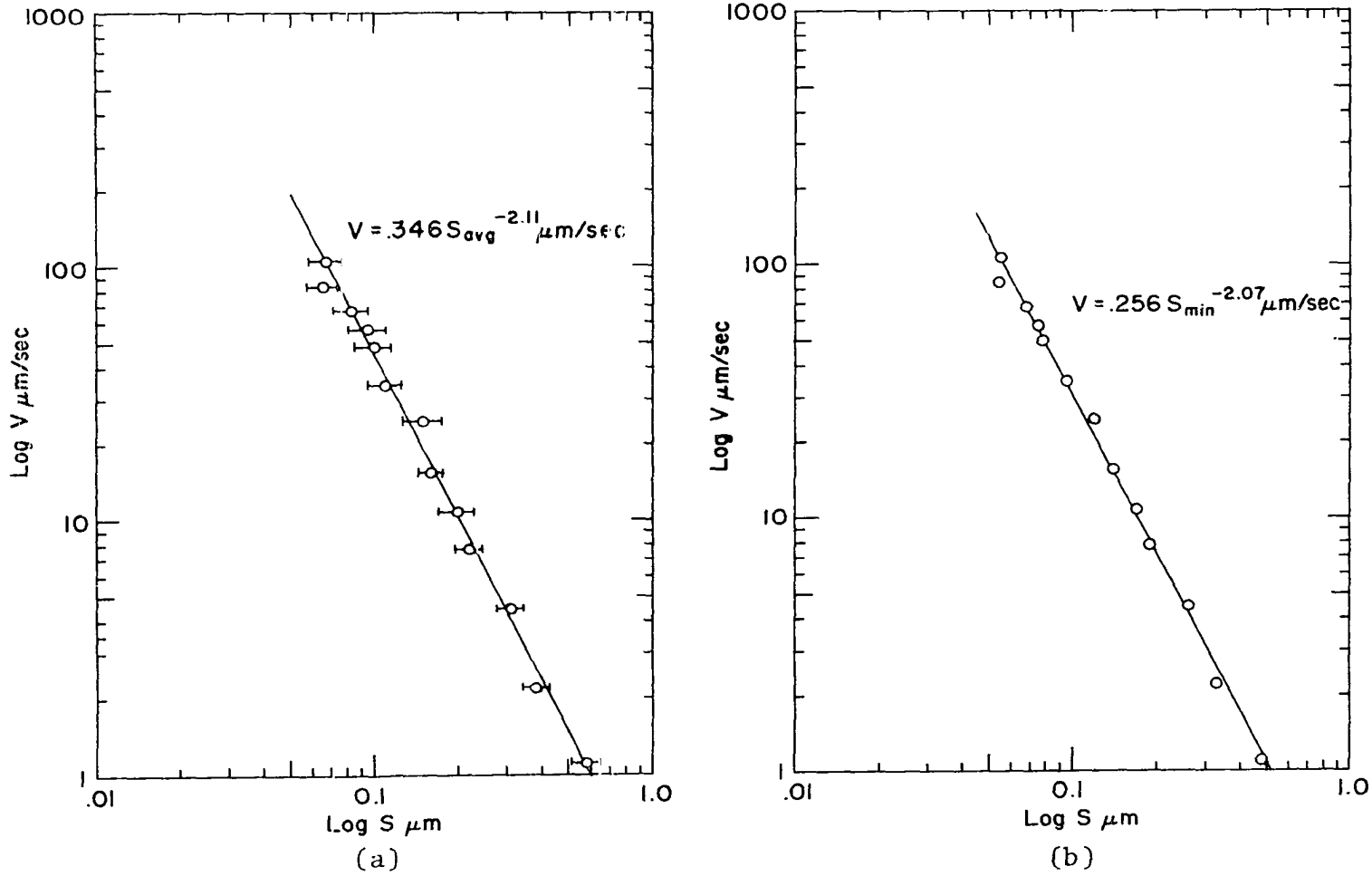

Fig. 15. Logarithmic velocity vs. interlamellar spacing. a) Average spacing, b) Minimum spacing

ponents in Equations 40 and 41. The biasing in the data is minimized by selecting the smallest spacings from the population sample and the net effect is the reduction in the absolute value of the exponent as can be seen by comparing these two equations.

The Microstructure of Directionally Transformed Pearlite

The directional eutectoid transformation of austenite to pearlite is not as effective as the directional solidification of eutectics in aligning the lamellae with the growth direction. Bramfitt and Marder (37) measured the angles of 200 lamellae with the growth direction of a high purity Fe-C eutectoid pearlite transformed at .71 μm/sec. They found that the distribution of lamellae peaked at 45° and that none of the lamellae were perfectly aligned with the growth direction. The micrograph in Figure 16a was taken from a longitudinal section of a sample transformed at 1.11 μm/sec. The band ahead of the growth front formed when the sample was quenched by instantly switching off the rf power. The lamellae have good alignment with the growth direction in regions A and C, but the alignment is poor at B. However, if the lamellae in region C are perpendicular to the plane of polish, and a new plane of polish is passed through region C perpendicular to the original plane of polish and parallel to the growth direction, the lamellae in C would appear perpendicular to the growth direction and would resemble region B. The true dis-

Fig. 16. Micrographs of typical pearlitic structure observed parallel to growth direction. a) Band of fine pearlite which forms during quench of samples transformed at low velocities. Rate: 1.11 μm/sec; light micrograph; 500X. b) Branching of cementite at beginning of quench band taken from region C of (a); SEM micrograph; 6000X. c) Effect of austenite grain boundary on pearlite growth. Arrows indicate areas where cementite lamellae have penetrated grain boundary without difficulty otherwise cementite platelets are stopped producing an excess of ferrite making boundary visible. Arrow (g.d.) indicates growth direction: Rate: 2.20 μm/sec; light micrograph; 500X. d) Similar effect of austenite grain boundary as shown in (c). Arrow indicates penetration of cementite lamellae through austenite grain boundary forming colony in upper grain. Rate: 2.20 μm/sec; light micrograph; 500X. All samples etched with Picral

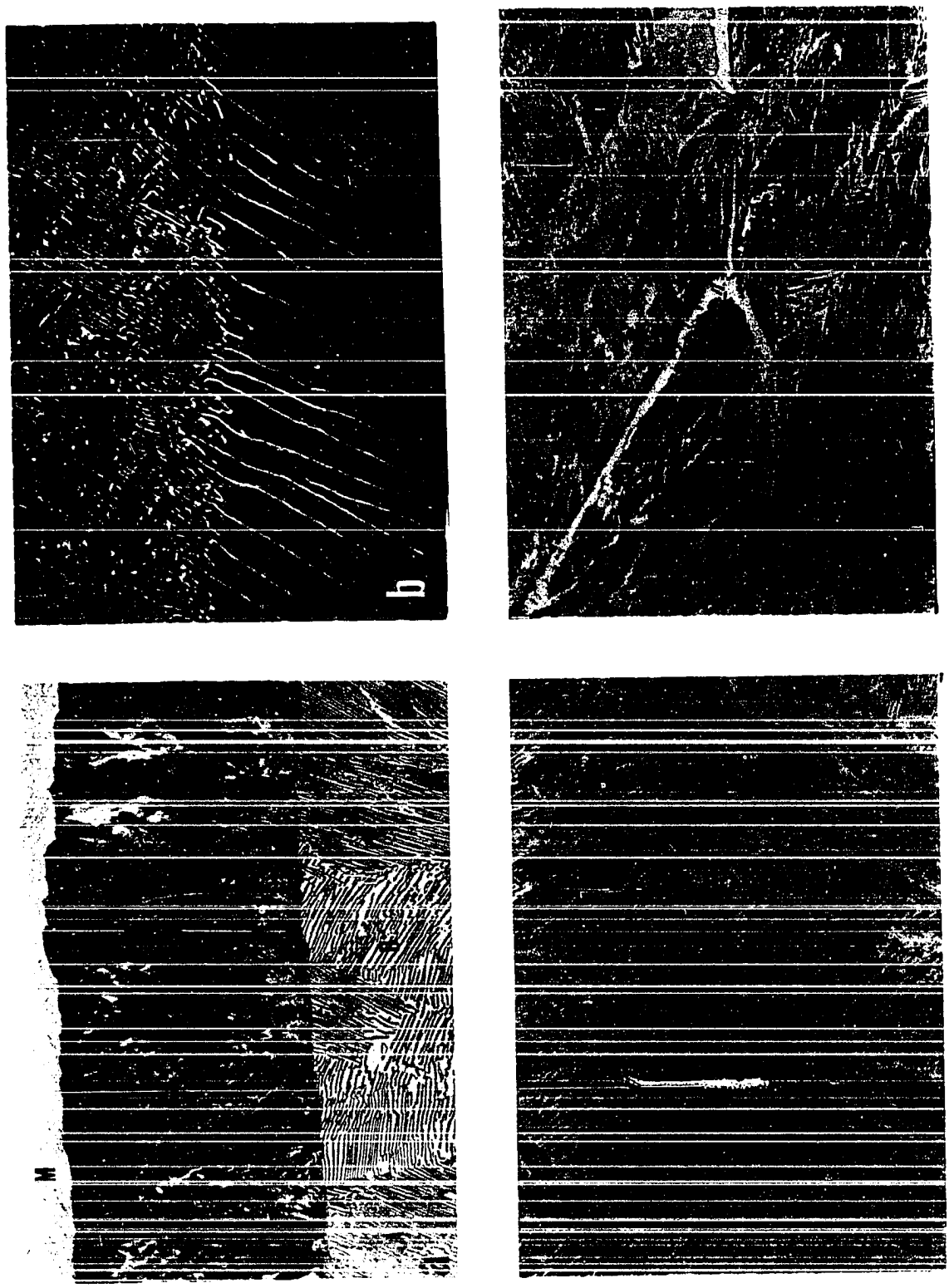
b

tribution of lamellar alignment about the growth direction can only be determined rigorously by two surface analyses. Hence, the actual alignment may be better than the results of Bramfitt and Marder indicate.

When a zone of austenite is passed through a sample, there are two transformation processes occurring. At the leading edge is the transformation to austenite and at the trailing edge is the transformation to pearlite. When the rf power is turned off, the austenitic zone is quenched in place as shown in Figure 8. The nature of the transformation to austenite at the austenitizing interface is discussed in Appendix B and several representative micrographs of the quenched interface are included in Figure B-3. The formation of the structure of austenite in the heated zone can be characterized by dividing the zone into three sections. The first section contains small grains of austenite which, because of the correspondingly high grain boundary area per unit volume and inhomogeneous carbon concentration, revert back to pearlite during the quench. This can be seen in the large band of surface nucleated pearlite in Figure 8. The center section of the zone is characterized by rapid grain growth as the sample is translated into the hottest part of the zone. These larger grains form martensite when the sample is quenched. The high temperatures achieved in the center of the zone were sufficient to cause considerable grain growth even for the fastest translation rates. The length of the zone was approximately 1 cm

so that at a rate of 106 μm/sec, a given element was austenitized for only 100 sec during passage through the zone. Nevertheless, this was sufficient time to produce austenite grains with ~.25 mm dia. The final section of the austenitized zone adjacent to the pearlite transformation interface is comprised of equiaxed grains of austenite having approximately the same grain size as the central region. It is somewhat surprising that there was no tendency to form elongated grains of austenite as a result of the directional passage of the heated zone.

The band in Figure 16a which formed in front of the growth front when the sample was quenched was determined by high resolution SEM microscopy to be fine pearlite. The spacing continually decreases in the band because of the rapid increase in the growth rate of pearlite occurring when the temperature of the interface decreases. The cementite branches almost instantaneously to produce smaller spacings as can be seen at the beginning of the quench band in Figure 16b. However, the branching and rate of growth cannot increase indefinitely and the structure becomes more irregular and eventually martensite forms (denoted by M in Figure 16a). Quench bands were observed at rates up to 48 μm/sec. At higher rates it became difficult to see the band because the change in spacing at the growth front, which produces the band during the quench, was small compared to the original structure.

Austenite grain boundaries were often observed as having a detrimental effect on the growth of pearlite. Figures 16c and 16d show that the cementite lamellae are frequently stopped at austenite grain boundaries. The ferrite apparently continues uninterrupted into the new austenite grain leaving the cementite behind. This would leave a thin line of ferrite tracing out prior austenite grain boundaries in the transformed pearlite; an effect often observed as evidenced by Figure 13a and Figures 16c and 16d. It is possible to determine the orientation of the ferrite at prior austenite grain boundaries and in adjacent pearlite colonies by applying Selected Area Channeling Pattern (SACP) techniques using a SEM. The orientation of ferrite at the boundaries could be compared with ferrite in adjacent pearlite colonies to see if indeed the ferrite grows into new austenite grains leaving cementite behind at grain boundaries. Figure 17 is a micrograph of a sample transformed at .51 μm/sec in order to produce the very coarse pearlite required by SACP techniques. The micrograph was taken at the quench interface and shows the competitive growth of two pearlite colonies along an austenite grain boundary. The cementite of the leading colony (colony A) is often stopped at the grain boundary. However, the ferrite is able to grow through the boundary since the large ferrite regions ahead of the cementite were shown by SACP techniques to have the same orientation as colony A. Careful

Fig. 17. SEM micrograph showing cementite lamellae being stopped at prior austenite grain boundary. Austenite grain boundary could be seen extending through quench band and into martensite (not shown). Ferrite within dashed line was shown by SACP to have same orientation as colony A. As electropolished. 1700X

examination of the micrograph shows that the cementite platelet tips thicken at the prior austenite grain boundary. This would indicate that considerable carbon transport to the cementite is occurring when the ferrite grows into the next grain. However, the cementite is effectively blocked by the austenite grain boundary and the ferrite eventually grows ahead of the cementite tips and stops any further thickening. It is interesting to note that when cementite does penetrate into an adjacent austenite grain, it does not change orientation markedly as can be seen in Figures 16c and 16d. This would indicate that there is no strong epitaxial relationship between cementite and austenite and makes an explanation of why cementite is stopped at grain boundaries a challenge. The observation of one colony leading another in Figure 17 was observed only rarely. However, the phenomena of cementite being stopped at grain boundaries was a common occurrence and was observed in samples transformed at all rates, although it was more prevalent at the lower velocities.

The Maximum Velocity of Pearlite

The analysis of the pearlite interface temperature and interlamellar spacing measurements as a function of rate assumed that pearlite could be forced to transform in a temperature gradient at an isothermal interface characteristic of the imposed velocity. The experimental procedure outlined on page 44 was designed to test the validity of this assumption at

high velocities (velocities in excess of 100 μm/sec). Extrapolation of the undercooling data in Figure 11 indicates that pearlite forced to grow at rates between 100 and 200 μm/sec should have an interface temperature between 550 and 600°C. Therefore, if the pearlite growth rate were suddenly increased from a value of around 5 μm/sec to 150 μm/sec, the transformation interface would continually drop in the temperature gradient until it coincided with the isotherm characteristic of the higher velocity. However, if pearlite were unable to grow at steady-state at the higher velocity, then the interface would continue to drop in the temperature gradient until some other ferrous structure characteristic of lower temperatures formed. In particular, the formation of martensite would be conclusive evidence that pearlite cannot grow at the high velocities since it forms below 200°C; well below the temperature range that pearlite can be expected to grow.

It is important to realize that in order for the pearlite growth front to adapt to the increased velocity, the spacing must be able to decrease to the characteristic size of the new velocity. If pearlite cannot change spacing efficiently during the initial transient to the new velocity, the growth front will not reach its steady state configuration; the cooperative nature of the lamellar growth will be lost, and growth will be stopped by the inability of the interface to respond to the rate change. On the other hand, if the pearlite interface can easily produce finer spacings within the

initial transient, the growth front will be able to reach the steady-state configuration characteristic of the high velocity if growth at that velocity is possible. The ability for cementite to branch efficiently and produce small spacings is dramatically illustrated by the sudden decrease in spacing occurring at the growth front of a slowly transformed sample that has been quenched. Figure 16b shows that the spacing is decreased by a factor of 5 within a few interlamellar spacings of the original growth front. The micrographs in Figure 18 were taken from longitudinal sections of samples which had been transformed at a nominal rate of 5 μm/sec and increased to velocities over 100 μm/sec. The rate change interface and martensitic areas are readily visible. The rate change interface is visible because of the rapid decrease in spacing due to the increased velocity. SEM microscopy at the interface showed that the spacing decreased nearly as rapidly as in Figure 16b. The additional distance that the pearlite was able to grow after the rate increase was several orders of magnitude greater than the 600 Å spacing characteristic of the high velocities. Therefore, the growth front is able to respond effectively to the transient velocity change but the formation of martensite is sufficient proof that the kinetics of pearlite formation will not support growth at high velocities.

The additional distance that pearlite was able to grow until martensite formed after the rate increase is listed in

Fig. 18. Light micrographs of representative cross sections of samples having undergone an increase in transformation rate. Arrows indicate rate change interfaces, M indicates martensitic areas. a) Rate increased from ~6 to 210 μm/sec (Note prior austenite grain boundaries diagonal to rate change interface) 50X. b) Rate increased from ~4 to 148 μm/sec; 75X. Etch: 1.5% HNO_3 in amyl alcohol and 4% Picral mixed 95:5


M

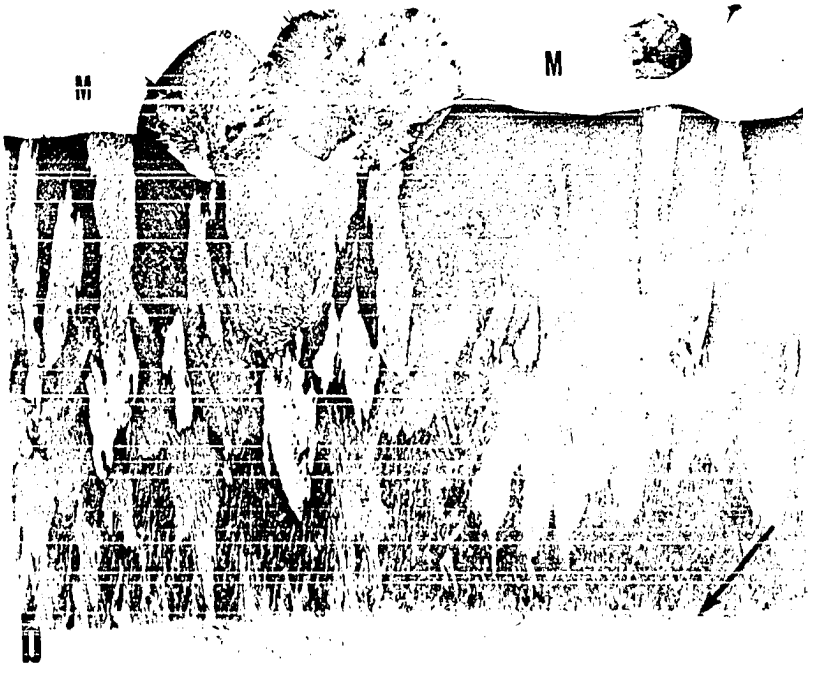
M
M

Table 4 for various starting rates and increased velocities. The reciprocal of the distance should go to zero for increased velocities near the maximum steady-state growth velocity of pearlite. Figure 19 is a plot of the reciprocal distances in Table 4 as a function of velocity. The plotted data do not lie on a straight line and extrapolation to 1/d = 0 is difficult. A curved line through the data yields an extrapolated value for the maximum growth velocity of approximately 100 μm/sec. It is not surprising that the dependence of the reciprocal distance on velocity is not linear because the velocity, which is temperature dependent, is also dependent on the position of the interface in the temperature gradient. Because the temperature gradient changes with the change in velocity, it is difficult to derive an analytic expression for the dependence of 1/d on velocity. Therefore, the determination of the maximum growth velocity by exprapolation of the plot in Figure 19 to 1/d = 0 can only be approximate.

Table 4. Summary of results of the maximum velocity determinations

Initial velocity μm/sec	Increased velocity μm/sec	Distance to martensite mm	Reciprocal distance mm^{-1}
4.4	106	2.4 ± .4	.41 ± .07
5.2	123	1.2 ± .06	.85 ± .05
4.4	148	0.9 ± .06	1.1 ± .08
6.8	163	.69 ± .003	1.5 ± .06
4.4	210	.06 ± .01	1.7 ± .23

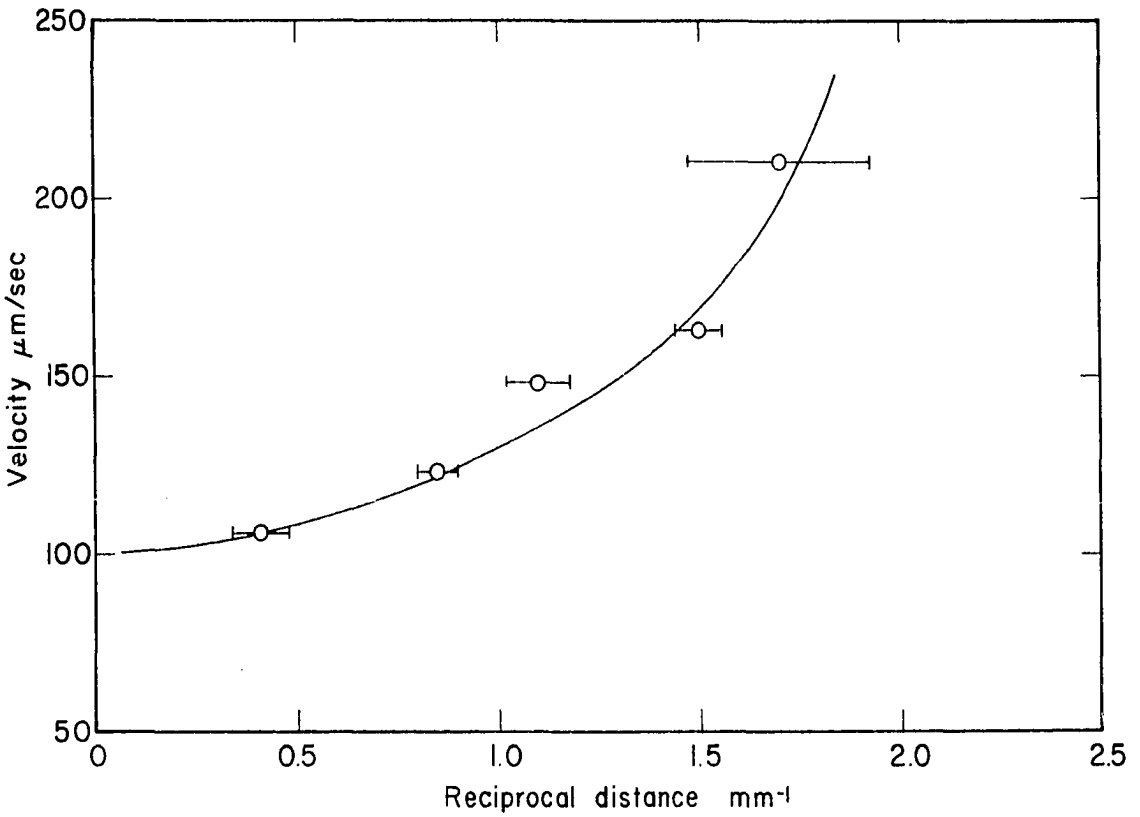

Figure 19. Plot of increased velocities and reciprocal distances from Table 4

The phenomenon of martensite formation in samples transformed at rates over 100 μm/sec is critically dependent on the austenite grain size. The samples used in the rate increase experiments were held at temperature 2 hours prior to transformation to yield very large grain size. If samples are continuously transformed at rates over 100 μm/sec without long austenitizing treatments, the resulting grain size is small due to the rapid passage of the hot zone through the sample. The small grain austenite has considerable grain boundary area and suppression of the nucleation of pearlite before the

material reaches large undercoolings is difficult even with the large gradients used in this study. The material continually transforms to pearlite due to growth from grain boundaries and the transformation is more aptly described by continuously cooling rather directional transformation. Samples quenched after transforming at 148 μm/sec showed the quench interface to be macroscopically planar but was clearly made of individual pearlite nodules and not continuous growth. Martensite was occasionally observed behind the quench interface in larger grains of austenite from which it is evident that pearlite does not grow with sufficient velocity to consume the grain during gradient cooling.

Comparison of Results to Previous Work

Constant velocity growth

This study has generated pearlite interface temperatures and interlamellar spacing data as a function of imposed velocity in the range of 1 to 100 μm/sec. There are no other constant velocity pearlite interface temperature studies with which to compare the interface temperatures of this study. On the other hand, Bolling and Richman (8), Cheetham and Ridley (40), and Chadwick and Edmonds (39) have measured the minimum regularly occurring interlamellar spacing as a function of velocity. Of the two sets of spacing data of this study, the one corresponding to the smallest 20 spacing measurements for each rate, S_{min}, was selected as the most representative

spacing to compare with these other investigations. The results of all the studies are plotted together as log V vs. log S in the velocity range 1 to 100 μm/sec in Figure 20. The results compare favorably and there is a definite trend in the data to lie along a line with slope equal to -2.

Figure 21 is an extended log-log plot containing the results of Bolling and Richman and of Chadwick and Edmonds including velocities under 1 μm/sec and over 100 μm/sec. Both of these data sets show a marked tendency towards smaller spacings at velocities below 1 μm/sec than the extrapolated results of this study would predict. However, as discussed in the pearlite interface temperature results of this chapter, it is difficult to transform a specimen at steady state with velocities below 1 μm/sec. Instabilities in either the heating of the sample or the translation mechanism can lead to temperature variation at the pearlite interface. Both of these investigations used similar water cooled heat sinks employing o-ring seals and both used rf induction heating. The tendency for o-rings to stick at low velocities can cause fluctuations in both the velocity of the sample by temporarily halting motion and the shape of the gradient by altering the point of application of cooling water to the sample. Also all studies heated the sample via rf heating without any feedback control on the power. Therefore, there is probably some temperature fluctuation in the sample caused by power variations. Gross fluctuations in either the drive mechanism or

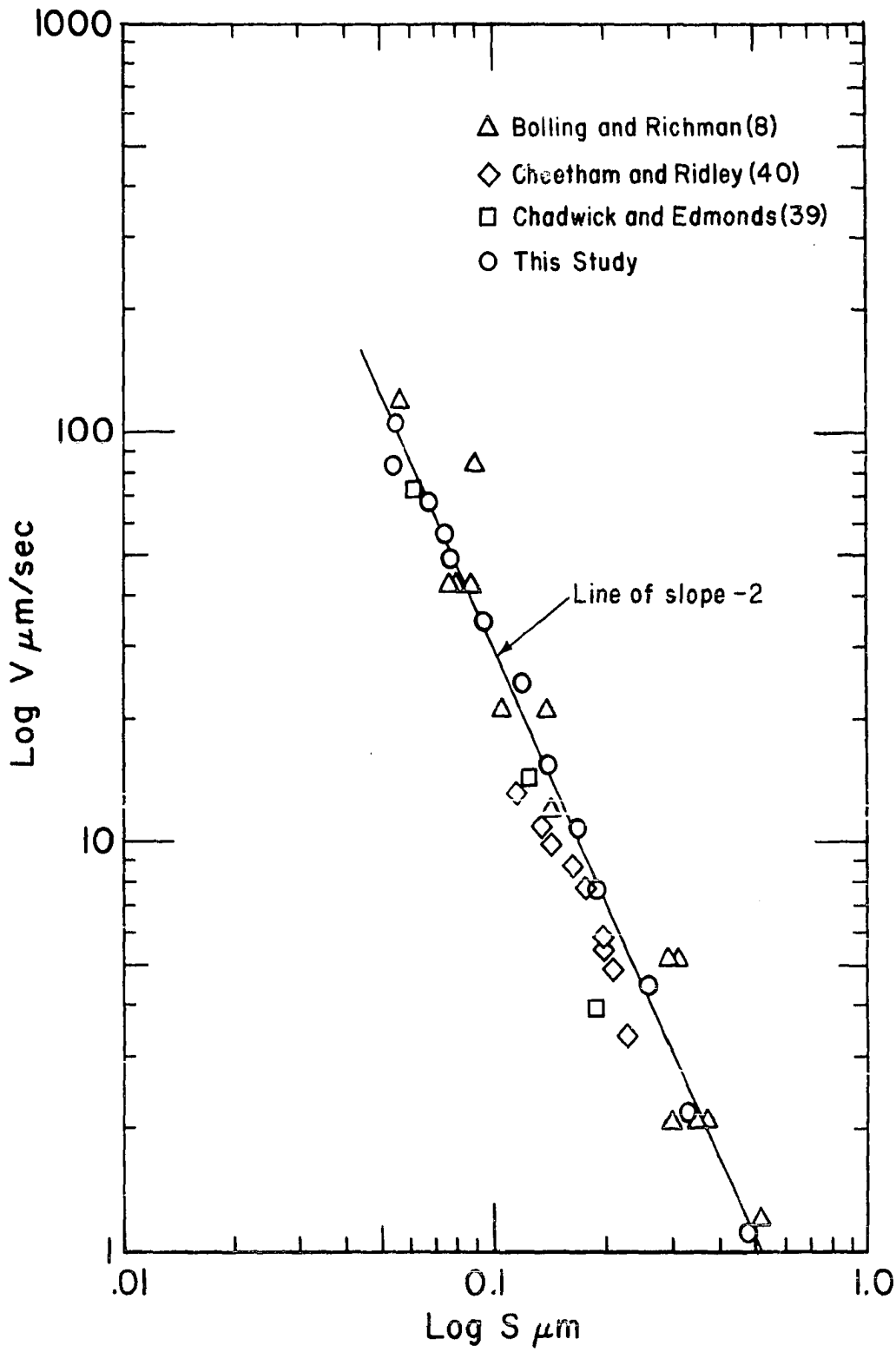

Fig. 20. Comparison of minimum observed spacings as a function of velocity with other constant velocity investigations

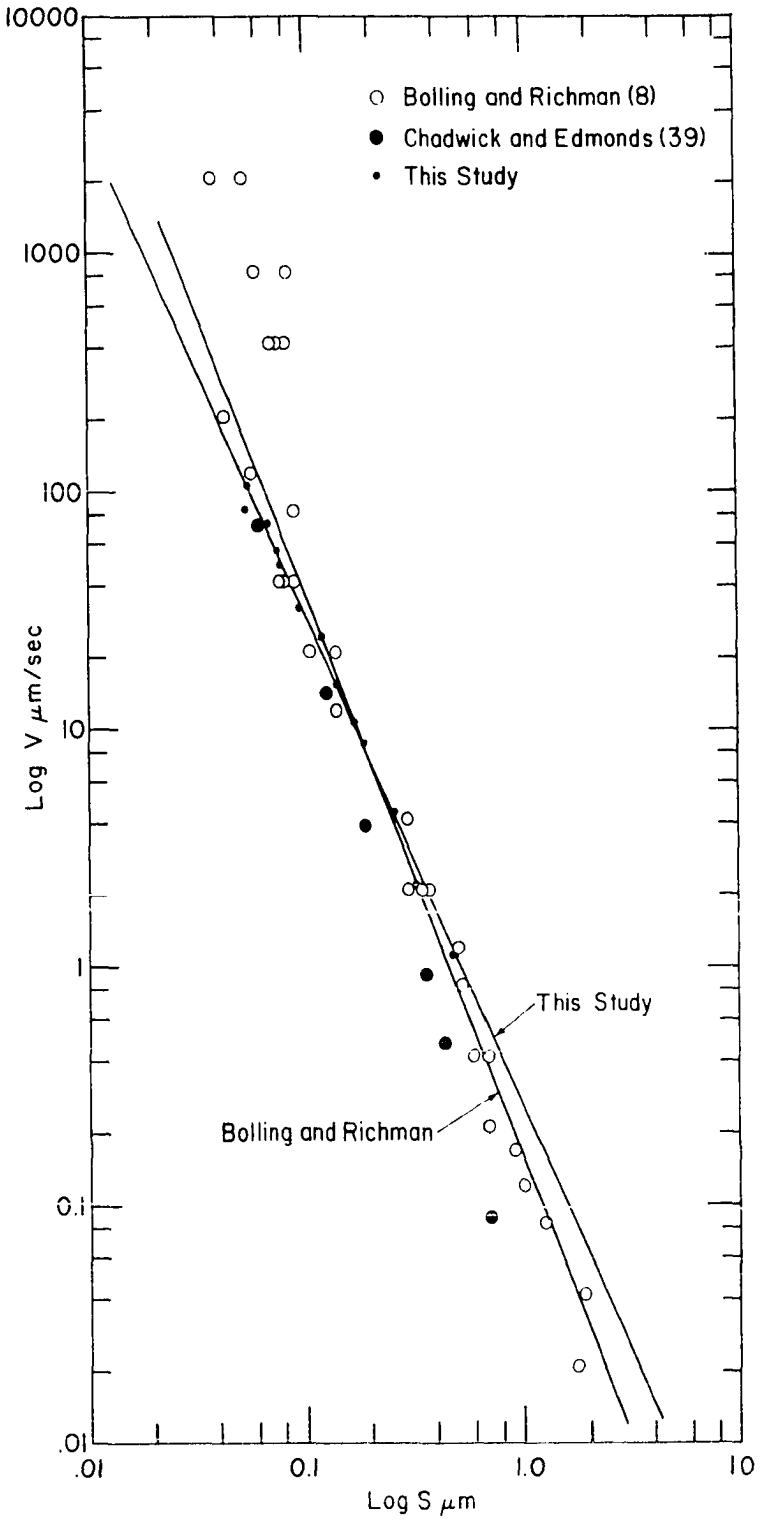

Fig. 21. Comparison of minimum observed spacings as a function of velocity with other constant velocity investigations

power supply will lead to bands in the microstructure. Bands are a common occurrence in directionally solidified eutectics at these rates even when steps are taken to accurately control the heating. The net effect on the fluctuations is to cause the isotherms at the pearlite interface to oscillate. The interface will attempt to move with the isotherms. When the average isotherm moves ahead of the interface, the velocity of the interface will increase producing smaller spacings. On the other hand, when the average isotherm moves behind the interface, the interface stalls and the spacing increases. Figures 5 and 6 from the work of Bolling and Richman (8, p. 2099) show that the spacing adjusts more rapidly to an increase in growth rate than to a decrease in growth rate. It is apparently easier for the spacing to increase by branching of the cementite platelets than to decrease the spacing by overgrowth of the cementite by ferrite. Therefore, the spacing may be smaller for a given average velocity because the velocity of the interface is oscillating. When the velocity increases the spacing is reduced compared to the slower average velocity, however when the velocity decreases, the spacing is not able to adjust as quickly and no appreciable growth occurs until the next increase in velocity occurs due to the oscillating temperature. The growth is actually stepwise with an actual velocity higher than the average translation velocity. Therefore, this would cause a decrease in the spacing for a given average velocity and would explain the smaller

spacings observed by Bolling and Richman and by Cheetham and Ridley than the extrapolated results of this study would indicate.

Isothermal growth

The pearlite interface temperature data as a function of velocity from this study are compared with the isothermal velocities reported by Frye et al. (13) and Brown and Ridley (14) in the plot shown in Figure 22. The results of this study compare well with the isothermally determined velocities for undercoolings to 45°C. At larger undercoolings, the results of the three studies deviate. Brown and Ridley determined velocities by two techniques: one involving a statistical analysis of the size distribution of pearlite nodules with time, and one involving the determination of the largest nodule at each increment of time at temperature. The velocities yielded by these two techniques begin to differ at undercoolings greater than 45°C. The results of this study lie between these two velocity determinations. The measured velocities of Frye et al. obtained by the maximum nodule technique compare very well with the maximum nodule velocities of Brown and Ridley. In addition, Frye et al. showed the maximum velocity of pearlite occurred isothermally at undercoolings of about 130-140°C which is in good agreement to the 126°C interface temperature of the maximum growth rate of 106 μm/sec determined in this study.

The deviation of the isothermal velocities from this

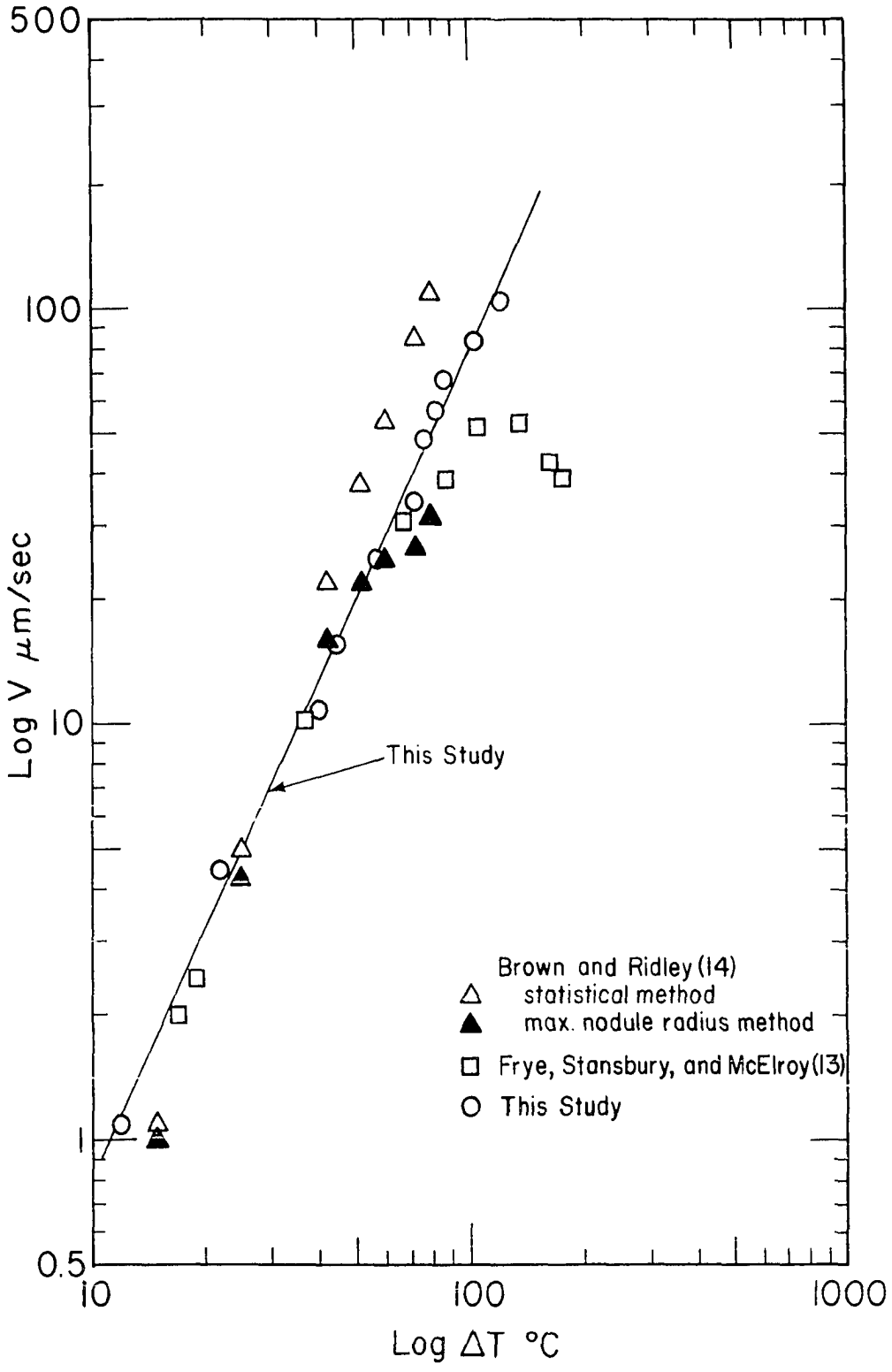

Fig. 22. Comparison of interface undercooling as a function of velocity with other isothermal investigations

study at undercoolings greater than 50°C is not unexpected. It is difficult to measure velocities by interrupting the isothermal pearlite transformation at undercoolings greater than 70°C since the entire sample reacts in less than 5 sec. The experimental difficulties associated with the rapid heat transfer to insure isothermal conditions during pearlite growth, coupled with the need to quench the sample after only a few seconds at temperature, makes it very arduous to get reliable velocity data at large undercoolings.

The chief advantage of isothermal experiments is the accurate determination of spacing as a function of undercooling. Figure 23 is a plot of the log S vs log ΔT for the isothermal spacings determined by Brown and Ridley (14), Cheetham and Ridley (40), and Williams and Glover as cited by Bolling and Richman (8). The interface temperatures and spacing data of this study are also included in the plot for comparison. The results agree well with Brown and Ridley and with Cheetham and Ridley. The overall trend in the data to lie along a line of slope -1 is evident.

It is evident in comparing Figures 22 and 23 that the kinetics of pearlite growth is the same whether pearlite is formed isothermally or at constant velocity. Figure 23 indicates that the spacing is strictly a function of undercooling, a result predicted by Equation 18. Figure 22 shows that interface temperature of pearlite transformed at fixed veloc-

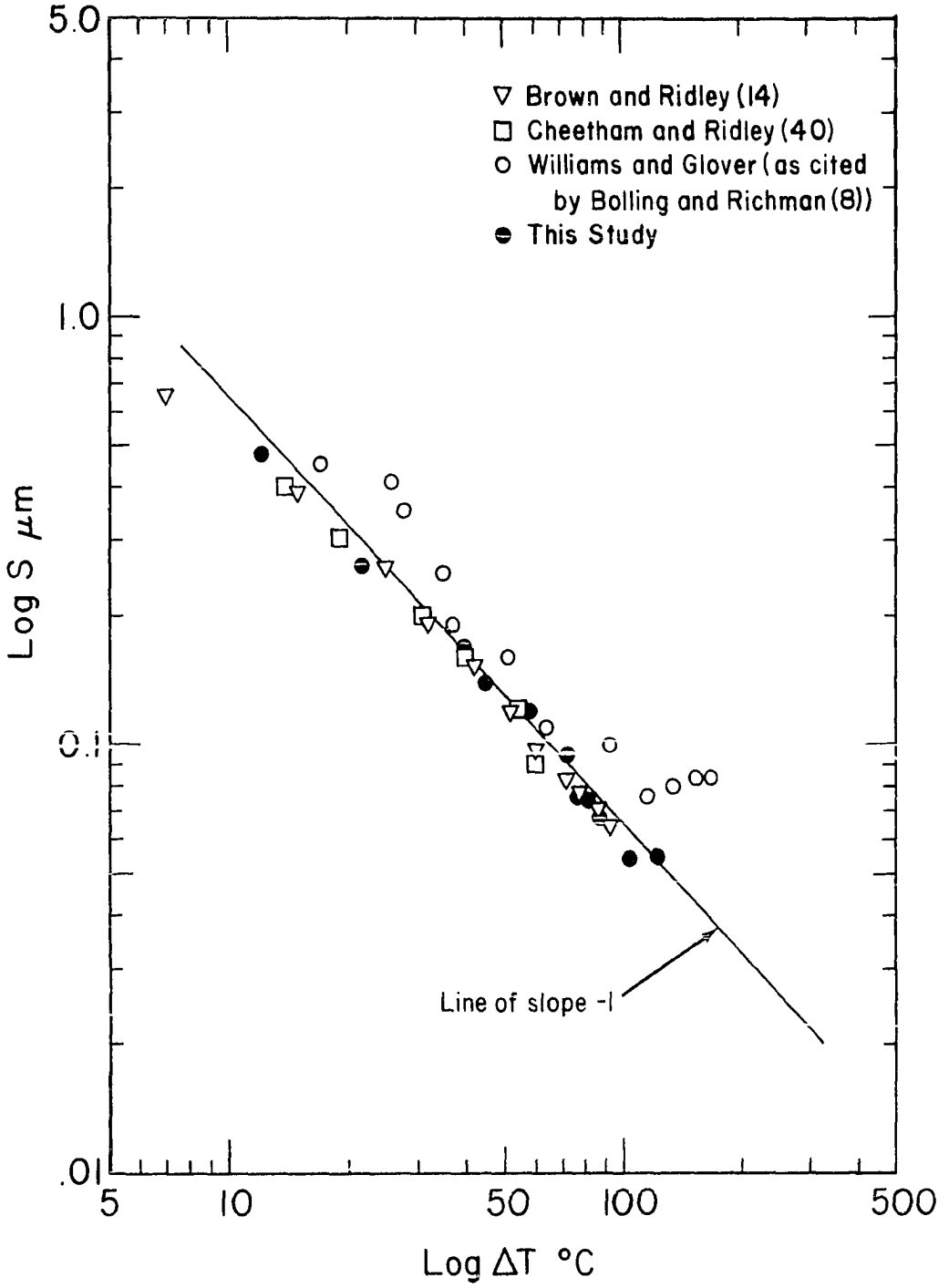

Fig. 23. Comparison of minimum observed spacing as a function of interface undercooling with other isothermal investigations

ity in a gradient corresponds within experimental error to the same velocities observed for isothermal pearlite growth. In previous forced velocity experiments (8,39,40), the temperature of the interface in the gradient could only be obtained by assuming the two growth modes were identical. The results of the interface temperature measurements of this study indicate that this assumption is valid.

Comparison to Theory

The theoretical growth rate expressions (Equations 20 and 26) and the expression for the dependency of the interlamellar spacing on undercooling (Equation 18) are all functions of the form $y = ax^n$. The experimental data from Table 2 were fit to this exponential form through least squares analysis with the resulting equations listed in Table 5. In previous sections, the data and the resulting fitted equations were compared to other experimental investigations. In this section the results will be compared with theory. As discussed earlier, the distinction between volume diffusion and interface diffusion controlled growth can in principle be made by the exponent of the growth rate equations. The exponents for the velocity equations in Table 5 are nearly equal to 2 and thus appear to support volume diffusion. The following discussion critically compares the experimental results with theory for growth controlled by volume diffusion.

Table 5. Least squares fit of the data in Table 2 to the form $y = ax^n$

Dependent variable Y	Independent variable x	Pre-exponential term, a [95% C.I.]	Exponent n [95% C.I.]	Correlation coefficient r
V	ΔT	$8.7(10^{-3})^a$ [5.1-13.2(10^{-3})]	1.99 [1.87-2.11]	.997
V	S_{avg}	.346[b] [.264-.453]	-2.11 [1.97-2.25]	.995
V	S_{min}	.256[b] [.205-.320]	-2.07 [1.97-2.17]	.997
S_{avg}	ΔT	6.38[c] [4.57-8.90]	-.96 [-.88-1.04]	.993
S_{min}	ΔT	5.58[c] [3.96-7.86]	-.97 [.89-1.05]	.993

[a] $\mu m/°C^n$ sec.

[b] $\mu m/\mu m^n$ sec.

[c] $\mu m/°C^n$.

Dependency of spacing on undercooling

The spacing and undercooling data from Table 2 are plotted as log S vs. log ΔT in Figure 24 together with the least squares equations from Table 5. The spacing is very nearly inversely proportional to the undercooling which is in agreement with the equation

$$S_{opt} = KS_c = \frac{2K\sigma^{\alpha C_m} T_E}{\Delta H_V^T \Delta T} \qquad (42)$$

developed on page 12. The constant K, which determines the optimum spacing, depends on whether growth is controlled by volume or interface diffusion and on which optimization principle is invoked. K is 2 for growth at maximum velocity (M.V.) and is 3 for growth at maximum entropy production (M.E.P.) for isothermal growth controlled by volume diffusion. For isovelocity growth in a gradient, the principle of maximum velocity corresponds to minimum interfacial undercooling. Kirkaldy (30, p. 360) has presented arguments that the principles of minimum undercooling and maximum entropy production are the same for isovelocity growth in a gradient.

In principle, the experimental dependence of spacing on undercooling can be compared with Equation 42 to determine the correct optimization principle. However, as discussed previously, the interfacial energy $\sigma^{\alpha C_m}$ is not precisely known and arguments as to which principle is correct will be subject to debate. Estimates of $\sigma^{\alpha C_m}$ can be obtained from the

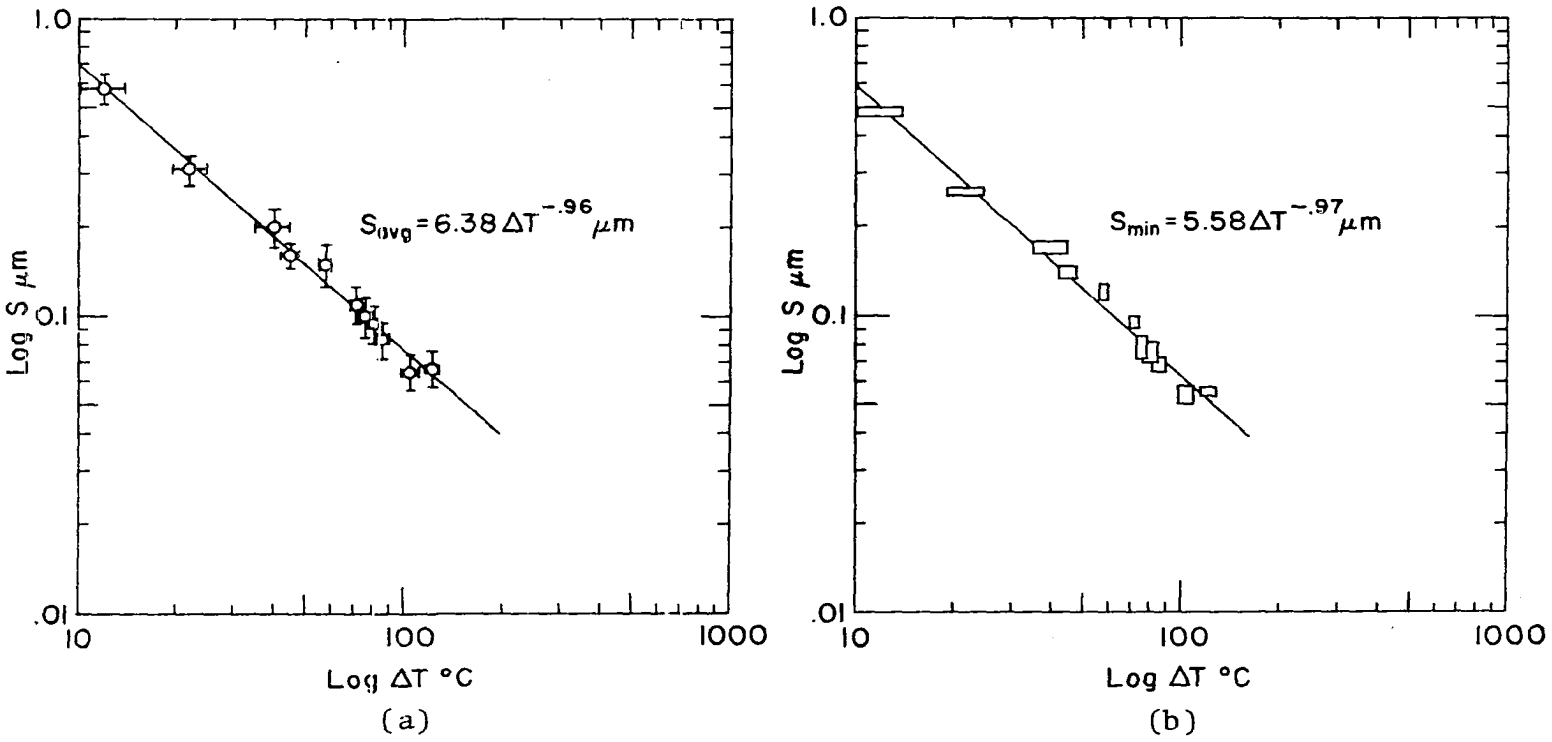

Fig. 24. Logarithmic spacing vs interface undercooling. a) Average spacing. b) Minimum spacing

relative interfacial energies of Smith (43) and absolute austenite grain boundary energies determined by Van Vlack (44). From these two studies, a value for $\sigma^{\alpha C_m}$ of .71 J/m^2 can be extracted. Kramer et al. (45) determined $\sigma^{\alpha C_m}$ and ΔH_V^T to be .70 $\pm$ .3 J/m^2 and 602 J/cm^3, respectively, using precision heat capacity measurements. Although the two values for $\sigma^{\alpha C_m}$ compare favorably, the variance of the interfacial energy reported by Kramer et al. is large. In addition, the calculation of $\sigma^{\alpha C_m}$ from calorimetric data depends critically on the interfacial area per unit volume of the test sample. The difficulty of determining this quantity, which depends on the interlamellar spacing, can readily be appreciated by the debate in the literature as to how the true interlamellar spacing is to be determined (14,25).

Values for $\sigma^{\alpha C_m}$ were calculated from Equation 42 using the experimentally determined relations, $S_{avg}=6.38\Delta T^{-.96}$ μm and $S_{min}=5.58\Delta T^{-.97}$ μm(Table 5), and $\Delta H_T^V=602$ J/cm^3 from Kramer et al. In calculating $\sigma^{\alpha C_m}$, the deviation of the exponents from the ideal value of -1 was ignored. The results are listed in Table 6 for the two optimization principles. The range in

Table 6. Values for $\sigma^{\alpha C_m}$ based on experimental spacings

$S\Delta T$ μm°C	$\sigma^{\alpha C_m}(J/m^2)$ [M.V., $S_{opt} = 2S_c$]	$\sigma^{\alpha C_m}(J/m^2)$ [M.E.P., $S_{opt} = 3\ S_c$]
5.58	.84	.56
6.38	.96	.64

calculated values for $\sigma^{\alpha C_m}$ are within the range determined by Kramer et al. However, it can be seen that neither optimization principle is supported by the average value of $\sigma^{\alpha C_m}$ = .70 J/m^2 which falls between the two determinations. Jordan and Hunt (46) have shown that the spacing in directionally solidified Pb-Sn eutectics is slightly larger than the spacing predicted by growth occurring at minimum undercooling. The results of the spacing measurements of this study, based on the best estimate of $\sigma^{\alpha C_m}$, indicates that this may also be occurring in directional eutectoid growth.

Dependency of spacing and undercooling on velocity

The exponential dependence of the spacing and undercooling on velocity in the least squares equations in Table 5 indicate that volume diffusion is rate controlling. However, in order for a clear distinction to be made between the two diffusion models based on the exponent, the temperature and concentration dependence of the carbon diffusivity in austenite, D_C^{γ}, must be determined. The diffusivity is known to be strongly dependent on temperature and carbon concentration. In addition, as is discussed in Appendix D, the carbon concentration in austenite adjacent to the pearlite interface increases with velocity and interface undercooling. Therefore, the functional form of $D_C^{\gamma}(c,T)$ is important in understanding the kinetics of pearlite growth.

Wells et al. (18) measured diffusivities throughout the

stable austenite phase field using standard diffusion couples. Smith (47) determined the carbon concentration dependence of D_C^γ at various temperatures by measuring the steady state flux of carbon through hollow iron cylinders by carburization techniques. The two techniques agree very well and indicate the isothermal diffusivity increases at a faster than linear rate with carbon concentration. However, values for D_C^γ characteristic of pearlite growth conditions can only be estimated by extrapolation from higher temperatures. Siller and McLellan (48) have applied absolute reaction rate theory and solute interaction statistics to derive a sophisticated expression which accurately accounts for the variation of D_C^γ with carbon concentration. However, application of this model is tedious, especially if the variation in D_C^γ for simultaneous changes in temperature and concentration is of interest. Kaufman et al. (49) presented an equation for the extrapolation of the diffusivities of Wells et al. (18) to very low temperatures in order to characterize the growth of bainite. Their equation was based on the following empirical relationship

$$D_C^\gamma(x,T) = D_o\, e^{-kx}\, e^{\frac{-Q(x)}{RT}} \qquad (43)$$

which qualitatively describes the diffusivity data of Wells et al. However, their treatment of Q(x) de-emphasized the increase in D_C^γ due to increased carbon content. A more accurate equation was obtained by fitting the data of Wells et al. to Equation 43 using a multiple linear regression program (50) at

the Iowa State University Computation Center. The resulting equation was

$$D_c(x,T) = .50 \exp(-33.2x)\exp\{\frac{-(1.53-4.1x-27x^2)10^5}{RT}\} \quad (44)$$

where x is the carbon concentration (at. fr.) and R = 8.147 J/°K. Equation 44 was used to generate lines of equidiffusivity which are shown graphically on the Fe-C phase diagram in Figure 25.

Hillert (17) and Jackson and Hunt (51) have shown for lamellar growth controlled by volume diffusion in a system with an asymmetric phase diagram, that the average solute concentration at the growth front depends on the rate of growth and undercooling. The deviation from the eutectoid composition at the growth front occurs because of the difference in concentration ahead of the two lamellae and the difference in their respective volume fractions. Therefore, in the Fe-C system there will be a net increase in carbon content of the interface with undercooling because the volume fraction of ferrite is 88% and the extrapolated $\gamma/\gamma + \alpha$ and $\gamma/\gamma + C_m$ phase boundaries indicate that there is a proportionally greater increase in carbon in front of ferrite than the depletion of carbon in front of cementite (see Figures 1 and 2).

The magnitude of the buildup depends on the slope of the $\gamma/\gamma + \alpha$ and $\gamma/\gamma + C_m$ phase boundaries, the ratio S^{C_m}/S^{α}, and various thermodynamic quantities. The slope of the extrapo-

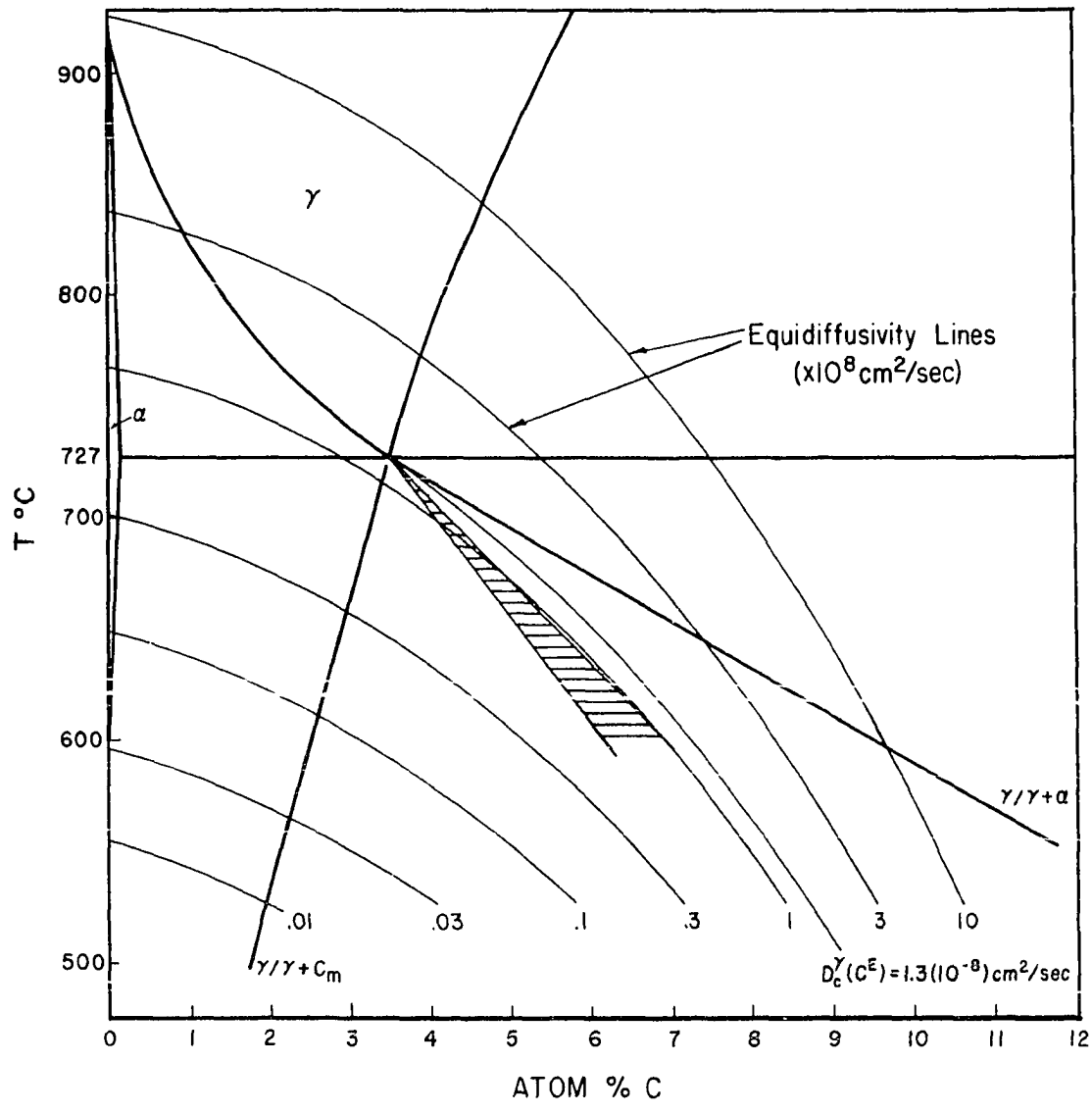

Fig. 25. Lines of equidiffusivity of carbon in austenite superimposed on Fe-C phase diagram. Cross hatched region indicates predicted average pearlite interface concentration of carbon as a function of undercooling

lated $\gamma/\gamma + \alpha$ phase boundary (m_α) has been the object of considerable theoretical investigation (48,52,53) and a reasonable estimate of m_α based on these is 2100°C/at. fr. A value for the slope of extrapolated $\gamma/\gamma + C_m$ phase boundary (m_{C_m}) of 13000°C/at. fr. can be obtained from the Fe-C phase diagram by Chipman (54). These two extrapolations are plotted in Figure 25. The fraction S^α/S was obtained from the relation

$$\frac{S^\alpha}{S} = \frac{f_m^\alpha/\rho^\alpha}{f_m^\alpha/\rho^\alpha + (1-f_m^\alpha)/\rho^{C_m}} = .882 \qquad (45)$$

where $\rho^\alpha = 7.874$ gm/cm^3, $\rho^{C_m} = 7.68$ gm/cm^3 (55) and $f_m^\alpha = .885$ (54). With these determined, the average carbon concentration at the interface was calculated as a function of undercooling (Appendix D) with the result

$$\bar{x}^\gamma = .0349 + (2.42\pm.22)10^{-4}\,\Delta T. \qquad (46)$$

This was plotted in Figure 25 with the equidiffusivity lines previously determined. From this figure it can be seen that the average carbon concentration in the interface is approximately tangent to the equidiffusivity lines. Therefore, it is reasonable to assume D_C^γ is fairly constant and can be estimated as $1.3(10^{-8})$ cm^2/sec.

The velocity equations in Table 5 can be interpreted as supporting volume diffusion with D_C^γ assumed constant. The equation for growth controlled by volume diffusion developed previously (Equation 15) is

$$V = \frac{D_c^{\gamma}}{a} \frac{S^2}{S^{\alpha}S^{C_m}} \frac{C_e^{\gamma/\alpha} - C_e^{\gamma/C_m}}{C^{C_m} - C^{\alpha}} \frac{1}{S}\left(1 - \frac{S_c}{S}\right) \tag{47}$$

where a defines the characteristic diffusion length, δ, (Figure 2) through the relation $\delta = aS$. Zener (10) assumed a = .5 but a more rigorous treatment by Hillert (17) and Jackson and Hunt (51) defines a through the equation

$$a = \frac{1}{\pi^3}\left(\frac{S^2}{S^{\alpha}S^{C_m}}\right)^2 \sum_{1}^{\infty} \frac{1}{n^3} \sin^2\left(\frac{n\pi S^{\alpha}}{S}\right) \tag{48}$$

which yields a = .77 when $S^{\alpha}/S = .882$. The ratio of the concentrations can be calculated from

$$\frac{C_e^{\gamma/\alpha} - C_e^{\gamma/C_m}}{C^{C_m} - C^{\alpha}} = \frac{\frac{V_m^{\alpha}\Delta T}{m_{\alpha}} + \frac{V_m^{C_m}\Delta T}{m_{C_m}}}{x^{C_m} V_m^{C_m}} = 2.61(10^{-3})\Delta T \tag{49}$$

with $x^{C_m} = .25$, $x^{\alpha} \cong 0$, $V_m^{\alpha} = 7.093\ cm^3$, and $V_m^{C_m} = 5.65\ cm^3$ (55). Therefore, Equation 47 becomes

$$V = .021 \frac{D_c^{\gamma}}{a} \frac{\Delta T}{S}\left(1 - \frac{S_c}{S}\right) \tag{50}$$

The ratio $S^c/S = 1/2$ for growth at maximum velocity and is equal to 2/3 for growth at maximum entropy production. S can be eliminated from Equation 50 by substituting the experimentally determined values

$$\frac{1}{S} \cong \frac{\Delta T}{6.38}\ \mu m^{-1} \tag{51}$$

and

$$\frac{1}{S} \cong \frac{\Delta T}{5.58}\ \mu m^{-1} \tag{52}$$

from Table 5. Thus, Equation 50 will become

$$V = 0.21\ k\ \frac{D_c^{\gamma}}{a}\ \Delta T^2\left(1-\frac{S_c}{S}\right) \tag{53}$$

where k is derived from Equation 51 and 52. Values for D_c^{γ}/a can be extracted from Equation 53 by comparison to the experimentally determined equation

$$V \cong 8.17(10^{-3})\Delta T^2 \tag{54}$$

from Table 5. Values for D_c^{γ}/a based on Equations 51, 52, 53, and 54 are tabulated in Table 7.

Table 7. Determination of D_c^{γ} from experimental results

$S\Delta T$ $\mu m°C$	Optimization principle	D_c^{γ}/a $10^{-8}cm^2/sec$	D_c^{γ} a=.5 $10^{-8}cm^2/sec$	D_c^{γ} a=.77 $10^{-8}cm^2/sec$
5.53	M.V.	4.34	2.17	3.34
5.58	M.E.P.	3.26	1.63	2.50
6.38	M.V.	4.96	2.48	3.82
6.38	M.E.P.	3.72	1.86	2.86

The calculated values of D_c^{γ} in Table 7 based on the two estimates of a are about a factor of 2 greater than the extrapolated value of $1.3(10^{-8})$ cm^2/sec for D_c^{γ}. There are several possible explanations for the discrepancy. First, theory may not adequately describe the magnitude of the concentration gradients in which case a is smaller than those listed in Table 7. Although possible, it is difficult to imagine characteristic lengths less than 1/2 the interlamellar spacing.

Second, carbon transport by volume diffusion may be aided in part by interface diffusion. However, if this is true, it would be expected that the contribution would be larger for faster growth rates. However, this is not observed since the quadratic dependence of the undercooling and spacing is preserved up to the maximum observed velocity. The final and most likely possibility is that the diffusivity in austenite adjacent to the pearlite growth front is altered by the conditions existing between the product and parent phases. Pearlite can be envisioned as growing into a matrix of austenite in which carbon is diffusing interstitially. However, from the crystallographic data by Fasiska and Jeffrey (56) there is an approximately 10% increase in the atomic volume of Fe in cementite over ferrite at room temperature. There exists a .8% volume expansion during the formation of pearlite (57) and the differential in the atomic volume of Fe in cementite and ferrite is not likely to change greatly at the temperatures of pearlite formation. Therefore, strain is induced in the austenite during pearlite formation and there must be some sideways plastic flow of the γ matrix iron atoms to ferrite as has also been noted by Hillert (17). Therefore, the extrapolated diffusivities which are based on interstitial diffusion in annealed austenite may be low. The combination of tensile strain in austenite together with the plastic flow of austenite may increase the diffusivity. For example carbon transport to cementite could be aided by pipe diffusion

through dislocations generated in front of cementite.

There are two observations which partially support the hypothesis of stain aided diffusion. First, Rathenau and Baas (58) observed that austenite grain boundaries are displaced towards an advancing pearlite colony. Second, the commonly observed occurrence of cementite platelets being stopped by austenite grain boundaries suggests there is some cooperation between cementite and austenite for increased diffusivities such as through dislocation networks or strain. When a cementite platelet intercepts an austenite grain boundary, the cooperation is lost and growth of cementite is impaired.

Some factors limiting the growth rate of pearlite

In the previous section, arguments have been presented for explaining why D_C^{γ} should be constant for pearlite growth. However, if this is true, there should be no reason for the rate of growth of pearlite to reach a maximum value. Marder and Bramfitt (34) have studied the growth rate of pearlite in continuously cooled high purity eutectoid alloys. An advantage of this technique is that pearlite growth rates can be determined at temperatures below the interface temperature corresponding to the maximum growth rate in directionally transformed pearlite. They have observed that pearlite reaches a maximum growth rate of ~ 80 μm/sec at 585°C and then gradually decreases on further undercooling, until a terminal velocity of 50 μm/sec at 525°C is reached. There are several

possible explanations for this behavior.

It was assumed in the development of the growth equations that the concentration difference in austenite between ferrite and cementite could be obtained by straight line extrapolations of the $\gamma/\gamma+\alpha$ and $\gamma/\gamma+C_m$ phase boundaries. This is a good approximation for undercoolings to 100°C. For larger undercoolings, theoretical models for the extrapolations indicate that there is curvature towards the eutectoid composition (48, 52,53). Therefore, the rate of increase of the concentration difference driving diffusion with increased undercooling is reduced and the rate of growth of pearlite is limited.

The volume expansion which occurs during the formation of pearlite must induce strains in all three phases and there is probably some deformation in austenite due to the redistribution of Fe atoms to ferrite. As the temperature is reduced, the elastic constants of the three phases increase as well as the yield strength of austenite. Hillert (17) has made calculations indicating that the free energy loss due to mechanical deformation is proportionally larger at higher temperatures than at lower temperatures. However, if the enhancement of diffusivity is due to elastic strains and deformation in austenite, then it is likely that relative enhancement over extrapolated diffusivities decreases with temperature due to increases in the elastic constants. Therefore, the growth rate is reduced due to the decrease in diffusivity with temperature at large undercoolings.

It should be noted that at the maximum rate of 100 μm/sec the interlamellar spacing is 600 Å and the width of the cementite platelet is 50 Å. The growth of pearlite must be cooperative in order that both phases take advantage of the efficient portioning of carbon in austenite. However, with small lamellar widths of cementite and high growth rates, the interface between austenite and pearlite may be unstable. Fluctuations of the interface may cause the cementite platelet to be pinched off by ferrite due to the narrow width of cementite at high velocities. Therefore, the ultimate limit of the formation of pearlite at low temperatures may be due to loss of cooperation between the two growing phases because of interface perturbations.

CONCLUSIONS

The following conclusions can be made from the results of this study on the directional growth of high purity Fe-C eutectoid alloys.

1. The growth of pearlite is controlled by diffusion of carbon in austenite ahead of the advancing pearlite growth front. Extrapolated diffusivities of carbon in austenite are about a factor of 2 to 3 smaller than the apparent diffusivity. It is probable that some enhancement in the diffusivity of carbon due to volume strain effects during transformation is occurring.

2. The interface temperature of pearlite transformed at constant velocity in a thermal gradient corresponds to the temperature of isothermally transformed pearlite with the same characteristic velocity. Both techniques produce spacings with the same inverse dependence on undercooling below the eutectoid. Therefore, the growth of pearlite can be assumed to be independent of the method of transformation.

3. The maximum growth rate of forced velocity pearlite is approximately 100 μm/sec occurring at about 130°C below the eutectoid temperature.

4. The spacing of pearlite directionally transformed in a thermal gradient is inversely proportional to the undercooling. The spacing is not adequately described by either of the two optimization principles of minimum undercooling of the inter-

face or maximum entropy production.

5. The volume fraction of regular lamellar pearlite decreases significantly with increasing rate.

6. The directional transformation of pearlite is not as effective in producing lamellae aligned with the growth direction as is the directional solidification of eutectics.

7. The process of passing a zone of austenite through a high purity Fe-C alloy does not produce elongated grains of austenite in the transformation direction as might be expected by analogy to similar work on controlled recrystallization experiments (59).

8. A high percentage of pearlite colonies are adversely affected by austenite grain boundaries which generally disrupt the lamellar character by inhibiting the growth of cementite.

LITERATURE CITED

1. H. C. Sorby, J. Iron Steel Inst. (London), No. 1, 140 (1896).

2. J. D. Embury and R. M. Fisher, Acta Met., 14, 147 (1966).

3. F. C. Hull and R. F. Mehl, Trans. ASM, 30, 381. (1942).

4. R. F. Mehl and W. C. Hagel, in "Progress in Metal Physics," Vol. 6, B. Chalmers and R. King, Eds., Pergamon Press, New York, New York, 1956, p. 74.

5. J. W. Cahn and W. C. Hagel, in "Decomposition of Austenite by Diffusional Processes," V. F. Zackay and H. I. Aaronson, Eds., Interscience Publishers, New York, 1962, p. 131.

6. M. P. Puls and J. S. Kirkaldy, Met. Trans., 3, 2777 (1972).

7. M. Hillert, in "Chemical Metallurgy of Iron and Steel," Proc. Int. Symp. on Metallurgical Chemistry-Applications of Ferrous Metallurgy, Sheffield, 1971, Iron and Steel Inst., London, 1973, p. 241.

8. G. F. Bolling and R. H. Richman, Met. Trans., 1, 2095 (1970).

9. F. M. A. Carpay, Met. Trans., 5, 2614 (1974).

10. C. Zener, Trans. Met. Soc. AIME, 167, 550 (1946).

11. M. Hillert, Met. Trans., 3, 2729 (1972).

12. A. Hultgren, in "Hardenability of Alloy Steels," American Society for Metals, Cleveland, 1938, p. 55.

13. J. H. Frye, Jr., E. E. Stansbury, and D. L. McElroy, Trans. AIME, 197, 219 (1953).

14. D. Brown and N. Ridley, J. Iron Steel Inst. (London), 207, 1232 (1969).

15. W. H. Brandt, J. Appl. Phys., 16, 139 (1945).

16. E. Schiel, Z. Metallk., 37, 123 (1946).

17. M. Hillert, Jernkont. Ann., 141, 757 (1957).

18. C. Wells, W. Batz, and R. F. Mehl, Trans. AIME, 188, 553 (1950).

19. M. Hillert, in "The Mechanism of Phase Transformations in Crystalline Solids," Institute of Metals Monograph and Report Series No. 33, The Institute of Metals, London, 1969, p. 231.

20. G. Bolze, M. P. Puls, and J. S. Kirkaldy, Acta Met., 20, 73 (1972).

21. M. S. Sulonen, Acta Met., 12, 749 (1964).

22. D. Turnbull, Acta Met., 3, 55 (1955).

23. F. M. A. Carpay, Acta Met., 18, 747 (1970).

24. F. M. A. Carpay and J. Van den Boomgaard, Acta Met., 19, 1279 (1971).

25. G. E. Pellisier, M. F. Hawks, W. A. Johnson, and R. F. Mehl, Trans. ASM, 29, 1049 (1942).

26. J. W. Cahn, Acta Met., 7, 18 (1959).

27. J. M. Shapiro and J. S. Kirkaldy, Acta Met., 16, 579 (1968).

28. B. E. Sundquist, Acta Met., 16, 1413 (1968).

29. B. E. Sundquist, Acta Met., 17, 967 (1969).

30. J. S. Kirkaldy, in "Energetics in Metallurgical Processes IV," W. M. Mueller, Ed., Gordon and Breach Science Publishers, New York, 1968, p. 197.

31. J. S. Kirkaldy, Scripta Met., 2, 565 (1968).

32. B. Chalmers, "Principles of Solidification," John Wiley and Sons, New York, 1964, p. 201.

33. D. Cheetham and F. R. Sale, Acta Met., 23, 1479 (1975).

34. A. R. Marder and B. L. Bramfitt, Met. Trans., 6A, 2009 (1975).

35. E. Schiel and A. Lange-Weise, Arch. Eisenhüttenw., 11, 93 (1937).

36. S. Glasstone, K. J. Laidler and H. Eyring, "The Theory of Rate Processes, McGraw-Hill, New York, 1941, p. 400.

37. B. L. Bramfitt and A. R. Marder, Proc. Ann. Tech. Meet. Int. Metall. Soc., 43 (1968).

38. R. W. Kraft, J. Metals, 18, 192 (1966).

39. G. A. Chadwick and D. V. Edmonds, in "Chemical Metallurgy of Iron and Steel," Proc. Int. Symp. on Metallurgical Chemistry - Applications in Ferrous Metallurgy, Sheffield, 1971, Iron and Steel Inst., London, 1973, p. 264.

40. C. Cheetham and N. Ridley, J. Iron Steel Inst. (London), 211, 648 (1973).

41. C. W. Marschall, J. D. Myers, and G. W. P. Rengstorff, Met. Eng. Quart., 14, 19 (1974).

42. R. W. Powell and M. J. Hickman, J. Iron Steel Inst. (London) 154, 112 (1946).

43. C. S. Smith, Trans. Met. Soc. AIME, 185, 762 (1949).

44. L. H. Van Vlack, Trans. Met. Soc. AIME, 191, 251 (1951).

45. J. J. Kramer, G. M. Pound, and R. F. Mehl, Acta Met., 6, 763 (1958).

46. R. M. Jordan and J. D. Hunt, Met. Trans., 3, 1385 (1972).

47. R. P. Smith, Acta Met., 1, 578 (1953).

48. R. H. Siller and R. B. McLellan, Met. Trans., 1, 985 (1970).

49. L. Kaufman, S. V. Radcliffe, and M. Cohen, in "Decomposition of Austenite by Diffusional Processes," V. F. Zackey and H. I. Aaronson, Eds., Interscience Publishers, New York, 1962, p. 313.

50. B. L. Hanson, "Mouflon: Statistical Numerical Analysis and Data Processing, No. 12," Statistical Laboratory, Iowa State University, Ames, Iowa, 1969.

51. K. A. Jackson and J. D. Hunt, Trans. Met. Soc. AIME, 236, 1129 (1966).

52. H. I. Aaronson, H. A. Domian, and G. M. Pound, Trans. Met. Soc. AIME, 236, 753 (1966).

53. H. Harvig, Jerkont. Ann., 155, 157 (1971).

54. J. Chipman, in "Metals Handbook: Metallography, Structures and Phase Diagrams," vol. 8, American Society for Metals, Metals Park, Ohio, 1973, p. 275.

55. F. X. Kayser, A. Litwinchuk, and G. L. Stowe, Met. Trans., 6A, 55 (1975).

56. E. J. Fasiska and G. A. Jeffrey, Acta Cryst., 19, 463 (1965).

57. H. Stuart and N. Ridley, J. Iron Steel Inst. (London), 204, 711 (1966).

58. G. W. Rathenau and G. Baas, Acta Met., 2, 875 (1954).

59. R. L. Cairns, L. R. Curwick, and J. S. Benjamin, Met. Trans., 6A, 179 (1975).

ACKNOWLEDGEMENTS

I wish to thank those who have made my graduate career pleasant and most rewarding. First, my major professor, Dr. John D. Verhoeven, whose encouragement and stimulation of my interest in research has made this project a reality. To Mr. E. D. Gibson whose suggestions and instruction of experimental technique were of considerable value and Mr. D. D. Woods whose machine work of the experimental equipment was most excellent, I extend my warmest thanks. Finally, to my wife Chris without whose patience and support, my graduate goals might not have been achieved, I express my gratitude.

I am also indebted to Dr. C. A. Beiser of the AISI Product Properties Subcommittee and Battelle Memorial Laboratories for furnishing the high purity iron used in this investigation.

APPENDIX A. ADJUSTING THE LEVEL OF HEATING WITH THE WESTINGHOUSE RADIOFREQUENCY GENERATOR

The basic tank circuit of the Westinghouse 25 kW Dual Frequency Radiofrequency Generator is schematically diagrammed in Figure A-1. The tank coil, excitation coil, and work coil together with the two tank capacitors define a simple LC oscillator circuit. The unit is designed to operate between 300 and 500 kHz. The frequency of an LC circuit is $2\pi/\sqrt{LC}$. Therefore, since the capacitance of the tank circuit is fixed, the frequency is adjusted by removing or adding turns in the tank soil and by the size of the work coil. The capacitance of the circuit is large and is designed to drive small single turn work coils used extensively in industry for surface hardening

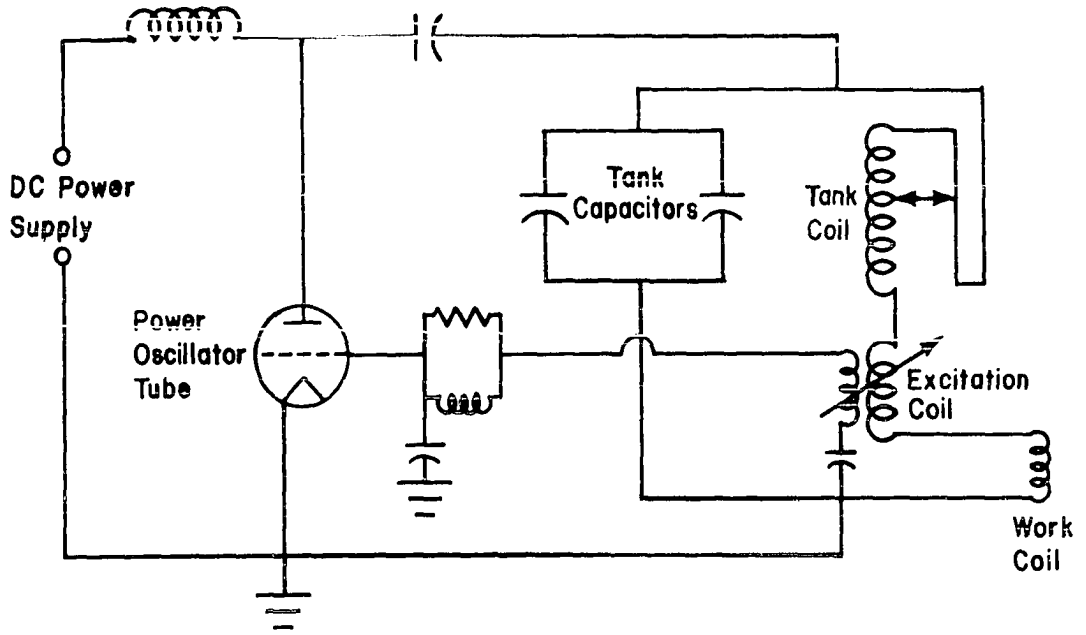

Figure A-1. Basic circuit of the Westinghouse Radiofrequency Generator

shafts and spindles. As such, the unit is ideally suited for heating a small zone necessary for the generation of high gradients required for this study. Power output of the rf generator is controlled by regulating the dc voltage over the oscillator circuit. The unit is equipped with a saturable core reactor which can control the voltage level quite satisfactorily. However, maximum efficiency results when full voltage is applied. Therefore, good matching between the load which is comprised of the oscillator circuit and the dc power supply is desirable for optimum heating conditions.

In any power circuit which has an internal resistance in the power supply, optimum power output is achieved when the resistance of the load is equal to the internal resistance of the power supply. In the case of induction heating, the various resistances are not known and the desired level of heating must be obtained largely by trial and error. Areas of control can be separated into three groups. The impressed (plate) voltage, the work coil, and the geometry of the work piece.

The plate voltage could be controlled in two ways. First, by use of the saturable core reactor already described. This could set the voltage level up to the maximum output voltage of the step-up transformer used to convert the line voltage to the operating voltage. In addition to the saturable core reactor voltage control, the step-up transformer could be adjusted to set three different plate voltage levels. These were 4600,

6500, and 9300 dc volts. The 6500 dc volt level was used throughout this study and supplied more than adequate power.

The work coil and geometry of the work piece are intimately related and will be discussed together. Since it was necessary to protect the sample against decarburization by surrounding it with a Pyrex tube which could hold an inert atmosphere, the inside diameter of the work coil was limited by the diameter of the Pyrex tube. Coupling between a given work coil and the work piece is primarily a function of the ratio of the cross sectional area of the work piece to that of the area of the inside diameter of the work coil. Fortunately, since this ratio was fixed by the particular geometry of the system, there was still adequate power to obtain the desired heating. The number of turns in the work coil was determined by trial and error. Four turns appeared to be the optimum, a fifth turn was tried but did not have any additional heating effect largely because it was too far from the center of the coil to add effectively to the flux density. Final adjustment of the system was achieved in two ways. First, assuming maximum voltage is applied to the LC circuit, the voltage drop over the circuit is divided over the tank coil, excitation coil and the work coil. The excitation coil is actually part of the tank coil and is part of the feed back circuit that controls the current drawn from the power oscillator tube. Adjusting the tank coil had two effects: altering the frequency

and changing the relative voltage drop over the work coil. By adding or subtracting turns in the tank coil, as much as 50-100°C difference would result in the maximum temperature of the sample. Subtracting turns increased the frequency, but more importantly, increased the voltage over the work coil thus increasing the power input to the sample. The second method of fine adjusting the level of heating in the sample was changing the separation distance between the two cooling fixtures by using different Pyrex tubes. The longer tubes increased both the effective heating area and the distance from the center of the hot zone that cooling water was in contact with the sample.

In summary, the level of heating could only be determined empirically. Nearly thirty coils and four different cooling fixtures were tried until the system described was obtained. The most effective control over heating with maximum applied voltage was adjustment of the tank coil and separation between the cooling fixtures. The maximum gradient ever obtained, which was the quantity to be optimized, was 2400°C/cm with a sample translation rate of 200 μm/sec. However, for the majority of samples a gradient of 1800-2000°C/cm was typical.

APPENDIX B. DISCUSSION OF POSSIBLE ERROR IN MEASURING THE AUSTENITE TO PEARLITE INTERFACE TEMPERATURE IN A THERMAL GRADIENT USING A THERMOCOUPLE OF FINITE SIZE

This appendix is concerned with possible sources of error in using a thermocouple to measure the isotherm characteristic of the austenite to pearlite transformation interface forced to move at a constant rate in a temperature gradient. Error can occur because the bead has small but finite size and the large gradients used in this study produce a significant temperature variation within the bead. As a result, the output of the thermocouple is not unique to a single isotherm and, therefore, calibration of the thermocouple was not based on an isothermal standard but more appropriately, on the gradient change characteristic of the austenitizing interface. No appreciable superheat was observed so that the eutectoid temperature was selected as the most reliable reference for calibration of the thermocouple. The following discussion is divided into two parts. The first is concerned with temperature gradients within the bead, and the second with a justification for using the austenitizing interface as a standard reference.

The geometry of the thermocouple with respect to the sample is diagramed in Figure B-1. The hole undoubtedly influences the thermal gradient in the sample in the vicinity of the bottom of the hole. However, the disruption in the total

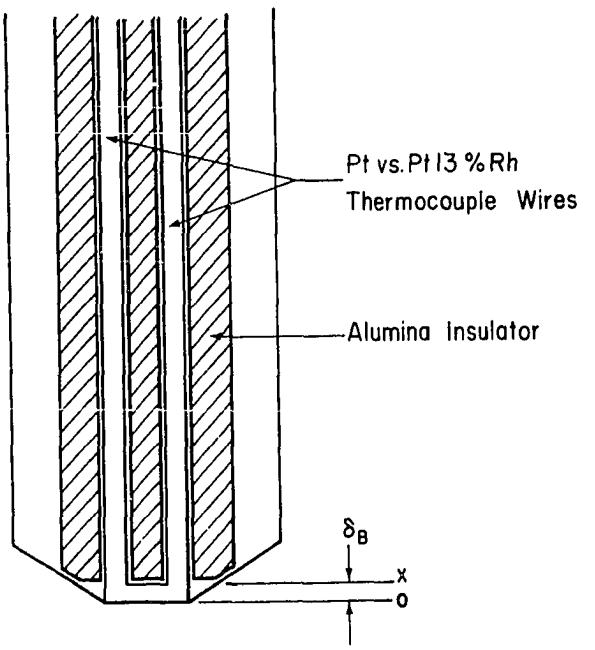

Fig. B-1. Geometry of the thermocouple and sample

heat flow of the sample will be small since the cross sectional area is only 6.3% of the total cross sectional area of the sample. Further, since the thermal conductivity of the material is high, the heat flux will be sufficiently large to effectively smooth radial variation in the thermal gradient thus minimizing distortion of the isotherms near the thermocouple bead. Therefore, when the sample is moving at constant rate in a temperature gradient, the thermocouple will pass through the austenite to pearlite transformation interface, which is occurring at some characteristic isothermal plane, without significantly disrupting the steady-state behavior of the reaction.

However, the possibility that an error can occur in the measurement of the temperature of the point of gradient change results from the fact that the surface of the bead in contact with the sample may not be the source of emf responsible for the output of the thermocouple. An approximation of the error can be made by assuming the bead to be uniformly alloyed, and that the thermocouple leads contact the bead at plane x in Figure B-1 with a step change in concentration between the leads and the bead at this plane. The recorded output of the bead, T_R, will then be determined by the temperature of plane x and will be different from the temperature of the tip of the sample, T_T, at $x+\delta$. This difference, ΔT, is given by

$$\Delta T = T_R - T_T = G_B \delta_B \qquad \text{(B-1)}$$

where G_B is the gradient in the bead, and δ_B is the bead thickness.

Since it is the temperature of the sample that is of primary interest, the temperature increment defined by Equation B-1 may lead to error in the measured point of gradient change if the gradient in the bead differs significantly from the gradient in the sample. Figure B-2 shows the effect of the recorded gradient being displaced by temperature increments ΔT_γ and ΔT_p from the actual temperature gradient which would be recorded by an infinitesimal thermocouple at plane $x+\delta$. The temperature increments obtained from Equation B-1 are

$$\Delta T_\gamma = G_B^\gamma \delta_B \qquad \text{(B-2)}$$

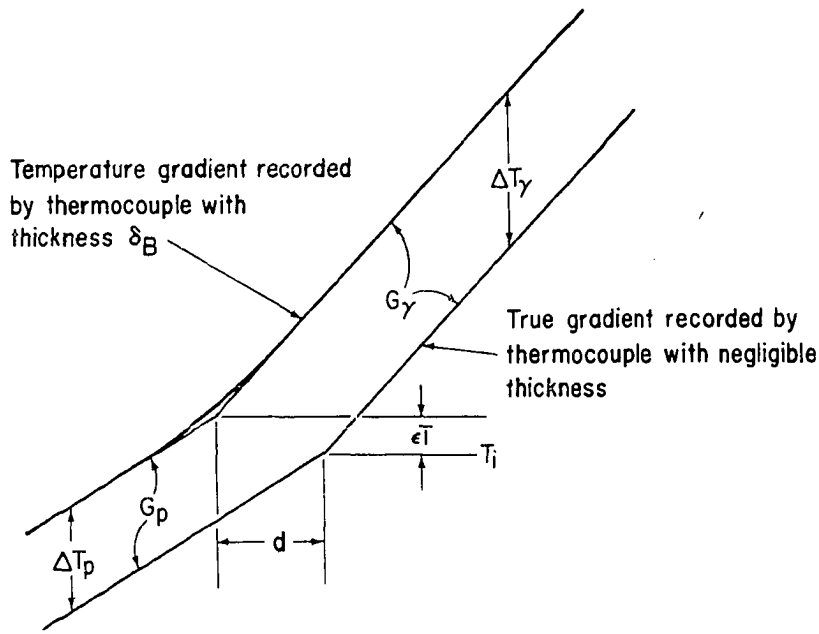

Fig. B-2. Relation between true gradient and recorded gradient at the $\gamma \rightarrow P$ interface

and

$$\Delta T_p = G_B^P \delta_B, \qquad \text{(B-3)}$$

where G_B^γ and G_B^P are the thermal gradients in the bead when it is in the austenite and pearlite phases respectively. The recorded change in gradient cannot be perfectly sharp because the gradient in the bead varies continuously during the transition between the two phases. However, the degree of curvature will have no effect on the interface temperature obtained by extrapolation because as shown in Figure B-2, the extrapolated temperature depends only on the values ΔT_p and ΔT_γ. Any error, ϵT, can be derived from the simple geometry of Figure B-2 and is given by

$$\varepsilon T = \frac{G_\gamma \Delta T_p - G_p \Delta T_\gamma}{G_\gamma - G_p} \qquad \text{(B-4)}$$

Substitution of Equations B-2 and B-3 gives

$$\varepsilon T = \delta_B \frac{G_\gamma \; G_p}{G_\gamma - G_p} (k_B^p - k_B^\gamma), \qquad \text{(B-5)}$$

where $k_B^p = G_B^p/G_\gamma$ and $k_B^\gamma = G_B^\gamma/G_p$. Thus, an error in determining the interface temperature will occur when the gradient in the bead is either not identical to the gradient in the sample, or the ratio of the bead gradient to the sample gradient is different in the two phases. An estimate of the magnitude of the error can be made by assuming G_γ = 2000°C/cm and G_γ/G_p = 1.34 (from average of ratios from Appendix C) and that δ_B = .008 cm. With a 5% variation in k_B^p and k_B^γ, εT is 2.4°C.

The preceding analysis assumed that the emf generated by the bead depended only on the temperature of the plane of the lead terminations. Actually, this is not the case since the composition varies in the bead and the bead is not isothermal. Therefore, the output of the thermocouple is an average of the temperature distribution within the bead. The average temperature indicated by the thermocouple may not be the average temperature of the gradient in the bead. The average output of the thermocouple will be weighted by the mass fraction of the bead at each isotherm and the composition variation in the bead. If the position of the average temperature is independent of the gradient, which is a reasonable assumption,

Equation B-5 can be applied. The net result is to reduce δ_B which in turn reduces the error εT.

Because the thermocouple averages the temperature distribution within the bead in some unknown way, calibration of the thermocouple against an isothermal standard may be in error. An alternative to an isothermal standard would be the measurement of some constant temperature in the same gradient used to obtain the austenite to pearlite interface temperatures. Measurements made on the change in gradient at the austenitizing interface indicated that there was no trend in the data showing an increase in temperature with increased rate. This implies that there is little or no superheating above the eutectoid temperature and that the material transforms continuously upon reaching the eutectoid isotherm. The measured temperature from the change in gradient at the austenitizing interface becomes a reliable reference to calibrate the austenite to pearlite interface temperature determinations. Figure B-3 shows several $Fe_3C + \alpha \rightarrow \gamma$ transformation interfaces observed in this study. Each micrograph shows that the interface is not sharp and that there is a diffuse region over which the transformation takes place. The purpose of the following discussion is to show that a possible error could result from this calibration since there is a range of temperature over which the reaction occurs but that this range is small and negligible error is involved.

Fig. B-3. SEM micrographs of representative structures associated with quenched austenitizing interfaces. Arrows indicate direction of interface motion with respect to sample. The light gray areas are fine pearlite formed during the quench from regions of austenite just transformed, the dark background is ferrite from the initial structure, and the initial carbide dispersion can be seen as either lamellar or small spheroids. a) Rate: 106 μm/sec. Initial structure was fine pearlite which had coarsened during heating in the gradient. Fine pearlite can be seen at right edge of micrograph indicating the onset of austenitization. Distance to large undissolved ferrite particle on left is 7.4 (10^{-3}) cm. 1200X. b) Rate: 24.7 μm/sec. Initial structure was directionally transformed pearlite; 550X. c) Rate: 4.43 μm/sec. Initial structure was slowly transformed pearlite; 1300X. d) Rate: 4.43 μm/sec. Initial structure was tempered martensite which had spheroidized during heating in the gradient; 1300X. All samples etched with Picral

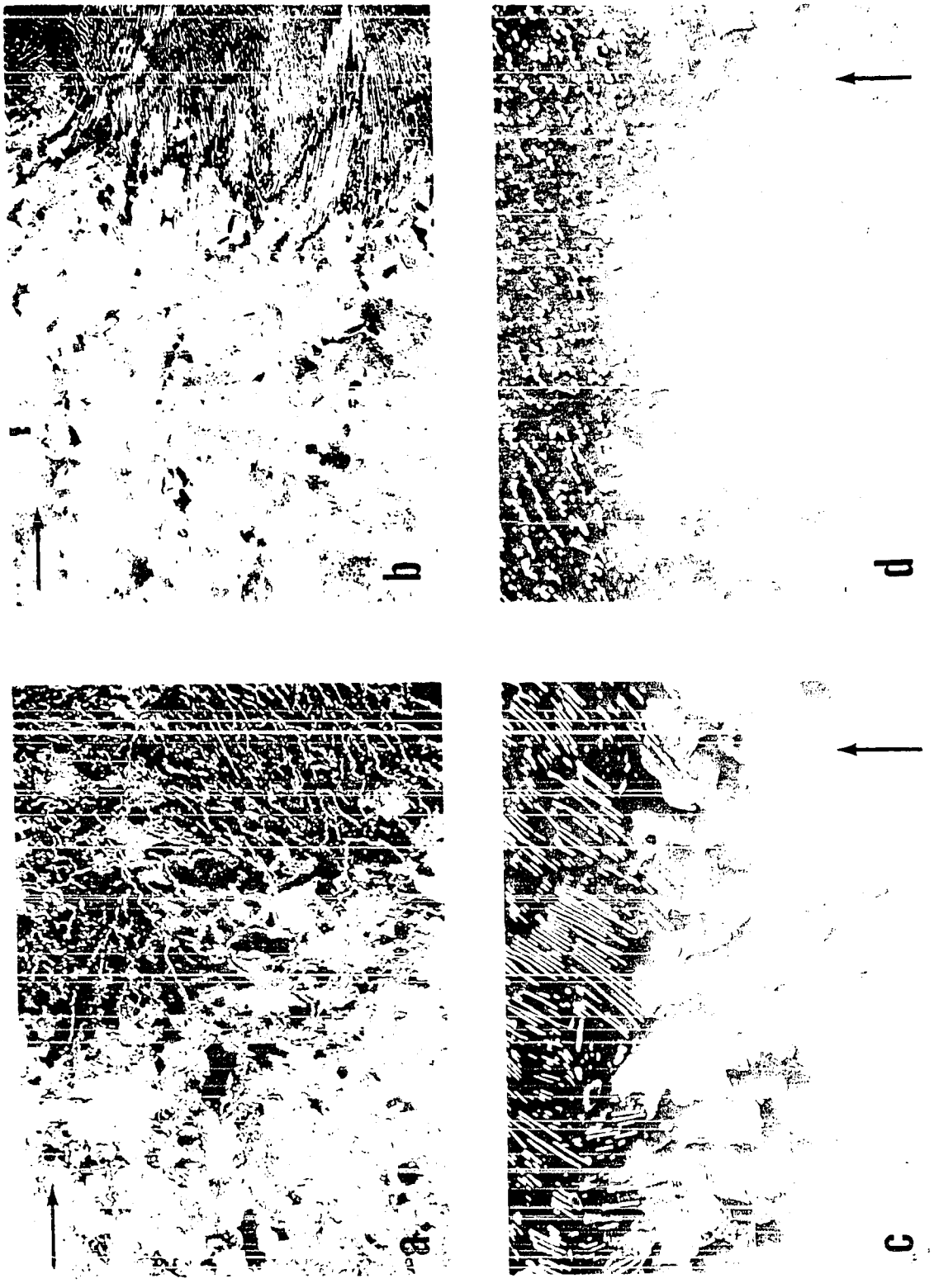
b
d
c

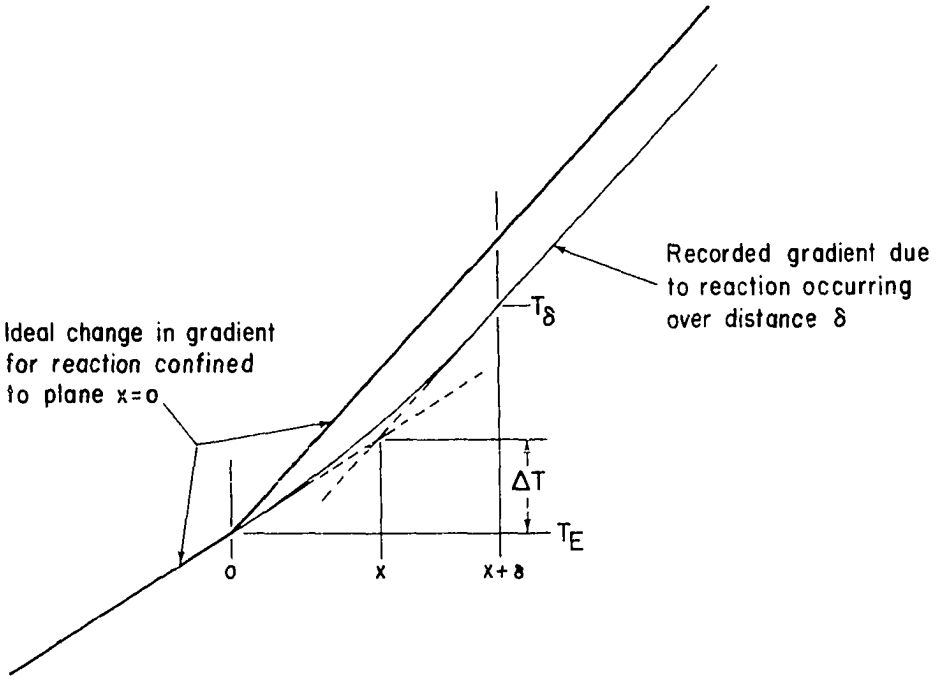

Fig. B-4. Geometry of ideal and recorded gradients of the austenitizing interface.

Figure B-4 shows the ideal gradient change for complete phase transformation at the eutectoid temperature and the recorded gradient resulting from a diffuse boundary with thickness δ. Both gradients are obtained from a thermocouple with infinitesimal thickness and the temperature increase, ΔT, is the measured super heat. Again by simple geometry ΔT can be obtained from Figure B-4 and is given by

$$\Delta T = xG_E = T_\delta - T_E - G_\gamma(\delta - x) \qquad \text{(B-9)}$$

or

$$\Delta T = \frac{G_E}{G_\gamma - G_E}\left(\delta G_\gamma - (T_\delta - T_E)\right) \qquad \text{(B-10)}$$

The difference $T_\delta - T_E$ can be obtained by integrating the tem-

perature gradient in the diffuse zone from 0 to δ or

$$T_\delta - T_E = \int_o^\delta \frac{dT}{dx}\Big)_{zone} dx \qquad \text{(B-11)}$$

For constant heat flow the gradient in the zone is

$$\frac{\partial T}{\partial x}\Big)_{zone} = \frac{k_\gamma G_\gamma}{k_{zone}} = \frac{k_\gamma G_\gamma}{k_E(1-f_\gamma)+k_\gamma f_\gamma} \qquad \text{(B-12)}$$

The amount of austenite will be assumed to change linearly through the austenitizing zone so that Equation B-11 becomes

$$T_\delta - T_E = \int_o^\delta \frac{k_\gamma G_\gamma \, dx}{k_E(1-\frac{x}{\delta})+k_\gamma \frac{x}{\delta}} = \frac{\delta k_\gamma G_\gamma}{k_\gamma - k_E} \ln \frac{k_\gamma}{k_E} \qquad \text{(B-13)}$$

which becomes $.86\delta G_\gamma$ with $k_E = 1.34\ k_\gamma$. The amount of superheat observed is then obtained from Equation B-10.

$$\Delta T = \frac{.14 G_E G_\gamma}{G_\gamma - G_E} = 824\delta\,°C \qquad \text{(B-14)}$$

when δ is in cm, $G_\gamma = 2000$ °C/cm and $G_E = 1.34\ G_\gamma$.

The largest distance δ observed is $7.4(10^{-3})$cm shown for a translation rate of 100 μm/sec in Figure B-3a. This gives a superheat of 6.1°C. The other figures show δ to be correspondingly smaller with Figure B-3d showing $\delta = 2.6(10^{-3})$cm indicating $\Delta T = 2$°C. The analysis leading to Equation B-14 assumed linear conversion to austenite with distance over the transition zone. Careful analysis of the micrographs in Figure B-3 indicates that this is not entirely correct. The transformation rate appears to increase with distance from the

eutectoid isotherm. Applying a more rigorous analysis on $f_\gamma(s)$ would reduce the predicted superheat of Equation B-13.

The average of 48 austenitizing interface temperature measurements was 724.7°C with a standard deviation of 4.7°C. There was no trend in the data towards increased temperature with increasing rate and the recorded gradient was sharp, similar to Figures 9 and 10, which implies the transformation occurred very quickly. The range in temperature is large enough to cover the small error of superheating effects. Hence, the thermocouple was calibrated using the eutectoid temperature 727°C.

The thermocouple was also calibrated isothermally against the melting point of pure aluminum by the technique described on page 41 of this dissertation. The difference between the two calibration techniques was 4.5°C. However, the use of the austenitizing interface measurements for calibrating the thermocouple for the austenite to pearlite temperature determinations was selected for three reasons. First, the average emf of a thermocouple bead in a thermal gradient may not correspond to the average temperature of the gradient and calibration against an isothermal standard may be in error. Second, the austenitizing interface temperature measurements were constant indicating that there was little or no superheat so that the eutectoid temperature could be used as a reference temperature. Third, both the austenitizing interface tempera-

ture measurements and the austenite to pearlite interface measurements were made in the same thermal gradient.

APPENDIX C. THERMAL DATA FROM GRADIENT MEASUREMENTS

Table C-1. Thermal data from sample 1

Run no.	Rate $\gamma \rightarrow P$ µm/sec	T_i $\gamma \rightarrow P$ mV	G_γ $\gamma \rightarrow P$ °C/cm	G_P $\gamma \rightarrow P$ °C/cm	Ratio $\gamma \rightarrow P$ G_γ/G_P	Max. temp. °C	Rate $P \rightarrow \gamma$ µm/sec	G_γ $P \rightarrow \gamma$ °C/cm	G_P $P \rightarrow \gamma$ °C/cm	Ratio $P \rightarrow \gamma$ G_γ/G_P	T_i $P \rightarrow \gamma$ mV
1	67.4	5.96	1750	1270	1.38	1235	67.4	1650	1240	1.33	6.96
2	67.4	6.02	1780	1220	1.46	1235	67.4	1730	1260	1.37	7.04
3	67.4	6.06	1790	1240	1.44	1240	67.4	1720	1330	1.29	6.94
4	67.4	6.05	1900	1300	1.46	1265	67.4	1670	1320	1.27	7.04
5	48.7	6.14	1720	1270	1.35	1240	48.7	1830	1450	1.26	7.06
6	48.7	6.17	1730	1260	1.37	1240	48.7	1670	1390	1.20	7.05
7	48.7	6.18	1530	1270	1.20	1245	48.7	1760	1450	1.21	7.06
8	106.0	5.67	1780	1240	1.44	1215	106.0	1600	1270	1.26	7.05
9	106.0	5.66	1870	1290	1.45	1225	106.0	1550	1160	1.34	6.97
10	106.0	5.60	1900	1320	1.44	1305	106.0	1740	1250	1.39	6.94
11	24.7	6.33	1710	1230	1.39	1250	24.7	1560	1280	1.22	6.94
12	24.7	6.34	1570	1280	1.23	1210	24.7	1610	1410	1.14	7.04
13	24.7	6.36	1530	1280	1.20	1165	24.7	1470	1220	1.20	6.99
14	10.8	6.55	1650	1310	1.26	1225	10.8	1620	1380	1.17	7.05
15	10.8	6.50	1630	1230	1.33	--	--	--	--	--	--
16	10.8	6.50	1710	1300	1.32	--	--	--	--	--	--
17	10.8	6.54	1730	1340	1.29	--	--	--	--	--	--
18	10.8	6.60	1690	1310	1.29	--	--	--	--	--	--
19	4.43	6.74	1630	1310	1.24	--	--	--	--	--	--
20	4.43	6.73	1860	1360	1.37	--	--	--	--	--	--

Table C-2. Thermal data from sample 2

Run no.	Rate $\gamma \rightarrow P$ μm/sec	T_i $\gamma \rightarrow P$ mV	$G\gamma$ $\gamma \rightarrow P$ °C/cm	Gp $\gamma \rightarrow P$ °C/cm	Ratio $\gamma \rightarrow P$ G_γ/G_p	Max. temp. °C	Rate $P \rightarrow \gamma$ μm/sec	$G\gamma$ $P \rightarrow \gamma$ °C/cm	Gp $P \rightarrow \gamma$ °C/cm	Ratio $P \rightarrow \gamma$ G_γ/G_p	T_i $P \rightarrow \gamma$ mV
1	106.0	5.50	1890	1300	1.45	1255	106.0	1560	1240	1.26	7.15
2	106.0	5.54	1980	1240	1.60	1245	--	--	--	--	--
3	106.0	5.67	1960	1280	1.53	1260	106.0	1700	1270	1.34	7.08
4	106.0	5.67	1910	1240	1.54	1260	106.0	1890	1470	1.29	7.06
5	106.0	5.68	1980	1270	1.56	1295	106.0	1820	1430	1.27	7.06
6	106.0	5.62	1970	1190	1.66	1260	106.0	1930	1430	1.35	7.04
7	106.0	5.68	1960	1110	1.76	1215	106.0	1670	1260	1.33	7.00
8	56.4	6.02	1810	1340	1.35	--	56.4	1724	1425	1.21	7.06
9	56.4	6.16	2090	1360	1.54	--	--	--	--	--	--
10	56.4	6.06	1900	1250	1.52	--	--	--	--	--	--
11	56.4	6.07	1820	1220	1.49	--	--	--	--	--	--
12	83.6	5.74	1830	1200	1.53	1250	83.6	1620	1440	1.13	7.00
13	83.6	5.78	1850	1200	1.54	1235	83.6	1670	1200	1.39	6.96
14	83.6	5.78	1820	1150	1.58	1205	83.6	1470	1260	1.17	6.98
15	83.6	5.92	1790	1100	1.63	1165	83.6	1290	1130	1.14	6.95
16	83.6	5.81	1800	1160	1.55	1210	83.6	1480	1150	1.29	6.95
17	83.6	5.89	1770	1090	1.62	1175	--	--	--	--	--

Table C-3. Thermal data from sample 3

Run no.	Rate $\gamma \rightarrow P$ μm/sec	T_i $\gamma \rightarrow P$ mV	G_γ $\gamma \rightarrow P$ °C/cm	G_P $\gamma \rightarrow P$ °C/cm	Ratio $\gamma \rightarrow P$ G_γ/G_P	Max. temp. °C	Rate $P \rightarrow \gamma$ μm/sec	G_γ $P \rightarrow \gamma$ °C/cm	G_P $P \rightarrow \gamma$ °C/cm	Ratio $P \rightarrow \gamma$ G_γ/G_P	T_i $P \rightarrow \gamma$ mV
1	24.7	6.37	1760	1270	1.39	1195	24.7	1530	1230	1.24	6.98
2	24.7	6.36	1790	1240	1.44	1215	24.7	1600	1260	1.27	7.07
3	48.7	6.08	1720	1220	1.41	1165	48.7	1450	1170	1.24	7.09
4	48.7	6.12	1770	1300	1.36	1165	48.7	1620	1220	1.33	7.10
5	34.4	6.18	1830	1250	1.46	1185	34.3	1450	1290	1.12	7.08
6	34.4	6.19	1740	1250	1.39	1170	34.3	1450	1160	1.25	7.05
7	34.4	6.18	1780	1320	1.35	1190	34.3	1620	1210	1.34	7.10
8	34.4	6.20	1680	1290	1.30	1200	34.3	1610	1290	1.25	7.11
9	34.4	6.20	1750	1330	1.32	1225	34.3	1600	1270	1.26	7.12
10	15.4	6.46	1770	1270	1.39	--	--	--	--	--	--

Table C-4. Thermal data from sample 4

Run no.	Rate $\gamma \rightarrow P$ μm/sec	T_i $\gamma \rightarrow P$ mV	G_γ $\gamma \rightarrow P$ °C/cm	G_P $\gamma \rightarrow P$ °C/cm	Ratio $\gamma \rightarrow P$ G_γ/G_P	Max. temp. °C	Rate $P \rightarrow \gamma$ μm/sec	G_γ $P \rightarrow \gamma$ °C/cm	G_P $P \rightarrow \gamma$ °C/cm	Ratio $P \rightarrow \gamma$ G_γ/G_P	T_i $P \rightarrow \gamma$ mV
1	15.4	6.47	1820	1240	1.47	1165	48.7[a]	2110	1740	1.21	7.06
2	15.4	6.52	1690	1300	1.30	1175	48.7	2070	1860	1.11	7.04
3	15.4	6.54	1720	1350	1.27	1190	48.7	2000	1830	1.09	7.06
4	15.4	6.53	1790	1250	1.43	1260	48.7	2350	1920	1.22	7.07
5	10.8	6.65	1930	1320	1.46	1230	48.7	1710	1330	1.29	7.13
6	10.8	6.60	1730	1390	1.24	1250	48.7	1640	1360	1.20	6.97
7	4.43	6.77	1890	1280	1.48	1245	48.7	1780	1360	1.31	7.06
8	4.43	6.84	1740	1390	1.25	1235	48.7	1640	1380	1.19	7.13
9	4.43	6.78	1780	1340	1.33	1240	48.7	1790	1510	1.19	7.08
10	1.11	6.89	1760	1270	1.39	1245	48.7	1590	1320	1.20	7.05
11	1.11	6.91	1690	1300	1.30	1200	48.7	1570	1430	1.10	7.05
12	1.11	6.85	1540	1190	1.29	--	1.11	1610	1170	1.38	6.94
13	1.11	6.90	1740	1160	1.50	--	1.11	1640	1260	1.30	6.94

[a]During the first 11 runs, the sample was transformed at a rate of 48.7 μm/sec until the maximum temperature was reached. At this point the rate was changed to the slower rate given in column 2. This procedure was used solely to conserve time and the sample. The $\gamma \rightarrow P$ interface temperature is in no way affected since there was ample time for the sample to reach steady-state before the thermocouple bead passed through the interface plane.

APPENDIX D. APPROXIMATE CALCULATION OF THE AVERAGE CARBON CONCENTRATION IN AUSTENITE ADJACENT TO THE PEARLITIC INTERFACE

The differential equation for diffusion of carbon in austenite adjacent to pearlite growing with velocity v is

$$\frac{\partial^2 C}{\partial x^2} + \frac{\partial^2 C}{\partial y^2} - \frac{v}{D_C^{\gamma}} \frac{\partial C}{\partial x} = 0. \qquad \text{(D-1)}$$

This equation has been solved rigorously by Hillert (17) assuming D_C^{γ} constant and that local curvature of the ferrite and cementite platelet tips specifies the carbon concentration in austenite at the interface. A similar analysis for lamellar and rod eutectic growth has been given by Jackson and Hunt (51). Both treatments provide methods for calculating the average carbon concentration in austenite adjacent to the pearlitic interface. A consequence of both analyses is that the average concentration is not equal to the eutectoid composition if the phase diagram is not completely symmetric about the eutectoid concentration and if identical curvatures and free energy changes are not associated with both new phases. In binary systems where these two conditions are not present, the average concentration is different from the eutectoid composition and is a function of the growth conditions. Jackson and Hunt presented an explicit equation predicting the change in concentration as a function of undercooling below the eutectic temperature. Their equation (Jackson and Hunt (51, Eq. 22)) can be modified for the present problem of

eutectoid growth in the Fe-C binary system and is given by Equation D-2. A similar equation can be obtained from Hillert's (17) analysis with the only difference being the treatment of the thermodynamic quantity, ψ.

$$\bar{x}_\gamma = x_\gamma^E + \frac{\Delta T}{2m}\left\{\frac{m_{C_m} - m_\alpha}{m_{C_m} + m_\alpha} + \frac{1}{2}\frac{1-\xi}{1+\xi} - \frac{1}{2}\frac{1-\psi}{1+\psi}\right\} \qquad \text{(D-2)}$$

where $\bar{x}_\gamma$ = average carbon concentration (at. fr)

x_γ^E = eutectoid carbon concentration (.0349 at. fr)

ΔT = undercooling below the eutectoid temperature

m_{C_m} = slope of the extrapolated $\gamma/\gamma+C_m$ phase boundary $\tilde{\cong}$ 13000°C/at. fr

m_α = slope of the extrapolated $\gamma/\gamma+\alpha$ phase boundary $\tilde{\cong}$ 2100°C/at. fr

$$\frac{1}{m} = \frac{1}{m_\alpha} + \frac{1}{m_{C_m}} \tilde{\cong} 5.5(10^{-4}) \text{ at. fr/°C}$$

$$\xi = \frac{S^{C_m}}{S^\alpha} = .134$$

$$\psi = \frac{1}{\xi} \cdot \frac{m_\alpha}{m_{C_m}} \cdot \frac{\Delta H_T^{\gamma\rightarrow\alpha}}{\Delta H_T^{\gamma\rightarrow C_m}} \cdot \frac{\sigma^{\gamma/C_m} \sin\theta^{\gamma/C_m}}{\sigma^{\gamma/\alpha} \sin\theta^{\gamma/\alpha}}$$

$\Delta H_T^{\gamma\rightarrow\alpha}$ = enthalpy of the austenite to ferrite phase transformation per unit volume

$\Delta H_T^{\gamma\rightarrow C_m}$ = enthalpy of the austenite to cementite phase transformation per unit volume

σ^{γ/C_m} = surface energy of the austenite/cementite phase boundary

$\sigma^{\gamma/\alpha}$ = surface energy of the austenite/ferrite phase boundary

θ^{γ/C_m}, $\theta^{\gamma/\alpha}$ = defined in Figure D-1

The calculation of Ψ depends on the enthalpy of the austenite to pearlite phase transformation and the surface energy of the related phase boundaries. For the lack of reliable data, the surface energies, σ^{γ/C_m} and $\sigma^{\gamma/\alpha}$, are assumed equal and the angles, $\theta^{\gamma/\alpha}$ and θ^{γ/C_m}, are assumed equal. The enthalpy of the pure iron $\gamma \rightarrow \alpha$ transformation is 3200 J/mol (48) and the enthalpy of the pearlite reaction is 4200 J/mol (45). From these two values, the enthalpy of the $\gamma \rightarrow C_m$ transformation can be calculated through the relation

$$\Delta H_T^{\gamma \rightarrow \alpha + C_m} = f_\alpha \Delta H_T^{\gamma \rightarrow \alpha} + f_{C_m} \Delta H_T^{\gamma \rightarrow C_m} \qquad \text{(D-3)}$$

which yields the value $\Delta H_T^{\gamma \rightarrow C_m} = 10{,}200$ J/mol. The value for ψ can now be estimated and in turn, the three quantities within the brackets of Equation D-2 can be calculated:

$$\frac{m_{C_m} - m_\alpha}{m_{C_m} + m_\alpha} = .722, \qquad \text{(D-4)}$$

$$\frac{1}{2}\,\frac{1-\xi}{1+\xi} = .382, \qquad \text{(D-5)}$$

and

$$-\frac{1}{2}\left(\frac{1-\Psi}{1+\Psi}\right) = -.225 \pm .080. \qquad \text{(D-6)}$$

The range of the value calculated for Equation D-6 results

from assuming a 50% error in Ψ. From this we can calculate a value for $\bar{x}_\gamma$

$$\bar{x}_\gamma = x^E + (2.42 \pm .22)10^{-4}\Delta T.$$

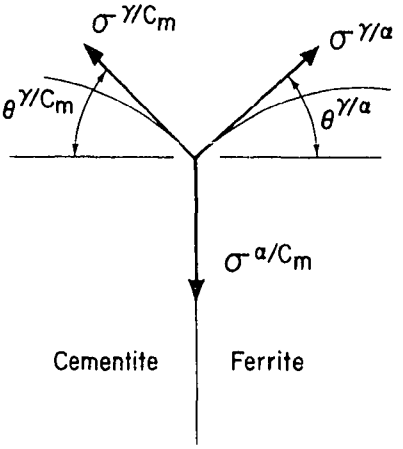

Fig. D-1. Schematic drawing of pearlite growth front defining θ^{γ/C_m} and $\theta^{\gamma/\alpha}$